

AD-A269 351



Defense Nuclear Agency
Alexandria, VA 22310-3398



DNA-TR-92-176

**Numerical and Analytical Solutions to Benchmark
Problems Related to Tunnel Mechanics**

Donald A. Simons
Logicon R & D Associates
P.O. Box 92500
Los Angeles, CA 90009

DTIC
ELECTE
SEP 14 1993
S A D

September 1993

Technical Report

CONTRACT No. DNA 001-88-C-0046

Approved for public release;
distribution is unlimited.

93 9 13 03 1

93-21235



Destroy this report when it is no longer needed. Do not return to sender.

PLEASE NOTIFY THE DEFENSE NUCLEAR AGENCY,
ATTN: CSTI, 6801 TELEGRAPH ROAD, ALEXANDRIA, VA
22310-3398, IF YOUR ADDRESS IS INCORRECT, IF YOU
WISH IT DELETED FROM THE DISTRIBUTION LIST, OR
IF THE ADDRESSEE IS NO LONGER EMPLOYED BY YOUR
ORGANIZATION.



REPORT DOCUMENTATION PAGE

Form Approved
OMB No. 0704-0188

Public reporting burden for this collection of information is estimated to average 1 hour per response including the time for reviewing instructions, searching existing data sources, gathering and maintaining the data needed, and completing and reviewing the collection of information. Send comments regarding this burden estimate or any other aspect of this collection of information, including suggestions for reducing this burden, to Washington Headquarters Service, Directorate for Information Operations and Reports, 1215 Jefferson Davis Highway, Suite 1204, Arlington, VA 22202-4302, and to the Office of Management and Budget, Paperwork Reduction Project (0704-0188), Washington, DC 20503

1. AGENCY USE ONLY (Leave blank)		2. REPORT DATE 930901	3. REPORT TYPE AND DATES COVERED Technical 910401 - 920915	
4. TITLE AND SUBTITLE Numerical and Analytical Solutions to Benchmark Problems Related to Tunnel Mechanics			5. FUNDING NUMBERS C - DNA 001-88-C-0046 PE - 62715H PR - RD TA - RC WU - DH000015	
6. AUTHOR(S) Donald A. Simons				
7. PERFORMING ORGANIZATION NAME(S) AND ADDRESS(ES) Logicon R & D Associates P.O. Box 92500 Los Angeles, CA 90009			8. PERFORMING ORGANIZATION REPORT NUMBER RDA-TR-2-2270-2402-001	
9. SPONSORING/MONITORING AGENCY NAME(S) AND ADDRESS(ES) Defense Nuclear Agency 6801 Telegraph Road Alexandria, VA 22310-3398 SPSD/Senseny			10. SPONSORING/MONITORING AGENCY REPORT NUMBER DNA-TR-92-176	
11. SUPPLEMENTARY NOTES This work was sponsored by the Defense Nuclear Agency under RDT&E RMC Code B4662D RD RC 00015 25904D.				
12a. DISTRIBUTION/AVAILABILITY STATEMENT Approved for public release; distribution is unlimited.			12b. DISTRIBUTION CODE	
13. ABSTRACT (Maximum 200 words) In this report, five numerical approaches to problems of tunnel dynamics are compared with each other and—wherever possible—with exact analytic solutions. The medium is an idealization of a jointed rock mass. The intact rock is linear elastic-plastic with a pressure-dependent failure surface and associated plastic flow law. There are two orthogonal sets of equally spaced joints. Each joint is nonlinear elastic in the normal direction and linear elastic with Coulomb friction in shear. All the methods but one represent the intact rock by continuum elements; the other treats it as rigid and lumps its compliance in the joints. Most methods represent the joints as sliding interfaces, but one models them also as finite elements. Most methods have two different types of models for jointed rock, an <i>explicit</i> one where the joints are treated separately, and an <i>implicit</i> one where their properties are lumped together with those of the intact rock. Seven problems are posed. In the simplest of the problems a strain history is specified for a block of intact rock. In the most complex, a lined tunnel in jointed rock mass is engulfed by a cylindrically divergent stress wave. A complete analytic solution is derived for the first problem, incrementally analytic ones for the next four, and an idealized static orthotropic elastic solution for the last one. Based on a combination of physical understanding (of wave propagation and material behavior) and comparison with the analytic solutions, three of the numerical approaches are judged to have produced credible results to final problem.				
14. SUBJECT TERMS Benchmark Tunnel Deformation Tunnel Mechanics Tunnel Vulnerability			15. NUMBER OF PAGES 122	
			16. PRICE CODE	
17. SECURITY CLASSIFICATION OF REPORT UNCLASSIFIED	18. SECURITY CLASSIFICATION OF THIS PAGE UNCLASSIFIED	19. SECURITY CLASSIFICATION OF ABSTRACT UNCLASSIFIED	20. LIMITATION OF ABSTRACT SAR	

CLASSIFIED BY:

N/A since Unclassified.

DECLASSIFY ON:

N/A since Unclassified.

PREFACE

This report was prepared at Logicon RDA as part of RDA's technical support to DNA under the SETA contract (DNA001-88-C-0046). Paul Senseny (DNA/SPSD) served as technical monitor. The report relies heavily on analysis performed by four contractors and a government laboratory under DNA funding, also monitored by Dr. Senseny. The analyses by RE/SPEC was performed under subcontract to SwRI, and was monitored at SwRI by Ben Thacker. The analysis by Itasca was performed under subcontract to Weidlinger Associates.

The author would like to thank a number of other people for technical and editorial contributions to this report. Above all, the benchmark study participants—Loren Lorig (Itasca), Francois Heuze and Ronald Shaffer (LLNL), John Osnes (RE/SPEC), Yoshio Muki and Marvin Ito (CRT), and Felix Wong and Darrent Tennant (WA)—have been most helpful and willing to supply information when asked. Those individuals and David Vaughan (WA) graciously wrote the appendices describing their organizations' numerical approaches. Liz Garnholz (RDA) cheerfully digitized countless curves and prepared most of the figures. Eric Furbee (RDA) contributed some of the figures. Anita Gigliello and Kip Radler (RDA) helped with the final preparation of the document.

The numerical work by LLNL and the contractors was mainly performed between February and July 1991, reviewed and discussed at three meetings during that same time span, and summarized in a series of briefing packages distributed at the time by RDA. The numerical results reproduced here came for the most part from those briefing packages. The problem definitions and requested outputs had been spelled out in detail in a series of memos from Dr. Senseny and—in one case (problem 2-S)—by the author. In several cases some of the requested outputs were missing from one or more participant's presentation. Except in one instance where a part of the package had been mislaid, the author chose to work only with the available information. Thus when comparisons are presented among various calculations, results may be missing for a particular organization. The reason is that the results had not been submitted in the first place, although usually no specific remark to that effect will appear in the text.

Accession For	
NTIS CRA&I	<input checked="" type="checkbox"/>
DTIC TAB	<input type="checkbox"/>
Unannounced	<input type="checkbox"/>
Justification	
By	
Distribution	
Availability Codes	
Dist	Avail and/or Special
A-1	

CONVERSION TABLE

Conversion factors for U.S. customary to metric (SI) units of measurement

To Convert From	To	Multiply
angstrom	meters (m)	1.000 000 X E-10
atmosphere (normal)	kilo pascal (kPa)	1.013 25 X E+2
bar	kilo pascal (kPa)	1.000 000 X E+2
barn	meter ² (m ²)	1.000 000 X E-28
British Thermal unit (thermochemical)	joule (J)	1.054 350 X E+3
calorie (thermochemical)	joule (J)	4.184 000
cal (thermochemical)/cm ²	mega joule/m ² (MJ/m ²)	4.184 000 X E-2
curie	giga becquerel (GBq)*	3.700 000 X E+1
degree (angle)	radian (rad)	1.745 329 X E-2
degree Fahrenheit	degree kelvin (K)	$t_K = (t_F + 459.67) / 1.8$
electron volt	joule (J)	1.602 19 X E-19
erg	joule (J)	1.000 000 X E-7
erg/second	watt (W)	1.000 000 X E-7
foot	meter (m)	3.048 000 X E-1
foot-pound-force	joule (J)	1.355 818
gallon (U.S. liquid)	meter ³ (m ³)	3.785 412 X E-3
inch	meter (m)	2.540 000 X E-2
jerk	joule (J)	1.000 000 X E+8
joule/kilogram (J/Kg) (radiation dose absorbed)	Gray (Gy)	1.000 000
kilotons	terajoules	4.183
kip (1000 lbf)	newton (N)	4.448 222 X E+3
kip/inch ² (ksi)	kilo pascal (kPa)	6.894 757 X E+3
ktap	newton-second/m ² (N-s/m ²)	1.000 000 X E+2
micron	meter (m)	1.000 000 X E-6
mil	meter (m)	2.540 000 X E-5
mile (international)	meter (m)	1.609 344 X E+3
ounce	kilogram (kg)	2.834 952 X E-2
pound-force (lbf avoirdupois)	newton (N)	4.448 222
pound-force inch	newton-meter (N·m)	1 129 848 X E-1
pound-force/inch	newton/meter (N/m)	1.751 268 X E+2
pound-force/foot ²	kilo pascal (kPa)	4.788 026 X E-2
pound-force/inch ² (psi)	kilo pascal (kPa)	6.894 757
pound-mass (lbm avoirdupois)	kilogram (kg)	4.535 924 X E-1
pound-mass-foot ² (moment of inertia)	kilogram-meter ² (kg·m ²)	4.214 011 X E-2
pound-mass/foot ³	kilogram/meter ³ (kg/m ³)	1.601 846 X E+1
rad (radiation dose absorbed)	Gray (Gy)**	1.000 000 X E-2
roentgen	coulomb/kilogram (C/kg)	2.579 760 X E-4
shake	second (s)	1.000 000 X E-8
slug	kilogram (kg)	1.459 390 X E+1
torr (mm Hg, 0°C)	kilo pascal (kPa)	1.333 22 X E-1

*The becquerel (Bq) is the SI unit of radioactivity: Bq = 1 event/s.

**The Gray (Gy) is the SI unit of absorbed radiation.

TABLE OF CONTENTS

Section	Page
PREFACEiii
CONVERSION TABLE	iv
FIGURES	viii
TABLES	x
1 INTRODUCTION	1
1.1 BACKGROUND AND OBJECTIVE	1
1.2 SCOPE	2
2 GENERAL SPECIFICATIONS	4
2.1 GEOMETRY	4
2.2 MATERIAL MODELS	4
3 STATEMENTS AND RESULTS FOR PROBLEMS WITH ANALYTICAL SOLUTIONS	7
3.1 ANALYTIC TREATMENT OF MATERIAL RESPONSE	7
3.2 PROBLEM 1-IN: SPHERICALLY DIVERGENT STRAIN PATH IN INTACT ROCK	9
3.2.1 Statement of the Problem	9
3.2.2 Analytic Solution	10
3.2.3 Numerical Solutions	12
3.3 PROBLEM 1-IM: SPHERICALLY DIVERGENT STRAIN PATH IN IMPLICITLY JOINTED ROCK	14
3.3.1 Statement of the Problem	14
3.3.2 Analytic Solution	14
3.3.3 Numerical Solutions	16
3.4 PROBLEMS 2-EX AND 2-IM: UNIAXIAL STRAIN OF A "STACK OF BRICKS"	16
3.4.1 Statement of the Problem	16
3.4.2 Analytical Solution	19
3.4.3 Numerical Solutions	19
3.5 PROBLEM 2-S: SHEARING OF TWO TRIANGULAR BLOCKS SEPARATED BY A SINGLE JOINT	22

TABLE OF CONTENTS (Continued)

Section	Page
3.5.1 Statement of the Problem	22
3.5.2 Analytical Solution	23
3.5.3 Analytical and Numerical Results	29
3.5.4 Why PRONTO Was Not Applicable to Problem 2-S	33
 4 PROBLEM STATEMENTS AND RESULTS FOR TWO-DIMENSIONAL PROBLEMS	 34
4.1 PRELIMINARY DISCUSSION	34
4.2 PROBLEM 3: DIVERGENT WAVE PROPAGATION THROUGH A JOINTED ROCK ISLAND	34
4.2.1 Statement of the Problem	34
4.2.2 Physical Effects Observed in the Numerical Solution	36
4.2.3 Numerical Issues	42
4.3 PROBLEM 4: LINED TUNNEL IN A JOINTED ROCK ISLAND SUBJECTED TO DIVERGENT WAVE PROPAGATION	44
4.3.1 Statement of the Problem	44
4.3.2 Physical Effects Observed in the Numerical Solutions	45
4.3.3 Orthotropic Elastic Predictions of Stresses	56
4.3.4 Remarks on the Numerical Solutions to Problem 4	59
 5 CONCLUSIONS	 61
 6 REFERENCES	 63
 Appendix	
A DESCRIPTION OF THE PRONTO2D COMPUTER CODE USED IN THE UNDERGROUND TECHNOLOGY PROGRAM BENCHMARK ACTIVITY	A-1
B THEORETICAL ASPECTS OF THE LLNL DIBS DISCRETE ELEMENT CODE USED IN THE DNA/UTP BENCHMARK EXERCISE	B-1

TABLE OF CONTENTS (Continued)

Section	Page
C DESCRIPTION OF FINITE ELEMENT METHOD USED IN UTP BENCHMARK ACTIVITY BY CALIFORNIA RESEARCH AND TECHNOLOGY	C-1
D DESCRIPTION OF THE DISTINCT ELEMENT METHOD USED IN THE UNDERGROUND TECHNOLOGY PROGRAM (UTP) BENCHMARK ACTIVITY	D-1
E THE APPLICATION OF THE FLEX PROGRAM TO UTP BENCHMARK PROBLEMS	E-1

FIGURES

Figure		Page
3-1	Geometry and loading in problems 1-IN and 1-IM	9
3-2	Intact rock compressibility in problem 1-IN	13
3-3	Intact rock stress path in problem 1-IN	13
3-4	Implicitly jointed rock compressibility in Problem 1-IM	17
3-5	Implicitly jointed rock stress difference vs pressure in problem 1-IM	17
3-6	Implicitly jointed rock effective stress $(J_2')^{1/2}$ vs pressure in problem 1-IM	18
3-7	Geometry and loading in problems 2-EX and 2-IM	18
3-8	Jointed rock compressibility in problem 2-EX	20
3-9	Stress path in problem 2-EX	20
3-10	Compressibility in problem 2-IM	21
3-11	Stress path in problem 2-IM	21
3-12	Geometry and loading in problem 2-S	22
3-13	Decomposition of joint displacements	26
3-14	Overall compressibility in problem 2-S	30
3-15	Von Mises effective stress path in problem 2-S	31
3-16	Joint shear displacement vs shear stress in problem 2-S	31
3-17	History of deformation mode in problem 2-S	32
4-1	Geometry and loading in problem 3	35
4-2	Radial stress at tunnel location in problem 3	36
4-3	Radial velocity at tunnel location in problem 3	37
4-4	Strain path at 500-m range, 2 degrees off axis, in problem 3	38
4-5	On-axis strain paths in implicitly jointed and intact rock, analytic solution and Itasca calculation, problem 3	39
4-6	Stress path at 487-m range on axis in implicitly jointed rock in problem 3	40
4-7	Compressibility at 487-m range on axis in problem 3	41
4-8	Radial stress pulse shapes at 480, 500, and 520-m ranges in problem 3	42
4-9	Hoop stress at 512-m range on axis, implicit and explicit region, problem 3	43
4-10	Geometry and loading in problem 4	44
4-11	Crown-invert closure in problem 4	45
4-12	Springline closure in problem 4	46
4-13	Radial stress field near the tunnel at peak free field stress arrival time (about 30 ms)	48
4-14	Tangential stress field near the tunnel at peak free field stress arrival time (about 30 ms)	49

FIGURES (Continued)

Figure		Page
4-15	Radial stress field near the tunnel at the end of the free-field positive phase (about 120 ms)	50
4-16	Tangential stress field near the tunnel at the end of the free-field positive phase (about 120 ms)	51
4-17	Slip along horizontal joints at peak free-field stress arrival	52
4-18	Slip along horizontal joints at the end of the free-field positive phase	53
4-19	Deformed tunnel shapes at end of positive phase (about 120 ms)	55

TABLES

Table		Page
1-1	The UTP benchmark problems	2
1-2	Participants in the UTP benchmark calculational exercise	3
2-1	Standardized geometric parameters	4
2-2	Material properties	5
3-1	Analytic solution to problem 1-IN	11
3-2	Imposed boundary displacements in problem 2-S	23
3-3	Potential deformation modes in problem 2-S	23
3-4	Road map for computational scheme used in problem 2-S	25
4-1	Joint slip contribution to springline closure	54

SECTION 1

INTRODUCTION

1.1 BACKGROUND AND OBJECTIVE.

In 1989 the Defense Nuclear Agency (DNA) initiated the Underground Technology Program (UTP), a multi-year investigation into the vulnerability of underground structures. The program includes calculations, material modelling, laboratory testing, and field testing all aimed at improving the ability to predict the response and failure of underground structures subjected to ground shock due to near-surface explosions. The emphasis is on deeply buried tunnels with little or no reinforcement. The focal point of the program is a field test to be conducted at Ft. Knox, wherein a buried high-explosive charge will be used to load various deeply buried structures in a saturated limestone formation.

During the course of the UTP at least five different organizations have been engaged in numerical modelling of various aspects of the relevant dynamic processes. Each organization has its own preconceptions about how best to construct these models. In order to explore the influence of the particular computational approach on the outcome of the numerical simulation, DNA conducted a "benchmark calculation" exercise. Several idealized problems were defined, and each participating organization was asked to apply its computational tools to generate certain specified outputs. This report summarizes the results of that activity.

Large rock masses inevitably contain discontinuities which are referred to as joints. In many cases they occur in one or several parallel sets with individual joints spaced at regular intervals. The numerical treatment of the combined effect of motion across joints and deformation of the intervening continuous blocks poses a formidable challenge. Most of the participants use two general, complementary approaches: *explicit*, in which the motions across the joints and the deformations within the blocks are represented separately; and *implicit*, wherein a single, effective medium is defined so as to deform on the average like an assemblage of blocks and joints¹. An implicit model, once defined, can be (and was in this study) used just like any other material model in a general purpose finite-element or finite difference code, while explicit models require special treatment. The model types are complementary in the sense that when applied to tunnel failure problems, the implicit models—which are more computationally efficient—suffice in regions remote from the tunnel, while the explicit ones—which are locally more accurate—must be used near the tunnel if the details of individual block motions are to be captured. As expected, the approaches to joint modelling provided the most stark contrasts among the participants.

¹In this report the terms *explicit* and *implicit* will always refer to the method for representing joints. They will not refer to the time integration scheme, except in the following sentence. All participants used explicit time integration.

1.2 SCOPE.

Table 1-1 contains a summary of the problems posed in the UTP benchmark calculation exercise. More precise definitions will be given later, when each problem is discussed in detail. Problems 1-IN and 1-IM exercise the intact (unjointed) and implicitly jointed material respectively over the same simple strain path. Problems 2-EX and 2-IM contrast the explicit and implicit treatment of a jointed sample over a simple strain path. Problem 2-S is the first one to cause shearing displacement across the joint. It was solved explicitly by most but implicitly by one participant. Problem 3 is the first one where dynamics and large-scale spatial variation come into play. It tests compatibility between adjacent regions of explicitly and implicitly jointed material. Problem 4 represents the way a "real" tunnel failure problem might be modelled, and provides a platform for comparing the tunnel deformations computed by the various schemes.

Table 1-1. The UTP benchmark problems.

Problem Name	Abbreviation	Geometry	Loading
1-Intact	1-IN	Single element, no joints	Quasi-static strain path representing spherically divergent flow
1-Implicit	1-IM	Single element with two perpendicular joints	Same strain path as 1-IN
2-Explicit	2-EX	"Stack of bricks," i.e., several continuous horizontal joints, several staggered vertical joints	Quasi-static uniaxial strain compression and unload
2-Implicit	2-IM	Same as 2-EX, but modelled implicitly	Same as 2-EX
2-Shear	2-S	Two triangular blocks separated by a joint	Quasi-static boundary displacements consistent with uniform plane strain, designed to cause joint slippage
3	3	Wedge section of annulus, modelled implicitly, except for inner region, modelled explicitly	Dynamic radial stress pulse on inner boundary
4	4	Same as 3 but lined tunnel within inner region	Same as 3

Table 1-2 lists the organizations and some of the individuals who participated in the exercise. It also contains the names of the codes used to perform the calculations. The only

ones which are generally available are PRONTO (through Sandia National Laboratory) and UDEC (through Itasca for a fee); the others are proprietary.

Table 1-2. Participants in the UTP benchmark calculational exercise.

Organization	Abbreviation	Point of Contact	Code
California Research and Technology Division, The Titan Corporation	CRT	Y. Marvin Ito	EXCALIBUR
Itasca Consulting Group, Inc.	Itasca	Loren Lorig	UDEC
Lawrence Livermore National Laboratory	LLNL	Francois Heuze	DIBS
RE/SPEC Inc.	RE/SPEC	John Osnes	PRONTO
Weidlinger Associates	WA	Felix Wong	FLEX
Logicon R & D Associates	RDA	Don Simons	Exact Solutions

A few brief remarks about the various approaches may be of interest at this point. All except Itasca and LLNL use finite elements to represent the rock as a deformable continuum; Itasca uses finite difference elements while LLNL treats the rock as rigid and approximates the rock's deformability by modifying the stiffness of the joints. All except CRT use some form of a slide line as part or all of their explicit joint model; CRT uses a special finite element. CRT has the most sophisticated implicit model, one which admits arbitrary constitutive behavior in both the intact rock and joint, and by enforcing internal compatibility and stress equilibrium derives a super-element representing the combined deformation due to both joints and intact rock. WA and Itasca's implicit models are isotropic elastic-plastic, while CRT and RE/SPEC's are anisotropic. Since the rock in this study contains two orthogonal joint sets, the large-scale rock mass behavior will be orthotropic (see Section 4.3.3). The latter two implicit modelling approaches have the potential to represent features of the deformation and stress fields peculiar to anisotropic media.

No further attempt will be made at this point to describe the details of these codes' treatments of the benchmark problems. Instead, each organization has prepared its own description which is included in this report as an appendix.

SECTION 2

GENERAL SPECIFICATIONS

2.1 GEOMETRY.

For those problems involving joints (all except 1-IN), a tunnel (4), or complex computational meshes (3 and 4), certain geometric parameters are standardized as shown in Table 2-1. Problems 3 and 4 are in plane strain, with a wedge-shaped mesh bounded by circular arcs of radii 450 and 550 m, a symmetry line through the tunnel location, and a ray at an angle of $\tan^{-1}0.1 = 5.71$ (making the mesh 50 m wide at the tunnel location). An inner, rectangular region extending 12.5 m in each direction from the tunnel location is modelled explicitly; the rest, implicitly.

Table 2-1. Standardized geometric parameters.

	Dimension	Symbol	Value
Joint	Joint Spacing	S	1 m
	Joint Thickness	δ	5 mm
Tunnel	Range of Tunnel	R_o	500 m
	Tunnel Diameter	D	5 m
	Liner Thickness	T	50 mm
Computational Mesh	Discrete Jointing Zone	L	25 m
	Mesh Height	H	100 m
	Mesh Divergence	θ	$\tan^{-1} 0.1$

2.2 MATERIAL MODELS.

The intact rock is treated as an isotropic, linear elastic and perfectly plastic material, with parameters summarized in Table 2-2. The plastic portion has an associated flow rule on a fixed (*i.e.*, non-hardening) two-invariant stress surface fitted to a Mohr-Coulomb failure condition in triaxial compression. (This is sometimes called a Mises-Schleicher material.)

Table 2-2. Material properties.

Property	Symbol	Value
Intact Mass Density	ρ	2500 kg/m ³
Intact Young's Modulus	E	30 GPa
Intact Poisson's Ratio	ν	0.25
Intact Cohesion	c	4.5 MPa
Intact Friction Angle	ϕ	25°
Intact Dilation Angle	ψ	25°
Intact Tensile Strength	T	2 MPa
Joint Normal Stiffness	k_N	$k_N = \frac{625}{(\delta - u_j)^2}$ kPa/m
Joint Shear Stiffness	k_S	1.25 GPa/m
Joint Cohesion	c_J	0
Joint Friction Angle	Φ	20°, except 30° in problem 2-S
Joint Dilation Angle	Ψ	0
Liner Young's Modulus	E_L	200 GPa
Liner Poisson's Ratio	ν_L	0.30
Liner Yield Strength	σ_{yL}	400 MPa
Liner Mass Density	ρ_L	7500 kg/m ³

To be more specific, the failure condition in terms of the principal stresses $\sigma_1, \sigma_2, \sigma_3$ (assumed positive in compression) can be written

$$f(\sigma_1, \sigma_2, \sigma_3) = 3J_2' - (a + bp)^2 = 0 \quad , \quad (2-1)$$

where $3J_2' = \sigma_1^2 + \sigma_2^2 + \sigma_3^2 - \sigma_1\sigma_2 - \sigma_2\sigma_3 - \sigma_3\sigma_1$ and $p = (\sigma_1 + \sigma_2 + \sigma_3)/3$. When this is fitted to a Mohr-Coulomb failure criterion in a state of triaxial compression ($\sigma_2 = \sigma_3 < \sigma_1$) we find the relation between (a, b) and (ϕ, c) to be

$$a = \frac{6c \cos \phi}{3 - \sin \phi} \quad , \quad b = \frac{6 \sin \phi}{3 - \sin \phi} \quad . \quad (2-2)$$

For the parameters given in Table 2-2 we have $a=9.49$ MPa, $b=0.984$.

This material specification is adopted for its computational simplicity. However, it is unphysical in that it leads to excessive dilatancy when compared with the response of real rocks. This needs to be kept in mind when assessing the results of problem 4, where—perhaps contrary to intuition, although not to certain lab and field observations—all calculators except one will be seen to predict that the tunnel suffers a *decrease* in the length of its springline (horizontal diameter). The one exception—LLNL—did not model the rock as a continuum and consequently could not possibly represent its plastic response accurately.

The joint behavior is also assumed to be elastic-plastic with a constant friction angle. However, the normal (opening/closing) elastic behavior is nonlinear, and the inelastic behavior is non-dilatant. The liner is elastic-perfectly plastic with a Mises failure condition and flow rule. Joint and liner property values are also listed in Table 2-2.

SECTION 3

STATEMENTS AND RESULTS FOR PROBLEMS WITH ANALYTICAL SOLUTIONS

3.1 ANALYTIC TREATMENT OF MATERIAL RESPONSE.

The first five problems (see Table 1-1) are quasi-static ones driven by boundary displacements which are consistent with homogeneous (uniform) strain throughout the region of interest. This does not mean that the actual strains *will* be uniform; if there are joints then actual strains will not be uniform. But in fact the stresses and strains in the intact rock and joint material will *separately* be homogeneous at each point of the imposed strain path. This opens the possibility of direct analytical solution of these problems for comparison with numerical results.

Another way of viewing the situation is that each of these problems reduces to nothing more than finding the response of a single implicit element around a specified strain path. This is strictly a material response question; equations of motion or compatibility among elements play no role whatsoever. It is curious to note that only one of the participants (CRT) produced single-element solutions to all of the first five problems.

All five of these problems can easily be written in terms of principal stresses $\sigma_1, \sigma_2, \sigma_3$ and strains $\epsilon_1, \epsilon_2, \epsilon_3$. Also, in no case will any strain exceed three percent, so a small-strain analysis is sufficient. As usual, the strain increments are decomposed into elastic and plastic parts

$$d\epsilon_1 = d\epsilon_1^{(e)} + d\epsilon_1^{(p)}, \quad (3-1)$$

with similar forms for $d\epsilon_2$ and $d\epsilon_3$. The elastic increments follow Hooke's law

$$d\epsilon_1^{(e)} = \frac{1}{E} [d\sigma_1 - \nu(d\sigma_2 + d\sigma_3)], \quad (3-2)$$

with similar forms for the other two components. The elastic response is easily invertible:

$$d\sigma_1 = \frac{E(1-\nu)}{(1+\nu)(1-2\nu)} \left[d\epsilon_1^{(e)} + \frac{\nu}{1-\nu} (d\epsilon_2^{(e)} + d\epsilon_3^{(e)}) \right]. \quad (3-3)$$

If $f(\sigma_1, \sigma_2, \sigma_3) < 0$, then the entire response is elastic and Eq. (3-3) fully describes the intact rock deformation. Moreover, since the coefficients are constant, Eq. (3-3) can be integrated by inspection over any change in strain.

The plastic increments follow from the associated flow law applied to the yield function (2-1):

$$d\varepsilon_1^{(p)} = \lambda \frac{\partial f}{\partial \sigma_1} = \lambda [\alpha \sigma_1 - \beta (\sigma_2 + \sigma_3) - \gamma] , \quad (3-4)$$

where λ is a constant (to be determined) and similar formulas obtain for the other components. In (3-4) the constants α, β, γ are given by

$$\alpha = 2 \left(1 - \frac{b^2}{9} \right) , \quad \beta = 1 + \frac{2b^2}{9} , \quad \gamma = \frac{2ab}{3} , \quad (3-5)$$

with (a, b) given by (2-2). When the intact rock is plastic, total strains are the sum of (3-2) and (3-4). An additional condition is that of continued yielding, which can either be written as Eq. (2-1) or

$$df = \frac{\partial f}{\partial \sigma_1} d\sigma_1 + \frac{\partial f}{\partial \sigma_2} d\sigma_2 + \frac{\partial f}{\partial \sigma_3} d\sigma_3 = 0 , \quad (3-6)$$

where the derivatives are given by formulas like the square-bracketed quantity in (3-4). The three principal stress increments can be found in terms of principal strain increments and current stresses by solving the system of ten equations (3-1), (3-3), (3-4), (3-6) in the ten unknowns $d\sigma_i, d\varepsilon_i^{(e)}, d\varepsilon_i^{(p)}, \lambda$. We will defer this step until discussing specific problems.

It will be useful to represent the joint normal response in terms of stress. According to Table 2-2 the joint stiffness is

$$k_N = \frac{d\sigma}{du_j} = \frac{A}{(\delta - u_j)^2} , \quad (3-7)$$

where $A=625$ kPa-in and u_j = joint closure. This can be rearranged to give

$$d\sigma = \frac{A du_j}{(\delta - u_j)^2} .$$

This can easily be integrated, giving

$$\sigma = \frac{A u_j}{(\delta - u_j) \delta} ,$$

which can be inverted to give

$$u_j = \frac{\delta^2 \sigma}{A + \sigma \delta} .$$

The stiffness (3-7) can now be written in terms of stress:

$$k_N = \frac{1}{A} \left(\frac{A}{\delta} + \sigma \right)^2 . \quad (3-8)$$

3.2 PROBLEM 1-IN: SPHERICALLY DIVERGENT STRAIN PATH IN INTACT ROCK

3.2.1 Statement of the Problem.

An intact rock sample is strained uniformly and quasi-statically along a strain path with two equal principal strains. This represents a spherically symmetric deformation, where the two hoop strains ϵ_θ are equal and generally different from the spherical radial strain ϵ_r . The geometry and strain path² are shown in Figure 3-1. The first leg is nearly uniaxial

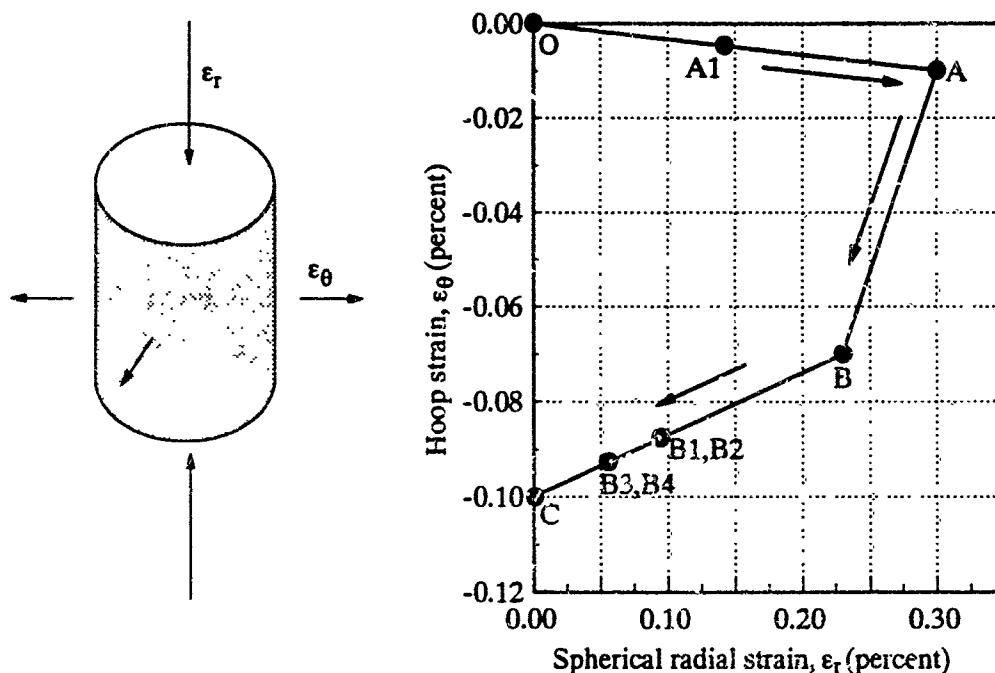


Figure 3-1. Geometry and loading in problems 1-IN and 1-IM.

²In this plot as well as throughout this report, strains and stresses are taken as positive in compression.

compression and represents the passage of a shock front. During the second leg, tensile hoop strain accumulates due to outward radial displacement. In the third leg, the radial strain is fully relieved but a residual tensile hoop strain remains. The problem is to find the stresses at each point along the given strain path.

3.2.2 Analytic Solution.

Let $\sigma_1 = \sigma_r$ and $\sigma_2 = \sigma_3 = \sigma_\theta$ be the spherical radial and hoop stresses respectively, and similarly for strains. From (3-2), the elastic response is

$$d\epsilon_r^{(e)} = \frac{1}{E}(d\sigma_r - 2\nu d\sigma_\theta) \quad , \quad d\epsilon_\theta^{(e)} = \frac{1}{E}[(1-\nu)d\sigma_\theta - \nu d\sigma_r] \quad , \quad (3-9)$$

with the inverse

$$d\sigma_r = \frac{E[(1-\nu)d\epsilon_r^{(e)} + 2\nu d\epsilon_\theta^{(e)}]}{(1+\nu)(1-2\nu)} \quad , \quad d\sigma_\theta = \frac{E(d\epsilon_\theta^{(e)} + \nu d\epsilon_r^{(e)})}{(1+\nu)(1-2\nu)} \quad . \quad (3-10)$$

In the elastic regime these equations govern the full response.

From (3-5) the plastic strain increments must obey

$$d\epsilon_r^{(p)} = 2\lambda \left(1 - \frac{b}{3}\right) (\sigma_r - \sigma_\theta) \quad , \quad d\epsilon_\theta^{(p)} = -\lambda \left(1 + \frac{2b}{3}\right) (\sigma_r - \sigma_\theta) \quad . \quad (3-11)$$

The differential form of the continuing yield condition (3-6) reduces to

$$\left(1 - \frac{b}{3}\right) d\sigma_r - \left(1 + \frac{2b}{3}\right) d\sigma_\theta = 0 \quad . \quad (3-12)$$

Equations (3-9), (3-11), and (3-12) combine with the two independent forms of (3-1) to provide seven linear equations in the unknowns $(d\epsilon_r^{(e)}, d\epsilon_\theta^{(e)}, d\epsilon_r^{(p)}, d\epsilon_\theta^{(p)}, d\sigma_r, d\sigma_\theta, \lambda)$. They can be solved for the stress increments during plastic loading, giving

$$\begin{aligned} d\sigma_r &= \frac{E(3+2b)[(3+2b)d\epsilon_r + 2(3-b)d\epsilon_\theta]}{27(1-2\nu) + 6b^2(1+\nu)} \quad , \\ d\sigma_\theta &= \frac{E(3-b)[(3+2b)d\epsilon_r + 2(3-b)d\epsilon_\theta]}{27(1-2\nu) + 6b^2(1+\nu)} \quad . \end{aligned} \quad (3-13)$$

Note that with the given yield function and flow rule, not only the elastic formula (3-10) but the elastic-plastic one (3-13) as well are linear with *constant* coefficients. Thus as long as $d\epsilon_\theta/d\epsilon_r$ is constant, the finite stress increments obey the same equations as the infinitesimals.

To compute the evolution of stresses along the strain path of Figure 3-1, we must proceed in steps, beginning with elastic response. On the initial leg OA we have $d\epsilon_\theta/d\epsilon_r = -1/30$.

The stresses at any point along the leg are those at the beginning—0 in this case—added to the increments. Combining this strain increment ratio with (3-10) we find

$$\frac{d\sigma_{\theta}}{d\sigma_r} = \frac{30\nu - 1}{30 - 32\nu} = 0.2954 \quad (3-14)$$

This holds until yielding, and in this case gives the ratio of stresses themselves since they both started at 0. For this axisymmetric stress state the yield condition (2-1) can be recast

$$f = |\sigma_r - \sigma_{\theta}| - \left[a + \frac{b}{3}(2\sigma_r + \sigma_{\theta}) \right] = 0 \quad (3-15)$$

Equation (3-14) and (3-15) solved simultaneously give the stresses at first yield, labeled point A1 in Table 3-1. The strains at this point follow from (3-9).

Table 3-1. Analytic solution to problem 1-IN.

Point	Time	Radial Stress σ_r (MPa)	Hoop Stress σ_{θ} (MPa)	Pressure p (MPa)	Stress Difference $\sigma_r - \sigma_{\theta}$ (MPa)	Radial Strain ϵ_r (percent)	Hoop Strain ϵ_{θ} (percent)	Volume Strain (percent)
O	0.	0.	0.	0.	0.	0.	0.	0.
A1	0.49	51.9	15.3	27.5	36.6	0.148	-0.005	0.138
A	1.	104.8	26.8	59.5	68.0	0.3	-0.01	0.28
B	2.	62.5	19.6	33.9	42.9	0.23	-0.07	0.09
B1	2.59	9.2	-2.	1.7	11.2	0.095	-0.088	-0.08
B2	2.59	10.2	0.	3.4	10.2	0.095	-0.088	-0.08
B3	2.76	-2.	0.	-0.7	-2.	0.054	-0.093	-0.13
B4	2.76	0.	0.	0.	0.	0.054	-0.093	-0.13
C	3.	0.	0.	0.	0.	0.	-0.1	-0.2

Once yielding occurs, equations (3-13) obtain. These two equations together with the strain-path slope $\epsilon_{\theta}/\epsilon_r = -1/30$ give the remaining response on leg OA as a function of (say) $d\epsilon_r$, and the final value $\epsilon_r = 0.3$ defines point A.

When the strain path direction changes at point A, we can tell if the next increment is elastic or plastic by supposing that it is elastic ("taking a trial elastic increment"), in which case

from (3-10) with $d\epsilon_\theta/d\epsilon_r=6/7$ we find $d\sigma_\theta/d\sigma_r=31/33$. With $\sigma_r>\sigma_\theta$ and $b=0.984$ the increment in the yield function (3-15) would be

$$df = d\sigma_r \left[1 - \frac{2b}{3} - \frac{d\sigma_\theta}{d\sigma_r} \left(1 + \frac{b}{3} \right) \right] = -0.904 d\sigma_r \quad (3-16)$$

With $d\sigma_r<0$ the trial increment would cause f to go positive, which is prohibited; therefore leg AB must start with an elastic-plastic increment. Starting from the known state at A, as before we use (3-13) and the strain-path slope $d\epsilon_\theta/d\epsilon_r=6/7$ to find the changes in stresses as a function of (say) $d\epsilon_r$. Provided the tensile failure criterion is not met, the response will continue in the elastic-plastic mode until the next change in strain-path direction.

The tensile limit is given as 2 MPa, but no other details of the tensile failure law are specified. In this analysis we assume this limit applies separately to each principal stress, and once it is exceeded, that stress is set to zero.

Tensile failure therefore does not occur before reaching point B, so we can fill in the state at B according to elastic-plastic response.

The beginning of leg BC is treated the same as was AB, and is likewise found to be elastic-plastic. As before, the strain and stress increment ratios give the direction of the stress path, and the starting point is known from the previous leg. The hoop stress is the first to reach the tensile limit. Here the hoop stress changes abruptly from -2MPa (point B1) to 0 (point B2), while the radial strain remains fixed. The macroscopic hoop strain also stays fixed, but after cracking, it will contain a portion due to the crack, while the intact material will contract in the hoop directions. Assuming the stress adjustments during crack formation are elastic, from (3-9)₁ with $d\epsilon_r=0$ and $d\sigma_\theta=+2$ MPa we find $d\sigma_r=1$ MPa. This completes the state at B2. (A yield function check verifies that the stress adjustment was indeed elastic.)

The next leg is (as a trial) taken to be elastic, with $\sigma_\theta=0$. Equation (3-9) then giving $d\sigma_r=E d\epsilon_r$. Radial tensile failure occurs as σ_r reaches -2 MPa at point B3. Now the radial stress also drops to 0 (point B4) with no change in macroscopic strain, and remains there until the end of the strain path at point C.

3.2.3 Numerical Solutions.

The compressibility and stress paths from the various numerical solutions to problem 1-IN are shown in Figures 3-2 and 3-3 respectively. The most obvious feature of these comparisons is the inadequacy of the LLNL approach for representing stresses in intact rock. It has the wrong stiffness, volumetric hysteresis, and stress path over the full duration of the problem. Among the other curves up to the point of tensile failure, all agree well except for slightly low unloading pressures in the CRT model. The final leg of the compressibility curve suggests that all the numerical models except RE/SFEC's used a criterion based on pressure rather than principal stress, and that after tensile failure some held the pressure at the cutoff value rather than fixing it at 0. Differences in intact rock tensile failure models are probably of negligible consequence to tunnel failure in jointed media.

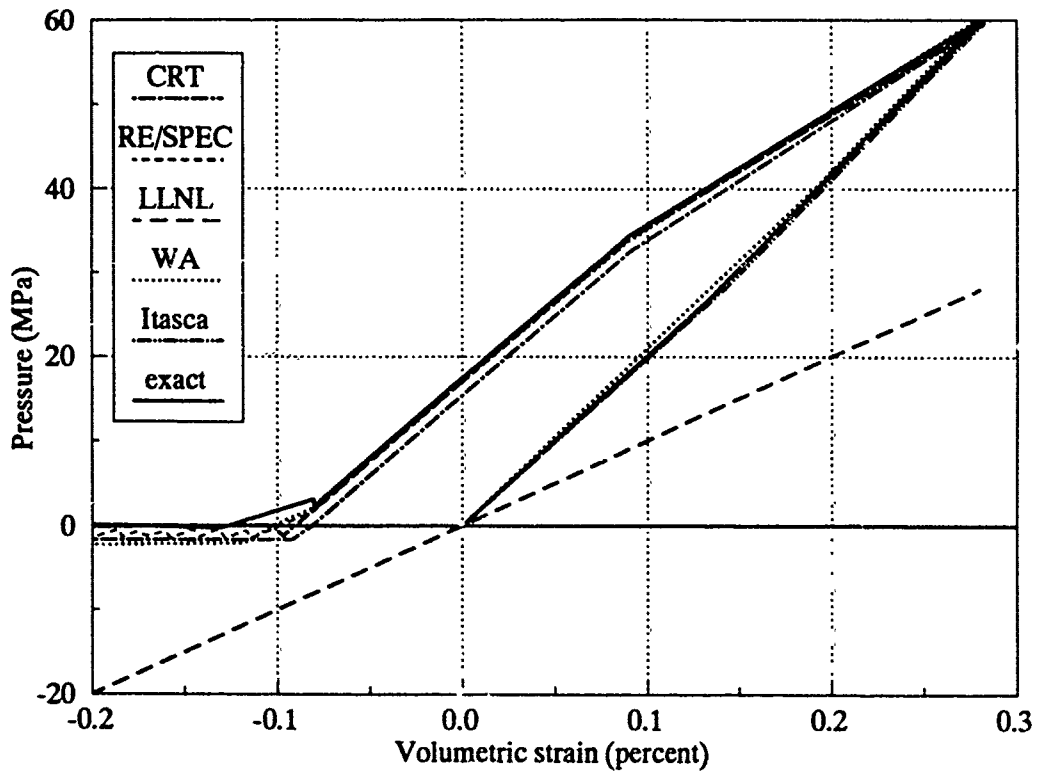


Figure 3-2. Intact rock compressibility in problem 1-IN.

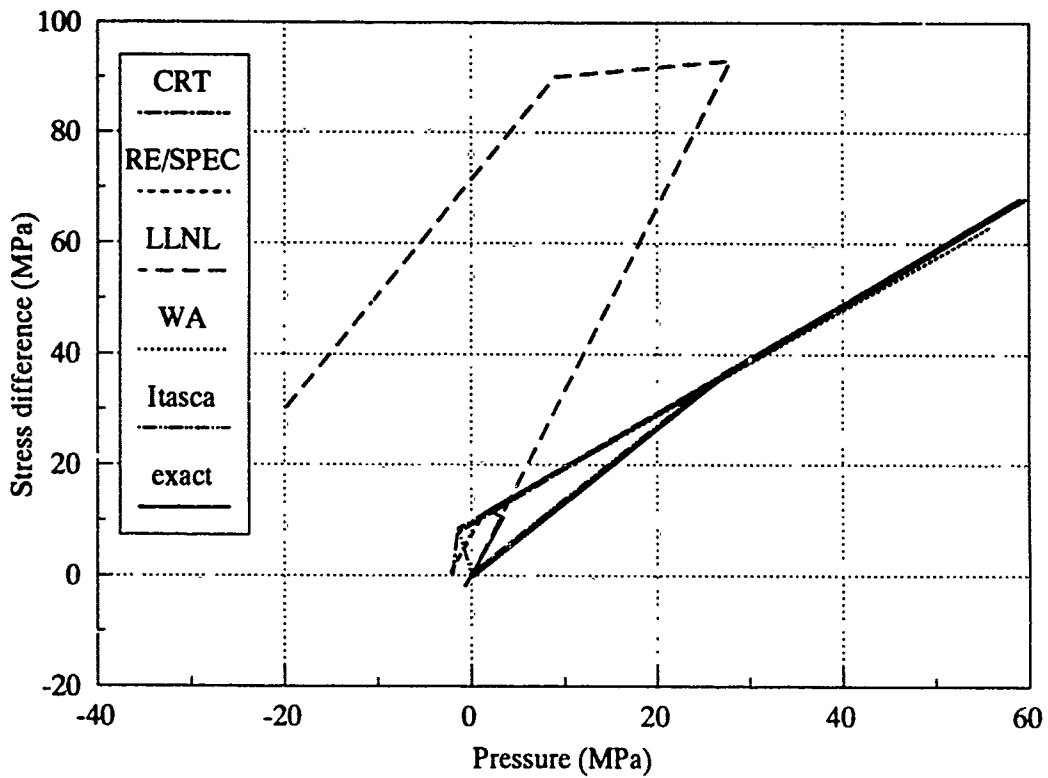


Figure 3-3. Intact rock stress path in problem 1-IN.

3.3 PROBLEM 1-IM: SPHERICALLY DIVERGENT STRAIN PATH IN IMPLICITLY JOINTED ROCK.

3.3.1 Statement of the Problem.

The only difference between this problem and the previous one, problem 1-IN, is the material, which now contains two perpendicular joint sets modelled implicitly. One joint set is assumed to be normal to the r -direction (horizontal in Figure 3-1). Joint properties are given in Tables 2-1 and 2-2.

3.3.2 Analytic Solution.

The introduction of implicit jointing profoundly affects the solution in several ways: by compounding the rock and joint response in each individual direction, by introducing nonlinearity on account of the joint's nonlinear normal stiffness, and by upsetting the axisymmetry on account of the effective anisotropy induced by the joints. The principal stresses still align with coordinate directions and joints, so there are still no shear stresses or shear displacements across joints, and it still suffices to consider only the normal stresses, strains, and displacements.

For this discussion, let the z -axis align with the r -direction and the normal to one joint set, and the x -axis with the other joint set. Consider the displacement increments for a single joint and intervening intact rock (i.e., a 1-m cube):

$$\begin{aligned} du_x &= du_x^I + du_x^J = w_x d\epsilon_x^I + \frac{d\sigma_x^J}{k_x} , \\ du_y &= du_y^I = w_y d\epsilon_y^I , \\ du_z &= du_z^I + du_z^J = w_z d\epsilon_z^I + \frac{d\sigma_z^J}{k_z} , \end{aligned} \quad (3-17)$$

where superscripts I, J refer to intact material and joints respectively, and $w_x = w_y = w_z = 1$ m. The joint thickness has been neglected compared with the block width in relating intact rock strains to the corresponding displacements. Recall that the joint stiffnesses k_x, k_z depend respectively on the stresses σ_x, σ_z according to (3-8). Combining (3-17) with the elastic constitutive law (3-2) gives

$$\begin{bmatrix} \left(1 + \frac{E}{w_x k_x^J}\right) & -\nu & -\nu \\ \vdots & 1 & -\nu \\ \text{symmetric} & \dots & \left(1 + \frac{E}{w_z k_z^J}\right) \end{bmatrix} \begin{bmatrix} d\sigma_x \\ d\sigma_y \\ d\sigma_z \end{bmatrix} = \begin{bmatrix} \frac{E du_x}{w_x} \\ \frac{E du_y}{w_y} \\ \frac{E du_z}{w_z} \end{bmatrix} \quad (3-18)$$

This system of three linear equations must be solved simultaneously to get the elastic stress increments corresponding to given displacement increments du_x , du_y , du_z . The system as a whole is nonlinear, because the joint stiffnesses, and consequently the coefficients in (3-18), depend on the current stress level.

Three of the equations governing stress increments in the plastic regime are found by combining the elastic strain increments (3-2) with the plastic ones (3-4) and substituting the sum into (3-17). A new unknown λ has been introduced, and the fourth and last required equation is the condition of continuing plastic yielding (3-6). The partial derivatives take the form of the square-bracketed quantity in (3-4). The resulting system of four equations in four unknowns is

$$\begin{bmatrix} \left(1 + \frac{E}{w_x k_x^J}\right) & -\nu & -\nu & E[\alpha\sigma_x - \beta(\sigma_y + \sigma_z) - \gamma] \\ \vdots & 1 & -\nu & E[\alpha\sigma_y - \beta(\sigma_x + \sigma_z) - \gamma] \\ \vdots & \left(1 + \frac{E}{w_z k_z^J}\right) & & E[\alpha\sigma_z - \beta(\sigma_x + \sigma_y) - \gamma] \\ \text{symmetric} & \dots & & 0 \end{bmatrix} \begin{bmatrix} d\sigma_x \\ d\sigma_y \\ d\sigma_z \\ \lambda \end{bmatrix} = \begin{bmatrix} \frac{E du_x}{w_x} \\ \frac{E du_y}{w_y} \\ \frac{E du_z}{w_z} \\ 0 \end{bmatrix} \quad (3-19)$$

where in the axisymmetric problem at hand we have $du_x/w_x = du_y/w_y = d\epsilon_\theta$, $du_z/w_z = d\epsilon_r$. Note that the matrix in (3-19) is symmetric. This is a consequence of the associated plastic flow law.

Either system (3-18) or (3-19) could be inverted in closed form if desired. However, the stress dependence of the resulting expressions for the stress increments would render them very difficult if not impossible to integrate in closed form. Therefore it was decided to perform both the inversion and the integration numerically. The procedure for each time step is as follows:

- (1) Solve the elastic equations (3-18), using current stresses, for trial stress increments due to current displacement increments. Note that overall strain increments in the problem specification (Figure 3-1), when applied to the 1-m cube, are numerically equal to the displacements in meters appearing on the right-hand sides of equations (3-18) or (3-19). A crude predictor-corrector is effected by updating the stresses and then re-solving the equations.
- (2) Check whether the yield criterion is violated by the current stresses augmented by the trial increments. If not, the current increment is elastic and the computed trial values are retained as actual values.
- (3) If the current state is elastic but the trial values violate the yield criterion, linearly interpolate back to the place where $f=0$, reset the time axis to this point, and move forward from there with a plastic increment based on equations (3-19).
- (4) If the current state is plastic, first conduct an elastic trial as above. If the trial state is elastic, update immediately (no interpolation is needed); if not, compute a plastic increment from (3-19) and update immediately.

It was not deemed of sufficient interest to pursue this computation beyond tensile failure, so it was simply terminated when any principal stress reached the tensile limit. The results are given with the numerical solutions in the following section.

3.3.3 Numerical Solutions.

Only CRT and RE/SPEC submitted numerical solutions to this problem. Because it is not axisymmetric, the stress difference $\sigma_z - \sigma_x$ is not equal to $(3J_2')^{1/2}$, so three plots of results are given. Figures (3-4), (3-5), and (3-6) indicate that prior to tensile failure, both numerical results are quite close to the analytical one. After that, although the analytic solution has not been carried this far, CRT's compressibility curve cannot be correct, since it does not terminate at a volumetric strain of -0.2 percent. However, as noted, this portion of the curve is not of particular interest in this problem.

3.4 PROBLEMS 2-EX AND 2-IM: UNIAXIAL STRAIN OF A "STACK OF BRICKS".

3.4.1 Statement of the Problem.

A 4-by-5-by-1-m volume is filled with 1-m cubes of rock separated by joints as shown in Figure 3-7. There are no joints parallel to the plane of the figure. Five sides have roller boundaries. The top is displaced vertically and quasi-statically as indicated in the figure, while shear traction is held at zero. Half-thickness joints separate full blocks from the three roller boundaries normal to the plane of the figure.

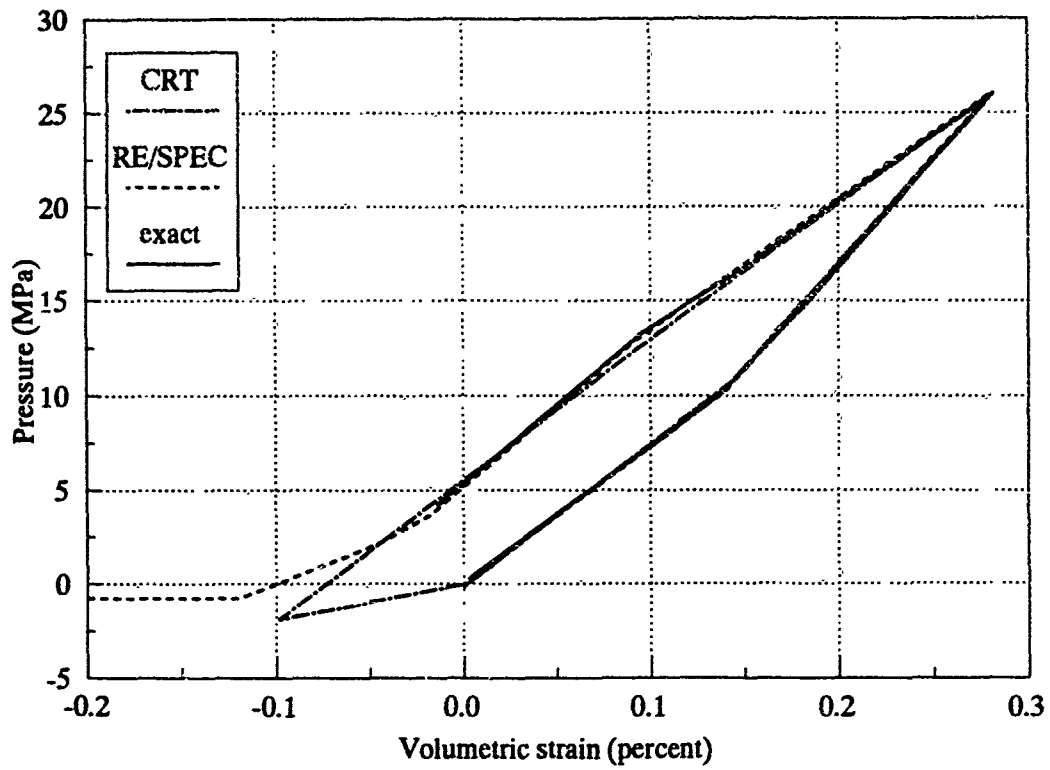


Figure 3-4. Implicitly jointed rock compressibility in problem 1-IM.

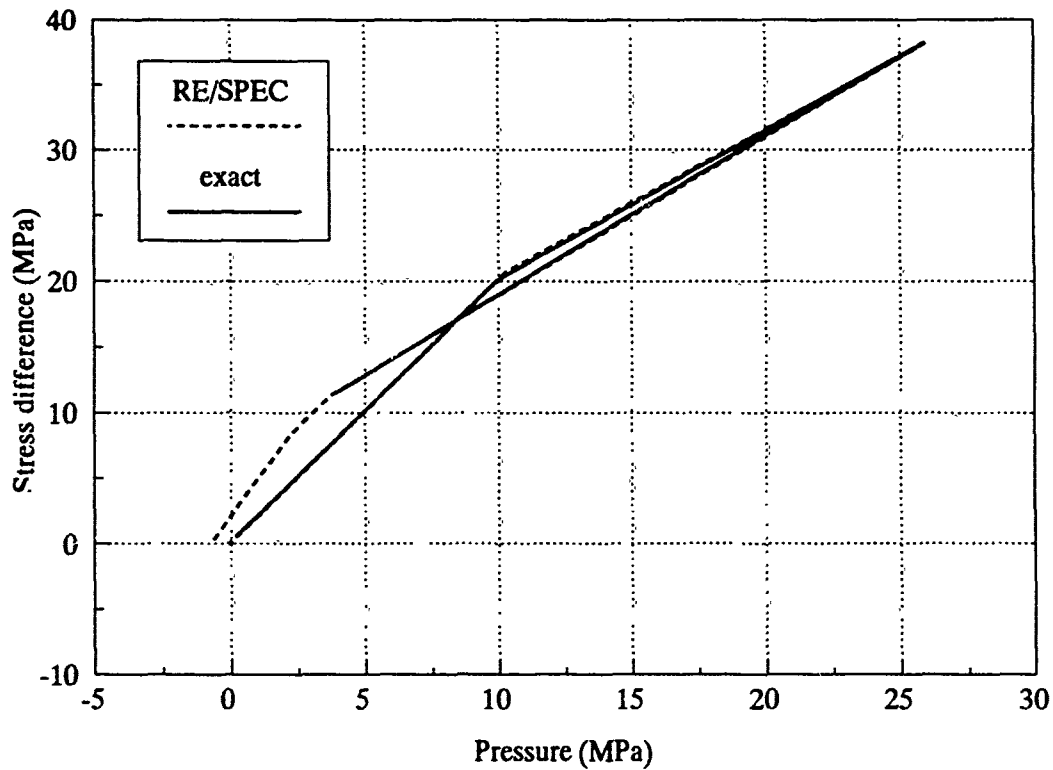


Figure 3-5. Implicitly jointed rock stress difference vs. pressure in problem 1-IM.

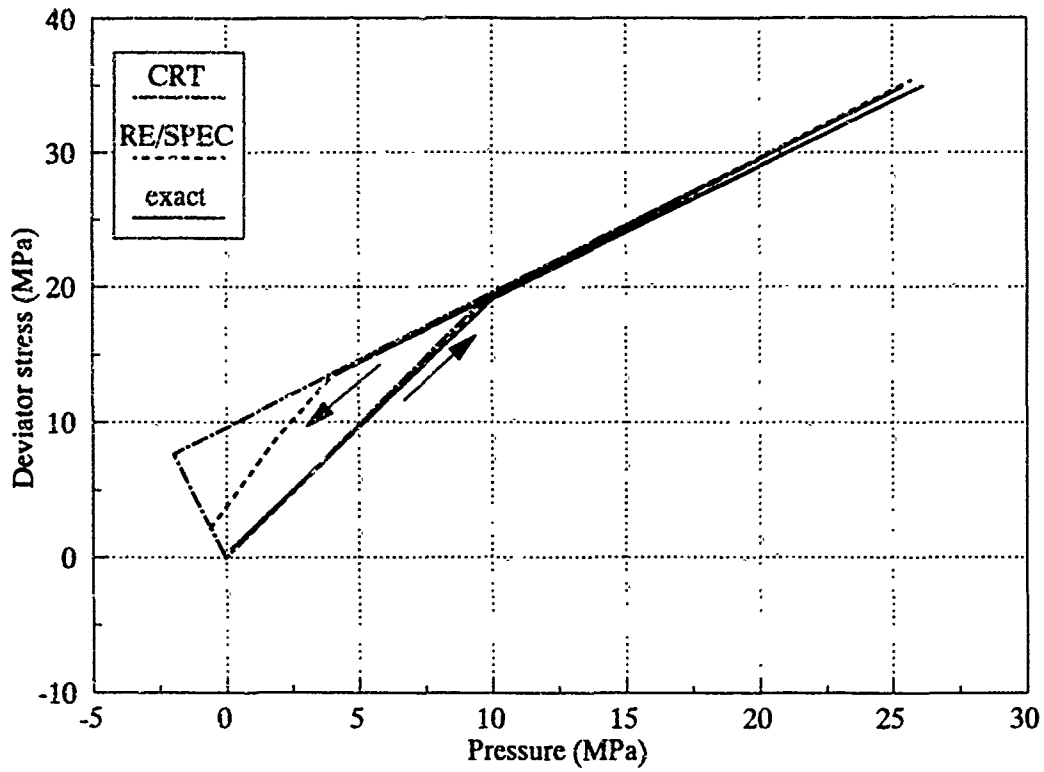
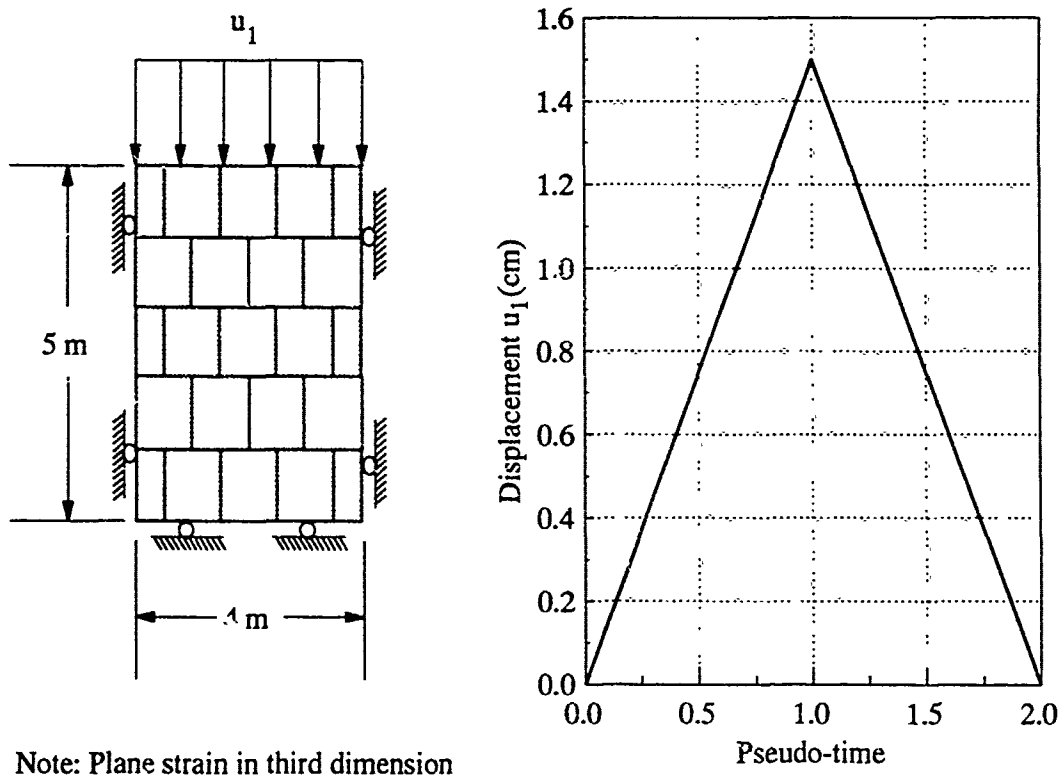


Figure 3-6. Implicitly jointed rock effective stress $(J_2')^{1/2}$ vs. pressure in problem 1-IM.



Note: Plane strain in third dimension

Figure 3-7. Geometry and loading in problems 2-EX and 2-IM.

3.4.2 Analytical Solution.

No distinction between implicit and explicit rock models needs to be made for the purpose of deriving the analytic solution to this problem. The stated conditions lead to stresses and strains identical to those in an *infinite* region with the same joint spacing and homogeneous macroscopic strain. The principal directions of the geometry will coincide with principal directions of stress and strain. Equations (3-18) and (3-19) from the previous section govern a single, representative 1-m cubic element under these conditions. (The staggering in the jointing only affects deformations at a much higher level of accuracy than considered here.) Therefore, the analytic solution to this problem follows exactly the same procedure as problem 1-IM. The only difference is the right-hand side of (3-18) or (3-19), where now $du_x = du_y = 0$, and (for a single 1-m element) u_z will increase quasistatically up to 0.3 cm and then decrease to zero. The results of the step-by-step numerical integration are shown in Figures 3-8 and 3-9.

3.4.3 Numerical Solutions.

Figures 3-8 and 3-9 also show the compressibility and stress path according to the various explicit numerical joint models. In each plot two curves stand out. The LLNL model again has incorrect stiffness, hysteresis, and deviator stresses. It does appear to agree with the initial slope of the compression loading curve, but not to stiffen on loading as it should due to the joint's nonlinear elastic compressive behavior.

The WA model has incorrect stiffness and excessive numerical chatter. The reason for the former is that in the joint treatment used in this problem, joint stiffness was fixed solely by numerical considerations related to the detection of and compensation for node penetration across joints. There was no other mechanism to include a specified normal joint stiffness, so it was ignored. The required numerical stiffness appears to have been much greater than that specified for the joint, leading to stiffer overall response. That the WA stiffness is roughly twice the correct value is consistent with the fact that at least according to specifications in the elastic regime, the contributions of the intact rock and joints to the overall stiffness are about equal. Subsequent to this calculation, the joint model was modified to admit a specified normal elastic stiffness in place of the former, numerically driven value.

The excessive chatter in both compressibility and stress path in the WA calculation is also caused by the joint model. WA explicitly modelled every individual block and interface shown in Figure 3-7. Subsequent to this problem, WA modified the treatment of joint forces at the corners of blocks and believes that these modifications are responsible for the improvement in the model's behavior in subsequent problems. (Appendix E contains a brief description of the modelling approach and the modifications.)

Numerical results for problem 2-IM are shown in Figures 3-10 and 3-11 together with the analytical solution. Again, only CRT and RE/SPEC submitted solutions based on implicit joint models, and both agree closely with the analytical results.

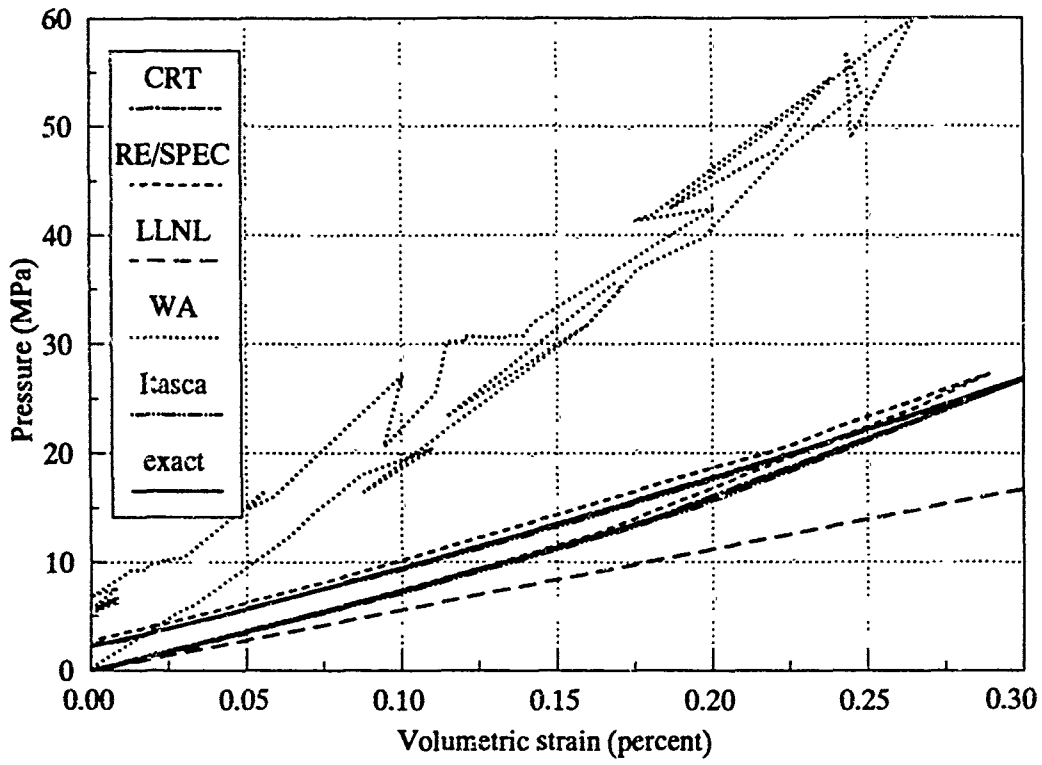


Figure 3-8. Jointed rock compressibility in problem 2-EX.

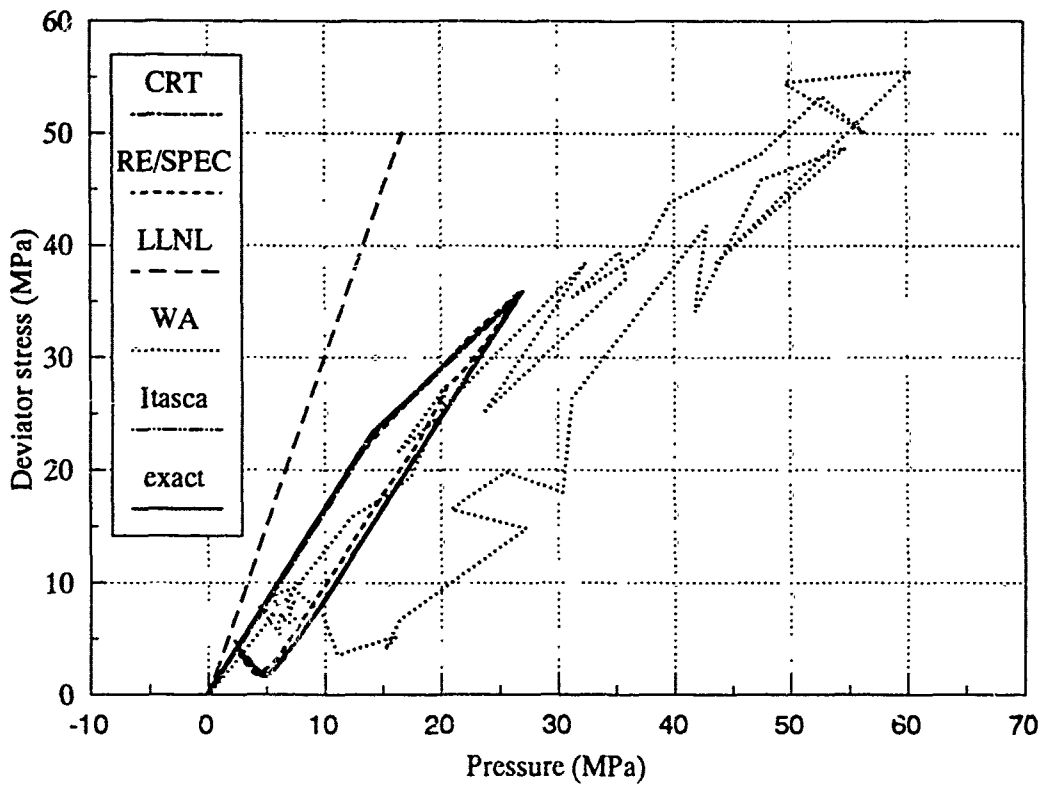


Figure 3-9. Stress path in problem 2-EX.

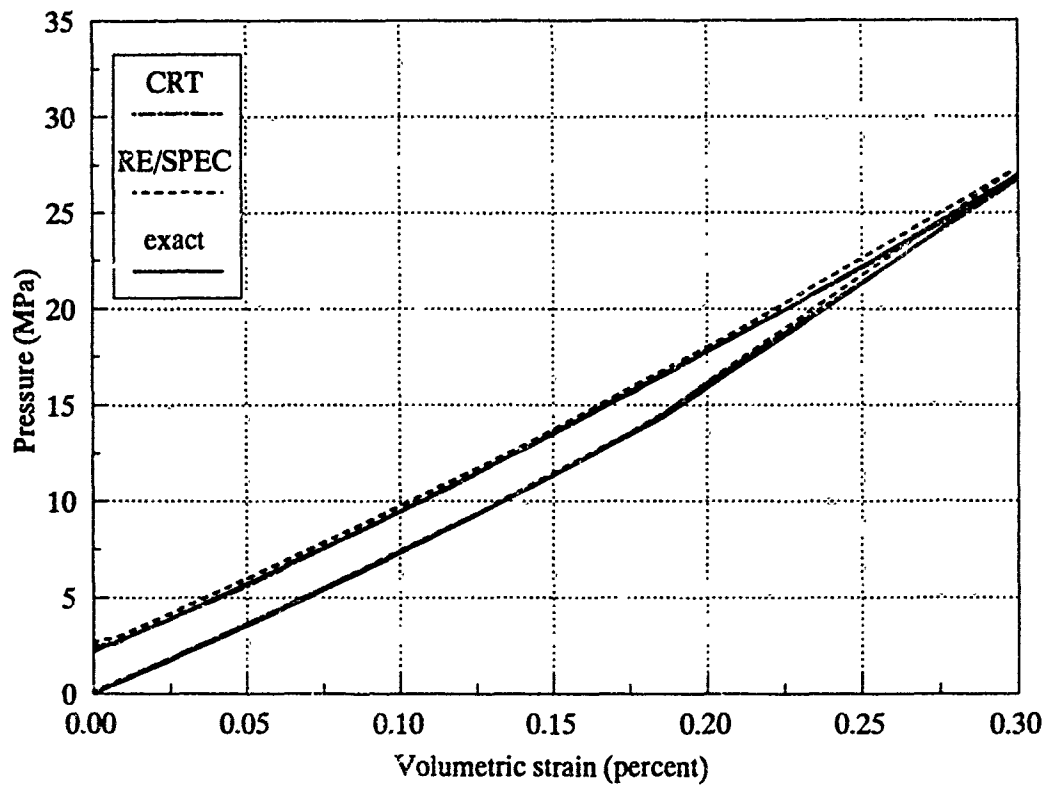


Figure 3-10. Compressibility in problem 2-IM.

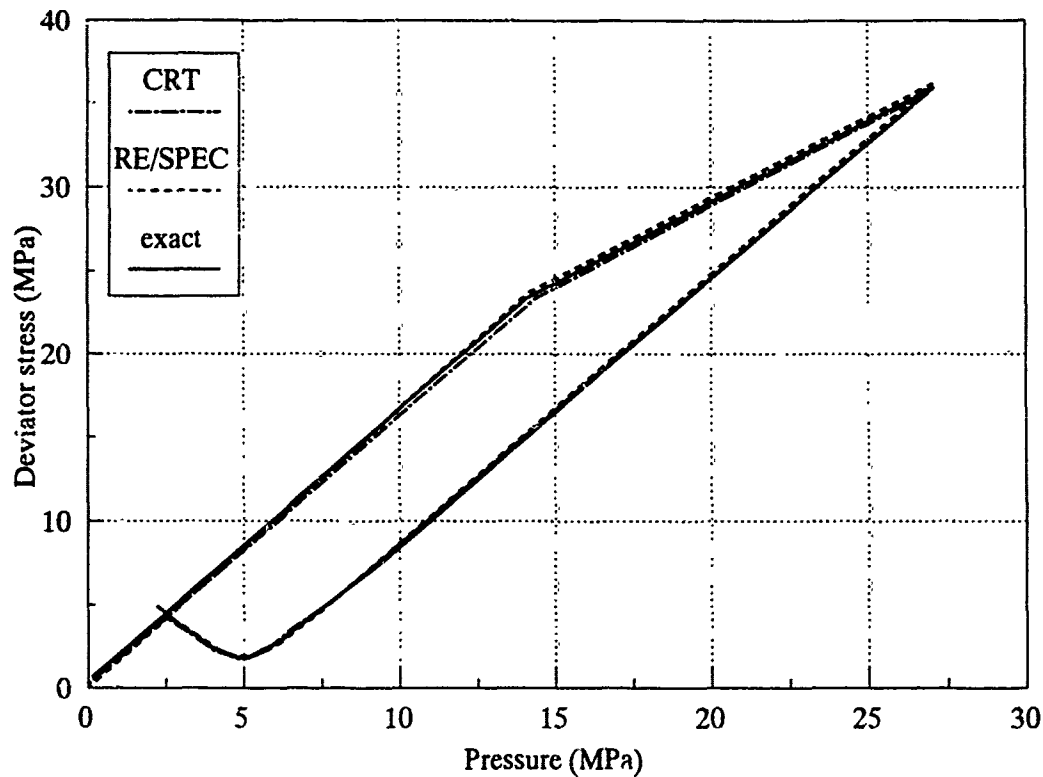


Figure 3-11. Stress path in problem 2-IM.

3.5 PROBLEM 2-S: SHEARING OF TWO TRIANGULAR BLOCKS SEPARATED BY A SINGLE JOINT.

3.5.1 Statement of the Problem.

Since none of the foregoing problems exercised the joint in shear, this problem was devised to do just that, and to do so while maintaining a homogeneous strain state in the intact rock. Two blocks of intact rock are separated by a diagonal joint as shown in Figure 3-12. Plane strain applies out of the plane of the figure. Normal displacements are imposed on the upper and right-hand faces, while maintaining zero shear traction. The remaining boundaries are rollers. As a function of time in arbitrary units, the displacements are given in Table 3-2, with linear variations between tabulated values. The displacements follow the path indicated in the figure. The objective is to find the stress histories in the block. The problem is to be solved with an explicit joint model, but an implicit model may be tried in addition.

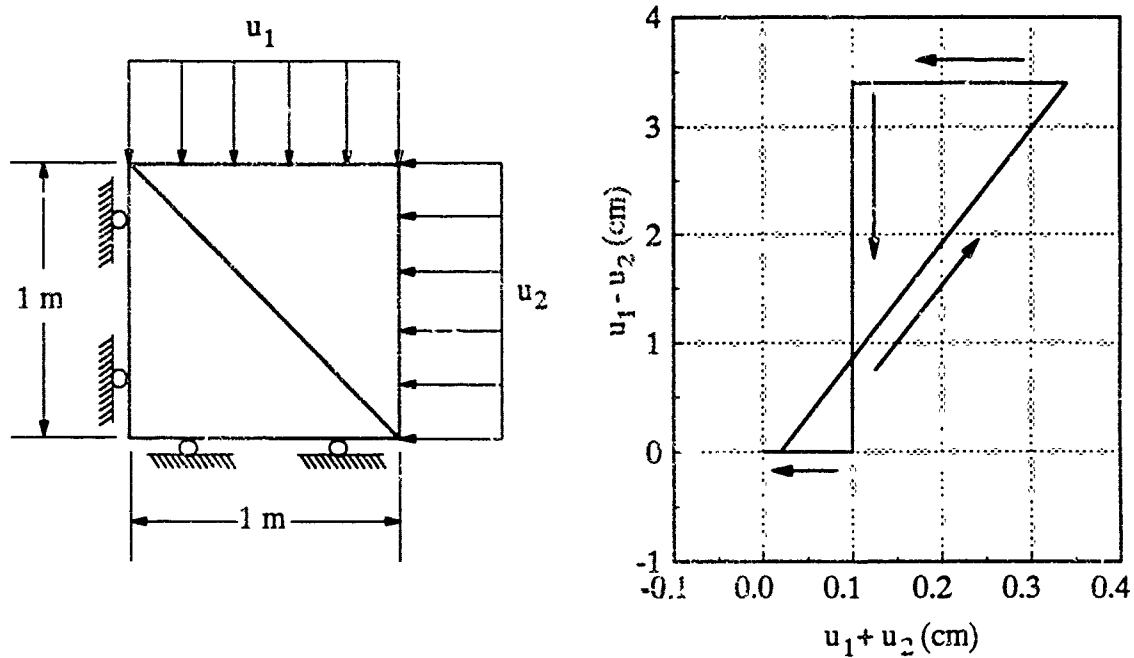


Figure 3-12. Geometry and loading in problem 2-S.

Table 3-2. Imposed boundary displacements in problem 2-S.

Time (Arbitrary units)	u_1 (m)	u_2 (m)
0	0	0
1	0.0001	0.0001
2	0.0187	-0.0153
3	0.0175	-0.0165
4	0.0005	0.0005
5	0	0

3.5.2 Analytical Solution.

3.5.2.1 Outline of the solution procedure. The problem will be treated by an incrementally linear scheme. At the beginning of each time step the stresses, boundary displacements, total joint slip, and pending displacement increments are known, and the stress increments and total joint slip increment are to be found. Once the increments are found, the corresponding quantities are updated and the process repeated.

For quasi-static deformations, this problem can be put into the same form as the more conventional one of elastic-plastic deformation with two intersecting, non-hardening failure surfaces. One surface is the standard one for the intact material; the other is the locus in stress-space of points satisfying the conditions for Mohr-Coulomb frictional slip. Plastic flow in intact rock is associated, while the effective plastic strain due to joint slip is not associated with the joint failure function. Table 3-3 lists the four potential deformation modes, and assigns a name and number to each.

Table 3-3. Potential deformation modes in problem 2-S.

Mode number	Mode name	Intact response	Joint response
1	EE	Elastic	Elastic (not slipping)
2	EP	Elastic	Plastic (slipping)
3	PE	Plastic	Elastic
4	PP	Plastic	Plastic

For each potential mode, a corresponding set of stress increments can always be obtained. The formulas will be given below. If the problem is well-posed, then one and only one of these four sets will be admissible, because together they comprise all of the possibilities. The criteria for admissibility are that the stresses at the end of the increment be inside or on the appropriate failure surface(s), and that the plastic strain increments for the active plastic mode(s) be in the correct direction. The former requirement is equivalent to the negativity or vanishing of the failure function f^I or f^J . For the intact rock, the latter requirement is that the proportionality constant λ^I relating plastic strain increments to stress derivatives of the flow potential, be positive. For the joint, the condition is that the increment of slip must be in the same direction as the total shear stress across the joint. While no analytical proof of uniqueness is available, it will be found numerically for the prescribed boundary displacement history that at every time step there is one and only one admissible solution among the four alternatives.

The computational procedure for each time step will begin with the evaluation of a number of "trial" increments, the number and type depending on the location of the stress point at the start of the increment.³ Specifically, only increments of types which cannot be ruled out a priori, based on the starting point, will be considered. For example, if the starting point is EE, i.e., both failure functions are negative and the stress point is inside both failure surfaces, then only an EE increment need be considered. If starting with an EP stress state, where the stress point is on the joint failure surface but inside the one for intact material, the increment must be either EP or EE. If a trial increment causes the stress point to cross a failure surface, then linear interpolation is used to shorten the current time step such that the stress point will be right on the failure surface at the end of the time step. This ensures that only a single deformation mode occurs during the entire time step.

Table 3-4 is a road map of the entire computational scheme. The second column lists the types of trial increments that cannot be ruled out a priori for each starting stress point location (column 1) and are therefore computed and checked for admissibility. Conditions for admissibility are listed in the third column in terms of failure functions and plastic flow proportionality constants. (Although we will not explicitly write the joint slip increment in the form of a constant multiplying the gradient of a flow potential, it could be done. In the table, " $\lambda^{J*} > 0$ " is simply shorthand for "the slip increment is in the same direction as the total shear stress across the joint.") The superscript "*" refers to a trial value, so for example $f^{I*} = f^I(\sigma + d\sigma^*)$ where σ is the stress at the start of the time step and $d\sigma^*$ is the trial stress increment. The fourth column indicates the final resolution for the time step, based on which pair of admissibility conditions holds. In some cases the trial increment itself becomes the actual stress increment. In others, where the trial increment caused the stress point to cross a failure surface, an interpolation based on failure function values is applied to scale back both the stress increment and the time step such that the end point is just on the failure surface(s).

³These "trial" increments should not be confused with the trial elastic increment used in most explicit dynamic codes.

Table 3-4. Road map for computational scheme used in problem 2-S.

Stress state at start of time step	Trial increment types	Admissible outcomes (see note A)	Action if condition in column 3 holds	Stress state at end of time step
EE	EE	$f^{I*} < 0, f^{J*} < 0$	$d\sigma = d\sigma^*$	EE
		$f^{I*} < 0, f^{J*} > 0$	$d\sigma = \theta^J d\sigma^*$	EP
		$f^{I*} > 0, f^{J*} < 0$	$d\sigma = \theta^I d\sigma^*$	PE
		$f^{I*} > 0, f^{J*} > 0$	(See note B)	EP or PE
EP	EE	$f^{I*} < 0, f^{J*} < 0$	$d\sigma = d\sigma^*$	EE
		$f^{I*} > 0, f^{J*} < 0$	$d\sigma = \theta^J d\sigma^*$	PE
	EP	$f^{I*} < 0, \lambda^{J*} > 0$	$d\sigma = d\sigma^*$	EP
		$f^{I*} > 0, \lambda^{J*} > 0$	$d\sigma = \theta^J d\sigma^*$	PP
PE	EE	$f^{I*} < 0, f^{J*} < 0$	$d\sigma = d\sigma^*$	EE
		$f^{I*} < 0, f^{J*} > 0$	$d\sigma = \theta^J d\sigma^*$	EP
	PE	$\lambda^{I*} > 0, f^{J*} < 0$	$d\sigma = d\sigma^*$	PE
		$\lambda^{I*} > 0, f^{J*} > 0$	$d\sigma = \theta^J d\sigma^*$	PP
PP	EE	$f^{I*} < 0, f^{J*} < 0$	$d\sigma = d\sigma^*$	EE
	EP	$f^{I*} < 0, \lambda^{J*} > 0$	$d\sigma = d\sigma^*$	EP
	PE	$\lambda^{I*} > 0, f^{J*} < 0$	$d\sigma = d\sigma^*$	PE
	PP	$\lambda^{I*} > 0, \lambda^{J*} > 0$	$d\sigma = d\sigma^*$	PP

Note A: For uniqueness, only one of the four conditions will hold.

Note B: This condition, corresponding to an EE starting point very near the intersection and a strain increment outside both surfaces, never occurred but could be handled if necessary.

For example, the constant θ^J , which must fall in the range (0,1), is defined by

$$\theta^J = \frac{-f^I(\sigma)}{f^I(\sigma + d\sigma^*) - f^I(\sigma)}$$

Finally, the last column shows the location of the stress point at the end of the time step.

3.5.2.2 Analytical preliminaries. As before, we decompose the displacements into parts separately due to intact material and the joint:

$$\begin{aligned} u_x &= u_x^I + u_x^J = w\epsilon_x^I + u_x^J, \\ u_z &= u_z^I + u_z^J = w\epsilon_z^I + u_z^J, \quad u_y = u_y^I = 0, \end{aligned} \quad (3-20)$$

where the last relation expresses the plane strain condition in the absence of any joints normal to the y-axis. As indicated by the vector diagram in Figure 3-13, the parts of the total displacement due to motion across the joint can be further decomposed into components normal and tangential to the joint. These are respectively denoted u_N^J (positive in compression) and u_S^J (positive when the upper block moves down and to the right), and are given by

$$u_z^J = \frac{u_N^J + u_S^J}{\sqrt{2}}, \quad u_x^J = \frac{u_N^J - u_S^J}{\sqrt{2}}. \quad (3-21)$$

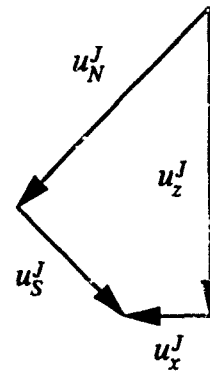


Figure 3-13. Decomposition of joint displacements

The symmetries of this problem guarantee that the only nonvanishing stresses in the x-y-z coordinate system are the normal stresses in the coordinate directions. By a 45-degree cw coordinate rotation, these give rise to the following normal and shear stresses across the joint:

$$\sigma_N^J = \frac{\sigma_z + \sigma_x}{2} = \bar{\sigma}, \quad \tau_S^J = \frac{\sigma_z - \sigma_x}{2} = \frac{\Delta\sigma}{2}, \quad (3-22)$$

In view of the form of (3-22) and other factors that lead to later simplification, we will regard the fundamental stress unknowns to be $\bar{\sigma}$, $\Delta\sigma$, σ_y , and will seek equations for the increments in these quantities in terms increments in the correspondingly defined quantities \bar{u} , Δu , $u_y (=0)$.

In preparation for that, by combining equations (3-7), (3-8), (3-21), and (3-22), the joint response law can be written in the form

$$d\bar{u}^J = \frac{du_z^J + du_x^J}{2} = \frac{du_N^J}{\sqrt{2}} = \frac{du_N^{Je}}{\sqrt{2}} = \frac{d\bar{\sigma}}{\sqrt{2}k_N} ,$$

$$d\Delta u^J = du_z^J - du_x^J = \sqrt{2} du_S^J = \sqrt{2}(du_S^{Je} + du_S^{Jp}) = \frac{d\Delta\sigma}{\sqrt{2}k_S} + \sqrt{2}u_S^{Jp} , \quad (3-23)$$

$$k_N = \frac{A}{(\delta^J - u_N^J)^2} = \frac{1}{A} \left(\frac{A}{\delta^J} + \sigma_N^J \right)^2 .$$

where a superscript *p* denotes the contribution of "plastic" or slipping joint behavior. Similarly, by using equations (3-1), (3-2), (3-4), and (3-22), the intact material response can be written

$$\begin{aligned} d\bar{u}^I &= \frac{du_z^I + du_x^I}{2} = d\bar{u}^{Ie} + d\bar{u}^{Ip} \\ &= w \frac{(1-\nu)d\bar{\sigma} - \nu d\sigma_y}{E} + w\lambda^I [\alpha\bar{\sigma} - \beta(\bar{\sigma} + \sigma_y) - \gamma] , \end{aligned} \quad (3-24)$$

$$d\Delta u^I = du_z^I - du_x^I = d\Delta u^{Ie} + d\Delta u^{Ip} = w \frac{1-\nu}{E} d\Delta\sigma + 3w\lambda^I \Delta\sigma ,$$

$$du_y = du_y^{Ie} + du_y^{Ip} = w \frac{-2\nu d\bar{\sigma} + d\sigma_y}{E} + w\lambda^I [\alpha\sigma_y - 2\beta\bar{\sigma} - \gamma] = 0 .$$

If the intact material is in the elastic regime, equations (3-24) still obtain, but with $\lambda^I = 0$.

In the next four subsections we will combine and solve these equations for each possible mode of deformation as summarized in Table 3-3. Once the four types of solutions are derived, they are used as the basis of a computer program which implements the logic embodied in Table 3-4.

3.5.2.3 Solution for mode 1 (EE) increments. For mode 1 (purely elastic response), equations (3-23) with vanishing joint slip increment ($du_S^{Jp} = 0$) and (3-24) with no intact rock plasticity ($\lambda^I = 0$) combine to give

$$d\bar{\sigma} = \frac{d\bar{u}}{w \frac{1-\nu-2\nu^2}{E} + \frac{1}{\sqrt{2}k_N}} , \quad d\Delta\sigma = \frac{d\Delta u}{w \frac{1+\nu}{E} + \frac{1}{\sqrt{2}k_S}} , \quad (3-25)$$

$$d\sigma_y = 2\nu d\bar{\sigma} , \quad du_S^J = \frac{d\Delta\sigma}{2k_S} .$$

Note that in mode 1 the increment in joint shear displacement du_S^J is explicitly determined by the joint constitutive law through the shear stiffness k_S .

3.5.2.4 Solution for mode 2 (EP) increments. For mode 2 there is still no intact rock plasticity ($\lambda^I = 0$) but now the joint is slipping ($du_S^{Jp} \neq 0$). The joint constitutive law no longer explicitly governs the incremental shear stress-shear displacement across the joint. Instead, the Coulomb friction law relates the shear and normal stress across the joint:

$$f^J = (\tau_S^J)^2 - (\mu\sigma_N^J)^2 = 0 , \quad (3-26)$$

where the coefficient of friction is related to the friction angle by $\mu = \tan \Phi$. The overall response equations analogous to (3-25) follow from (3-23), (3-24), and (3-26):

$$d\bar{\sigma} = \frac{d\bar{u}}{w \frac{1-\nu-2\nu^2}{E} + \frac{1}{\sqrt{2}k_N}} , \quad d\Delta\sigma = \text{sgn}(\Delta\sigma) 2\mu d\bar{\sigma} , \quad (3-27)$$

$$d\sigma_y = 2\nu d\bar{\sigma} , \quad du_S^J = \frac{1}{\sqrt{2}} \left(d\Delta u - w \frac{1+\nu}{E} d\Delta\sigma \right) .$$

3.5.2.5 Solution for mode 3 (PE) increments. In mode 3, the plastic proportionality constant λ^I becomes an additional unknown. The first three equations governing the basic unknown increments are obtained as before by combining (3-23) and (3-24), but now with $\lambda^I \neq 0$. An additional equation comes from the condition of continued yielding (3-6). In matrix form the equations are

$$\begin{bmatrix}
w \frac{1-\nu}{E} + \frac{1}{\sqrt{2}k_N} & 0 & -w \frac{\nu}{E} & w[\alpha\bar{\sigma} - \beta(\bar{\sigma} + \sigma_y) - \gamma] \\
0 & w \frac{1+\nu}{E} + \frac{1}{\sqrt{2}k_S} & 0 & 3w\Delta\sigma \\
-\frac{2}{E} & 0 & \frac{1}{E} & \alpha\sigma_y - 2\beta\bar{\sigma} - \gamma \\
2[\alpha\bar{\sigma} - \beta(\bar{\sigma} + \sigma_y) - \gamma] & \frac{3\Delta\sigma}{2} & \alpha\sigma_y - 2\beta\bar{\sigma} - \gamma & 0
\end{bmatrix}
\begin{bmatrix}
d\bar{\sigma} \\
d\Delta\sigma \\
d\sigma_y \\
\lambda^I
\end{bmatrix}
=
\begin{bmatrix}
d\bar{u} \\
d\Delta u \\
0 \\
0
\end{bmatrix}
\quad (3-28)$$

We have elected to solve this set numerically during each time step when required, rather than explicitly.

3.5.2.6 Solution for mode 4 (PP) increments. In mode 4 both the intact material and the joint are failing. The fundamental unknowns are taken as the three stress increments, λ^I , and the joint slip increment du_s^{JP} . The equations governing the stress increments follow as before from (3-23) and (3-24). The fourth equation is the condition of continued intact material yielding (3-6). The fifth is the differential form of the joint failure condition (3-26), which was already used for mode 2 and appears as the second of equations (3-27). When assembled into matrix form the equations are

$$\begin{bmatrix}
w \frac{1-\nu}{E} + \frac{1}{\sqrt{2}k_N} & 0 & -w \frac{\nu}{E} & w[\alpha\bar{\sigma} - \beta(\bar{\sigma} + \sigma_y) - \gamma] & 0 \\
0 & w \frac{1+\nu}{E} + \frac{1}{\sqrt{2}k_S} & 0 & 3w\Delta\sigma & \sqrt{2} \\
-\frac{2}{E} & 0 & \frac{1}{E} & \alpha\sigma_y - 2\beta\bar{\sigma} - \gamma & 0 \\
2[\alpha\bar{\sigma} - \beta(\bar{\sigma} + \sigma_y) - \gamma] & \frac{3\Delta\sigma}{2} & \alpha\sigma_y - 2\beta\bar{\sigma} - \gamma & 0 & 0 \\
-2\mu \operatorname{sgn}(\Delta\sigma) & 1 & 0 & 0 & 0
\end{bmatrix}
\begin{bmatrix}
d\bar{\sigma} \\
d\Delta\sigma \\
d\sigma_y \\
\lambda^I \\
du_s^{JP}
\end{bmatrix}
=
\begin{bmatrix}
d\bar{u} \\
d\Delta u \\
0 \\
0 \\
0
\end{bmatrix}
\quad (3-29)$$

3.5.3 Analytical and Numerical Results.

In addition to the analytic solution just outlined, complete solutions using explicit joint models were submitted by CRT, WA, and Itasca. A partial solution was completed by LLNL.

RE/SPEC encountered problems with the PRONTO code—to be discussed later—and could not generate a meaningful solution. The lone numerical solution with implicit jointing was by CRT. It gave results which with one exception—to be discussed later—were visually identical with CRT's explicitly jointed solution, so only the latter will be plotted.

The zoning used by CRT, Itasca, and LLNL was the simplest possible choice—single zones for each triangular block and an explicit model of the joint. On the other hand, WA broke the structure into 54 zones with six adjacent to the joint on each side.

Figures 3-14, 3-15, and 3-16 contain the numerically predicted compressibility, stress path, and joint shear displacement vs shear stress along with the analytic solution. The figures show that from this perspective the numerical results that were provided are fairly close to the analytic. Several features of the WA computation of net compressibility in Figure 3-14 deserve mention. It begins with the correct slope but remains linear over most of the duration of compressive loading. The treatment of normal joint stiffness was modified between this problem and the earlier ones such that it was now adjustable, but still restricted to linear behavior. This solution also contains much less residual pressure at the end of the calculation, indicating that for some reason there was not enough dilatancy occurring. Note also that the LLNL result in Figure 3-16 is fairly accurate, indicating that this kinematically-based approach can provide reasonable results for certain portions of some problems.

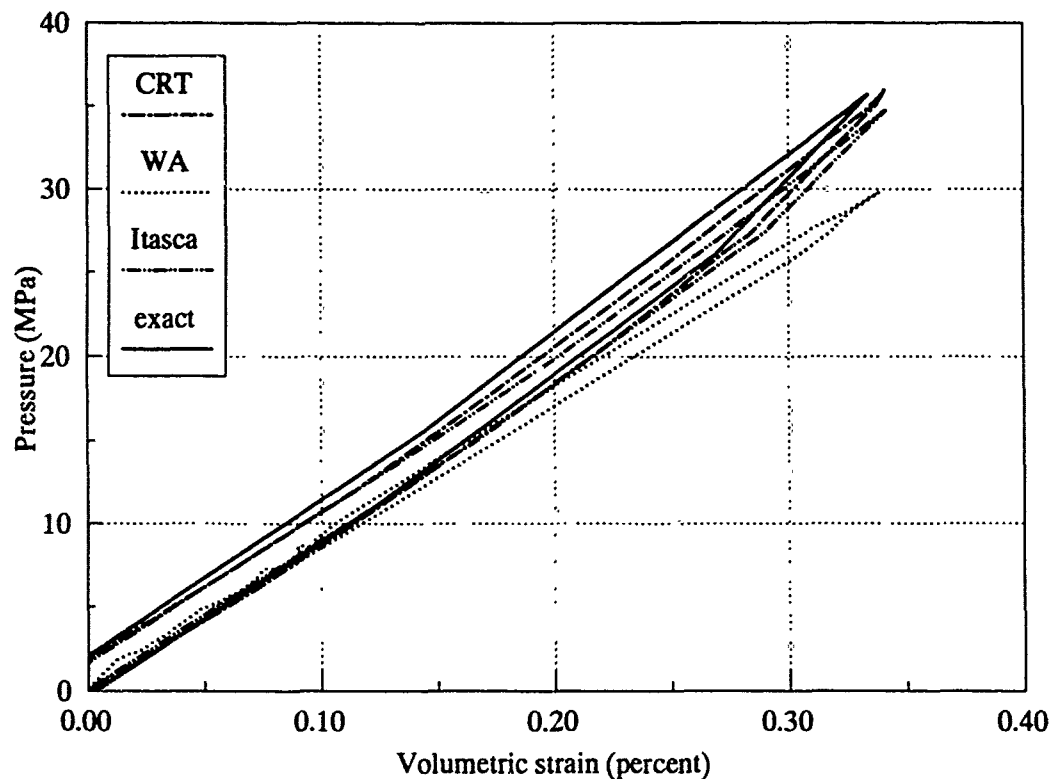


Figure 3-14. Overall compressibility in problem 2-S.

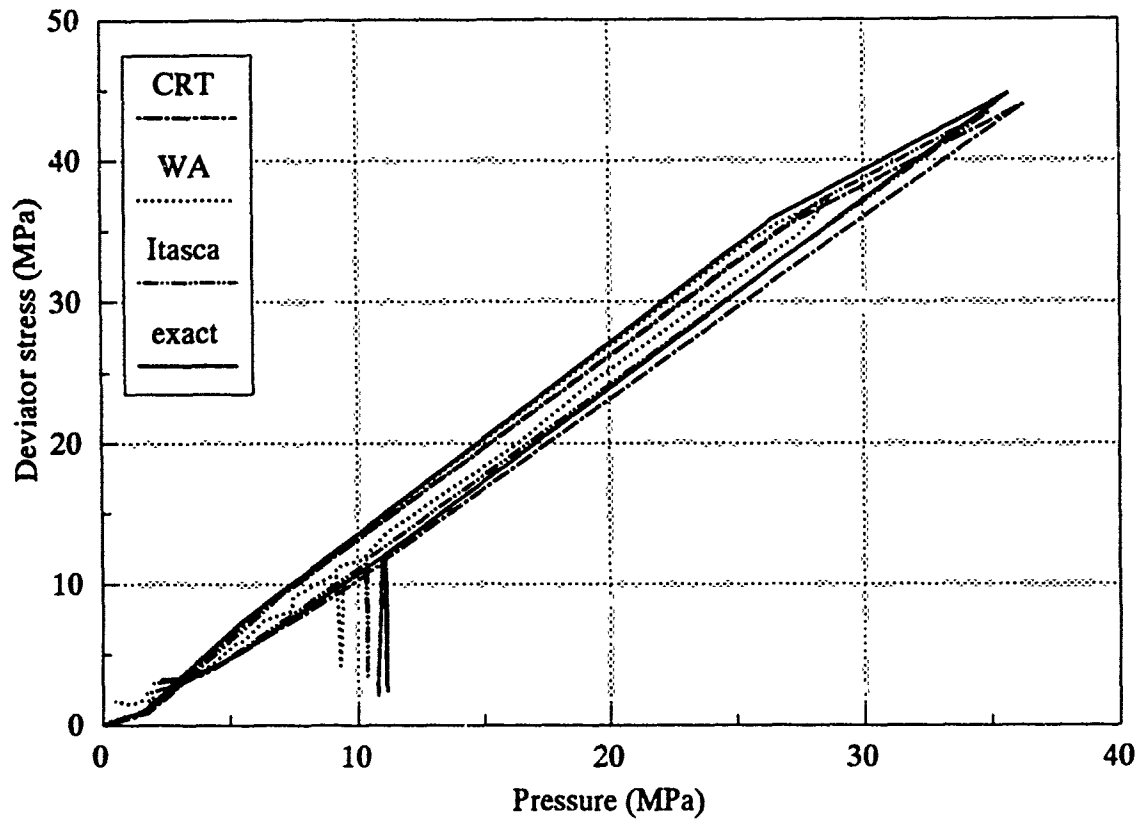


Figure 3-15. Von Mises effective stress path in problem 2-S.

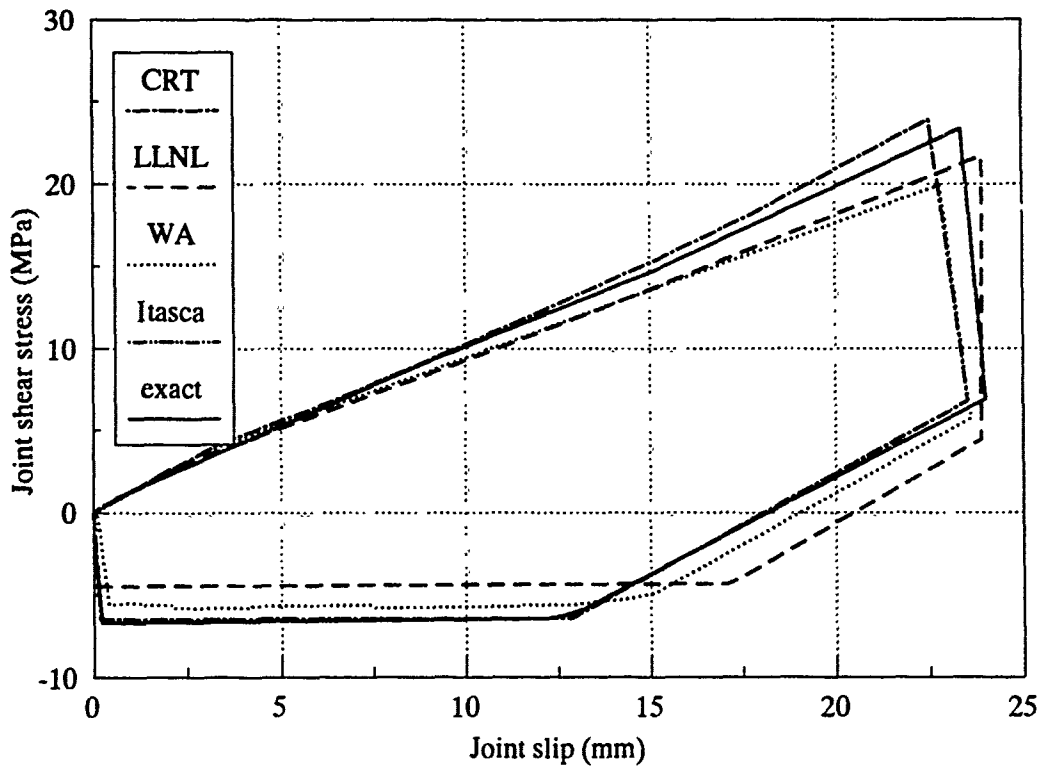


Figure 3-16. Joint shear displacement vs shear stress in problem 2-S.

Figure 3-17 shows the deformation mode vs time for those who provided this information. It is interesting to note that both CRT and Itasca predict a short episode of mode 4 (PP) response starting around $t=1.8$, while the analytic solution does not. This is where the CRT implicit solution differs from explicit. The former stayed in mode 4 for only one time step, thus agreeing most closely with the analytic one. From a practical standpoint, in this particular problem, the discrepancy is of little significance; the stresses and strains in the four solutions are very close to one another. However, this still raises some perplexing questions. On one hand, two conscientious, meticulous calculators independently have reached the same result with their explicitly jointed models; on the other hand, the scheme detailed in Section 3.5.2, for numerically evaluating the analytical solution, has been designed to probe all possible evolutionary paths from each stress point and to test each one for admissibility. At every stage, this scheme has identified a unique admissible stress increment. In particular, in the analytic solution (and effectively in the CRT implicit solution), the stress point approaches the intersection between the two failure surfaces, moves right up to it (by interpolation), and then moves directly *across* it, while the two explicit numerical solutions predict a short traverse *along* the intersection. In the numerical scheme for the analytic solution, an increment along the intersection (mode 4 or PP) was one of the four which were explicitly tested for admissibility (see the last four rows of Table 3-3). It

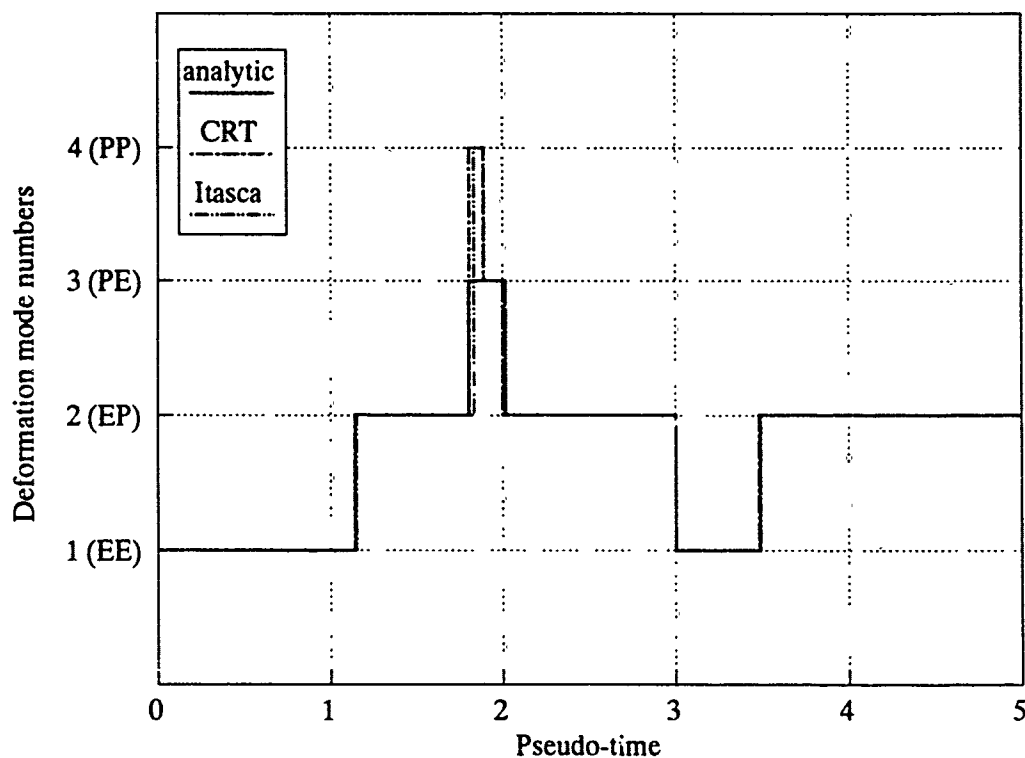


Figure 3-17. History of deformation mode in problem 2-S.

was found to lead to a joint slip increment opposite the prevailing shear stress across the joint, and so was deemed inadmissible. It is also interesting to note that the elastic trial increment from this point gave rise to trial stresses which violated *both* failure conditions (and was ruled out for that reason). This is not the same as the elastic trial used by the numerical solutions⁴. Nevertheless, one might speculate that the numerically derived trial stresses in the explicit models also violated both failure conditions and that this somehow initiated the excursion along the intersection of the failure surfaces. It may then have taken these methods a number of time steps to recognize and correct for joint slippage opposite the shear stress across the joint.

3.5.4 Why PRONTO Was Not Applicable to Problem 2-S.

RE/SPEC elected always to treat the elastic properties of joints implicitly, i.e., by smearing them out and distributing them in the surrounding intact material. Only the Coulomb slip is represented explicitly. This may be reasonable if there are many such joints, but with just a single one it leads to difficulties when the joint is inclined. The problem stems from the fact that the RE/SPEC approach makes the surroundings behave like a transversely isotropic material, with the primary material axis aligned normal to the joint(s). In problem 2-S this axis is 45 degrees from the geometric axes. To see the effect of this misalignment, consider the situation before any slippage occurs. The two triangular blocks are acting as a single, continuous square one. Because of the anisotropy, the specified boundary conditions (constant normal displacements, vanishing shear traction) are not consistent with a homogeneous stress state within the block. In other words, with no shear traction the block would suffer a shear strain and would require linearly varying normal boundary displacements to maintain homogeneity; conversely, a particular value of shear traction could be applied which would cause shear strain to vanish. Therefore, when RE/SPEC set up and ran this problem with the specified boundary conditions, the stress state was nonuniform from the very beginning. Later the situation got even worse, because the joint failure condition was not met simultaneously all along the joint, not even approximately. Because the nonuniformities were traceable to particular features of the RE/SPEC approach in a way that was not anticipated when the problem was defined, it was decided not to pursue the solution to its conclusion with this method.

⁴For this problem, the trial elastic stresses used in the numerical solutions come from strains within each element which depend in part on internal (non-forced) nodal displacements, projected from the previous time step by forward differences based on the momentum balance equations.

SECTION 4

PROBLEM STATEMENTS AND RESULTS FOR TWO-DIMENSIONAL PROBLEMS

4.1 PRELIMINARY DISCUSSION.

The problems treated so far could be classified as both static and "zero-dimensional," since their underlying solutions have neither essential temporal nor large-scale spatial variation. As we have seen, this simplicity makes analytic solutions possible, and those have been used as ground truth for assessing the numerical results. In contrast, problems 3 and 4 have fields which vary both spatially and temporally. Analytic solutions are not generally feasible, and the proper procedure for assessing the accuracy of numerical solutions is much less obvious. In this study, we have tried to use all of the tools available to evaluate the numerical solutions, but none of them is as definitive as a full analytic solution would be. So we check for internal consistency, compatibility with the basic understanding of wave propagation processes, robustness of the method as revealed in the zero-dimensional problems, and comparison with the other solutions. We can perform limited analytical solutions, for example taking numerically computed macroscopic strains as input and deriving intact rock response analytically. In the end we will form some judgments about the relative credibility of the various solutions to these particular problems. But such judgments cannot ever be definitive for problems with no complete analytic solution.⁵

4.2 PROBLEM 3: DIVERGENT WAVE PROPAGATION THROUGH A JOINTED ROCK ISLAND.

4.2.1 Statement of the Problem.

This problem concerns deformations of a wedge-shaped section of an annulus in plane strain, as shown in Figure 4-1. The entire region contains vertically and horizontally jointed rock as specified in Tables 2-1 and 2-2. The top edge (the inner arc) is loaded with the pressure pulse shown in the figure, while shear tractions are zero. (The pulse approximates that at a 500-m range from 1/3 MT of coupled nuclear energy). The left and right sides have roller boundaries, making the left side a plane of symmetry (the right side is not, because the effective anisotropy due to jointing makes the *material* unsymmetric about that plane). The lower edge (the outer arc) is a transmitting boundary. Most of the region is to be modelled implicitly, except for a rectangular region extending 2.5 tunnel diameters (12.5 m) in all directions from the on-axis point at $R=500$ m. This region is to be modelled explicitly, in anticipation of the tunnel situated here in problem 4. The problem is to find stresses, velocities, and strains throughout the region.

⁵Some individuals believe that numerical methods can be "validated" by comparison with experiments. Whether or not this is true is mainly a matter of definition. But in this study, using data is not an option. All the material models are highly idealized and not intended to accurately represent real material behavior.

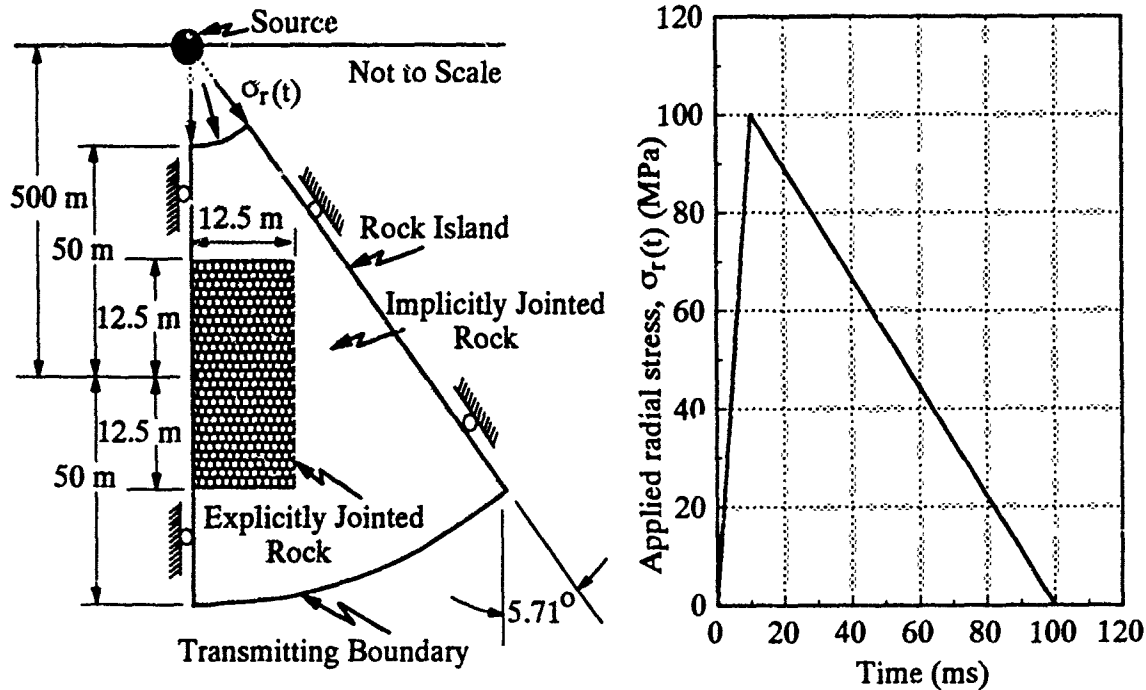


Figure 4-1. Geometry and loading in problem 3.

When this problem was originally set up, a gravitational prestress was proposed. This seemingly innocuous requirement led to both philosophical disagreements and computational difficulties, and was eventually discarded. In principal, given a material model and some assumption about the lateral lithostatic stress, it is straightforward to define the gravitationally induced stresses at any depth in a half-space, then translate those to a set of boundary tractions, body forces, and stresses in the wedge-shaped region of problem 3. Modelers should have been able to impose these loads as initial conditions, then proceed forward with the active loads and boundary conditions applied relative to the initial state.

In practice, most of the modelers were unable to proceed as above without either extensive code modifications or separate off-line calculations. Some could not impose body forces, some could not impose the necessary shear tractions on those boundary segments that were neither vertical nor horizontal, and some could not switch the character of the boundary conditions between the initialization phase and the dynamic loading. A compromise approach was to ignore body forces and boundary shears, and impose only a normal traction on the upper boundary arc as the initial condition. But even if the lower boundary could have been made to switch character (statically a roller, dynamically transmitting), the vanishing shears on the slanted right-hand edge and upper arc would have led to an initial stress state unlike the intended one.

Furthermore, even if a reasonable initial stress state could have been defined, the introduction of a tunnel in problem 4 would have raised a whole new set of issues, differences of opinion, and difficulties. For example, one point of contention would have been whether to impose the prestress after the tunnel is emplaced, or to computationally "excavate" the tunnel in an already prestressed rock mass. In light of all the potential pitfalls, the limited insight into real computational differences that would have been gained compared with the effort that would have been required, and the small anticipated impact on the results even if the loads were imposed correctly, the gravitational prestress was abandoned.

4.2.2 Physical Effects Observed in the Numerical Solutions.

The gross features of the numerical solutions are quite consistent with each other and with expectations. Above all, there is very little variation in the stress and deformation pulses over the computational grid, except for temporal offsets which are fully consistent with anticipated wave propagation speeds. The on-axis vertical stress and velocity at the center of the grid are shown in Figures 4-2 and 4-3. Note the small attenuation in peak stress that has occurred from the top edge, where the applied peak was 100 MPa, to the center, where peaks of 99.1, 94.1,

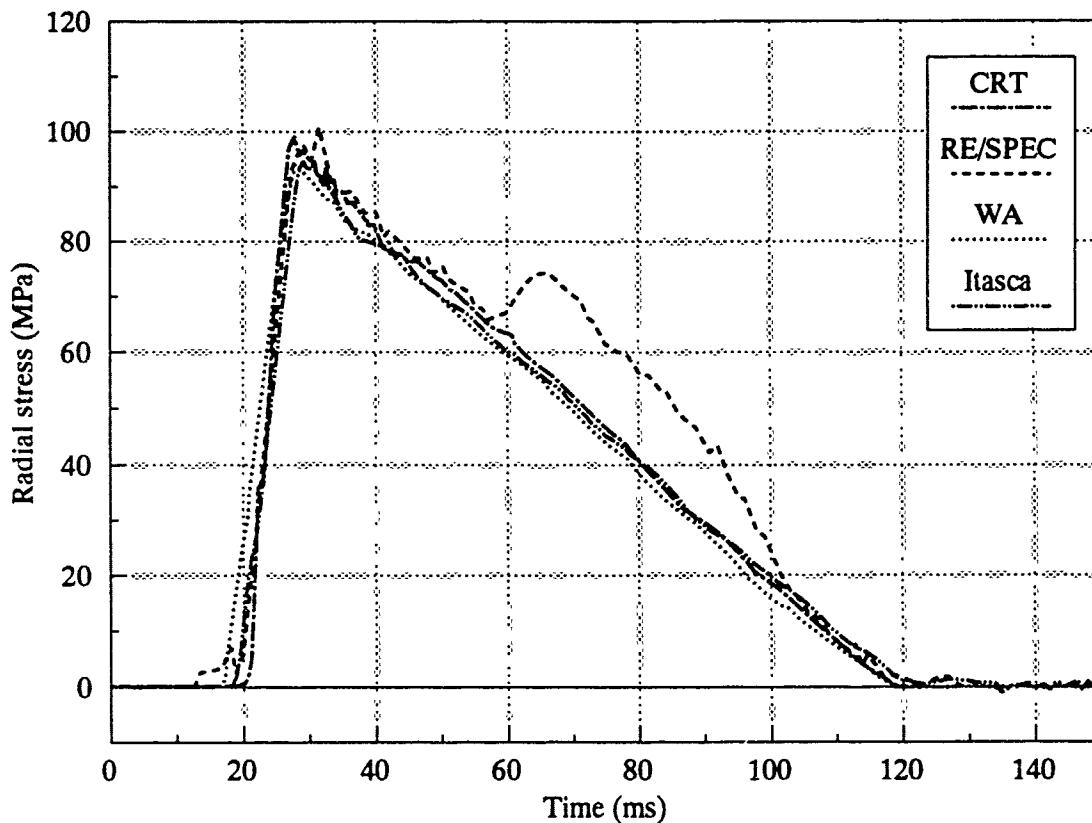


Figure 4-2. Radial stress at tunnel location in problem 3.

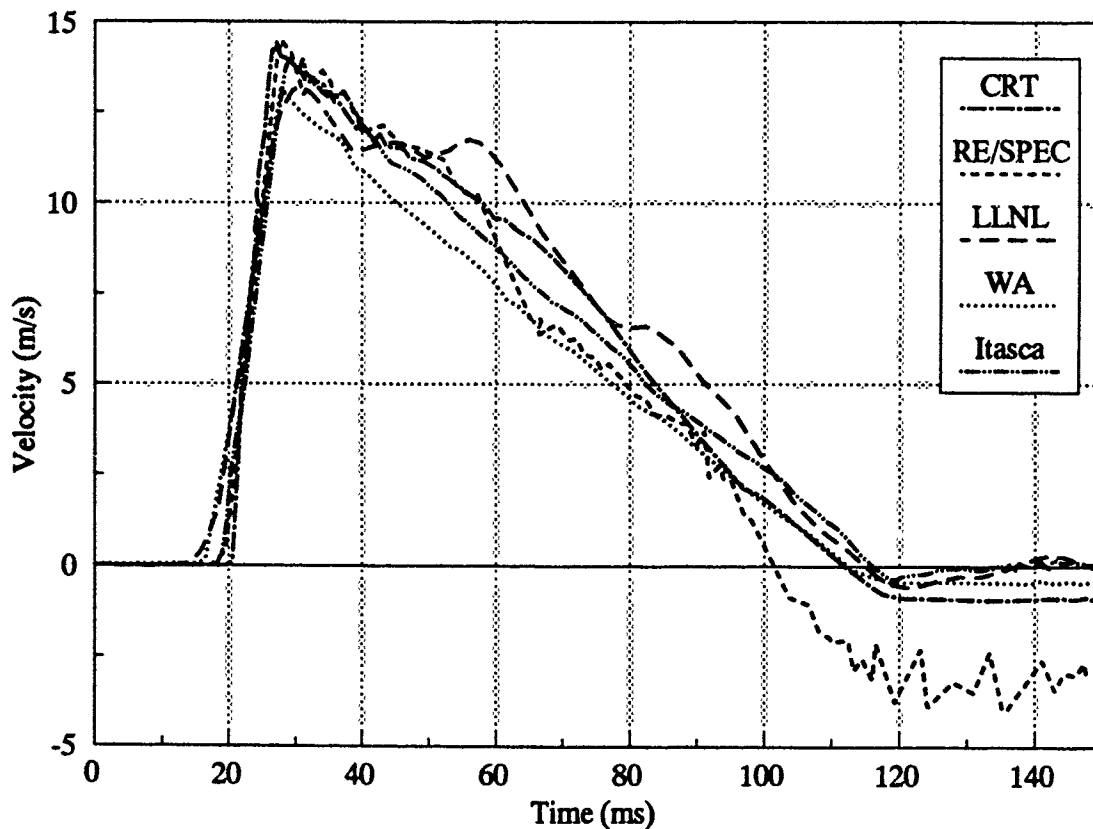


Figure 4-3. Radial velocity at tunnel location in problem 3.

94.7, and 100.8 MPa were reported by CRT, WA, Itasca, and RE/SPEC. Attenuation can be traced either to geometric divergence or material dissipation. The pure geometric divergence of the region over this range is slight: $R^{-1/2}$ is only 5 percent smaller at the center than the top. Furthermore, the effective anisotropy induced by the joints might be focussing energy in the downward direction.

Note that the LLNL approach produced a fairly accurate velocity pulse. This is probably a reflection of the fidelity of the overall uniaxial compressibility as lumped into the joints.

Another indicator of divergence is the post-peak shape of the strain path. Figure 4-4 shows calculated strain paths at $R=500$ m, $\theta=2$, in implicitly jointed rock. They present a macroscopic view of the deformation of a homogeneous effective medium with the properties of intact rock and joints combined and smeared out. In this medium, as in *any* homogeneous medium under rapidly rising but slowly decaying divergent dynamic loading, the strain path is almost purely uniaxial up to the initial peak (i.e., very little hoop strain), but on unloading the hoop strain becomes increasingly negative (tensile) as outward radial displacement accumulates.

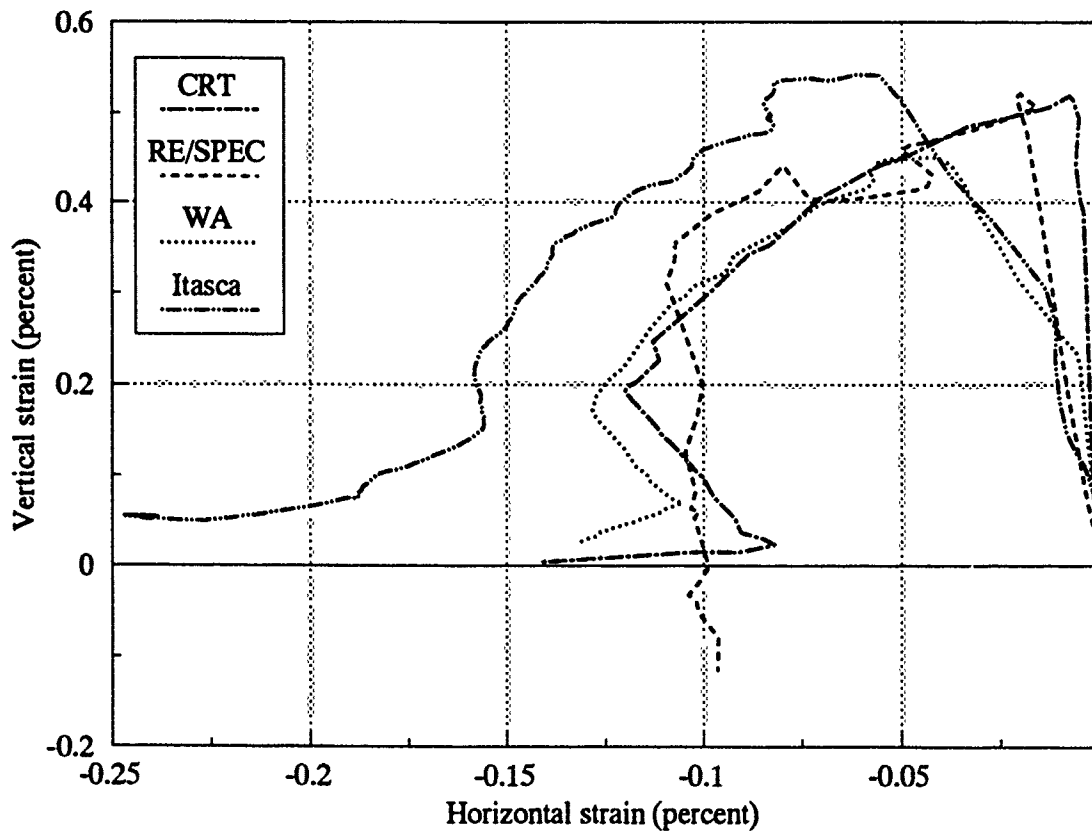


Figure 4-4. Strain path at 500-m range, 2 degrees off axis, in problem 3.

Because the medium is a composite (of joints and intact rock), the foregoing observations do not fully reveal the material's deformation under divergent wave loading. In particular, while the *macroscopic* response is mainly uniaxial strain on loading, the *intact* rock constituent undergoes substantial hoop expansion at the same time. This is illustrated in Figure 4-5, which shows Itasca's calculated on-axis strain paths both above and below the upstream and downstream edges of the explicitly modelled region. In the implicitly jointed material the first leg is uniaxial strain compression; the second, simultaneous hoop and radial expansion, and the third (with some imagination) pure radial expansion. On the other hand, in the intact rock most of the hoop expansion occurs during the first leg along with the radial compression. This effect is exaggerated by the particular constraint conditions of this planar model, and may not be generally representative of three-dimensional divergent wave propagation. Here, through a Poisson effect, the out-of-plane, plane strain constraint makes the intact rock behave more stiffly in the plane. When compressed radially (vertically) it develops compressive hoop (horizontal) stresses which are larger than they would be in the absence of the out-of-plane constraint. The larger compressive stresses are transmitted directly into the vertical joints. Because the constrained intact rock is stiffer than the joints, the joints compress and the intact rock expands horizontally.

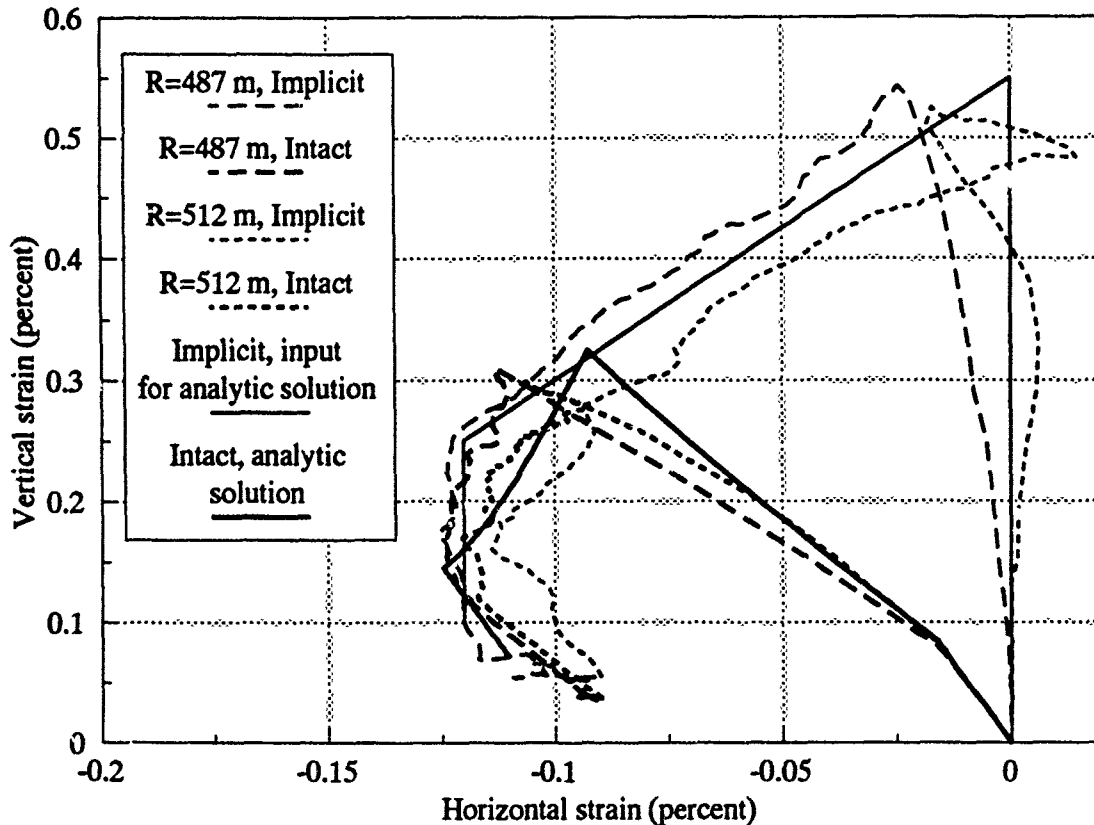


Figure 4-5. On-axis strain paths in implicitly jointed and intact rock, analytic solution and Itasca calculation, problem 3.

Figure 4-5 also shows an analytic representation of this effect. The light solid curve labelled "input for analytic solution" is simply an idealization of the two Itasca strain paths in implicitly jointed rock. This path was used as input into a calculation using the machinery developed for problem 1-IM, i.e., a homogeneous block of implicitly jointed material was homogeneously strained according to the prescribed path. The heavy solid line is the corresponding strain path in intact rock. Note that it agrees well with the numerical results in both magnitude and shape. The kink in the loading leg signals the onset of plastic flow. The fact that the two kinds of paths end up at about the same point is related to the fact that during this deformation the joint behaves elastically, so when the stresses become very small the joints return to near their original dimensions and the residual strains are mostly confined to the intact rock.

Returning to the matter of dissipation, in this problem it could arise either from intact rock plasticity or joint slip. The kinematic constraints and loading virtually preclude joint slip. Plasticity begins part way through the loading phase, which macroscopically is essentially uniaxial strain. On unloading, the small geometric divergence does increase the deviatoric stress

over that which would occur in pure uniaxial strain, and this enhances the plasticity. To illustrate this, Figure 4-6 shows the stress path at a typical on-axis point from all the numerical calculations, compared with the analytic result for uniaxial strain up to about the same peak strain. (The latter comes from the general solution for problem 2.) For both strain paths plasticity begins at a pressure of about 15 MPa and continues up to peak stress. But on unloading, the deviator stress $(3J_2)^{1/2}$ is much greater at the same pressure in the divergent problem than the uniaxial one. The divergence, though small, is sufficient to cause the unloading to be predominantly plastic, following along the failure surface, while by comparison it remains elastic in the uniaxial case.

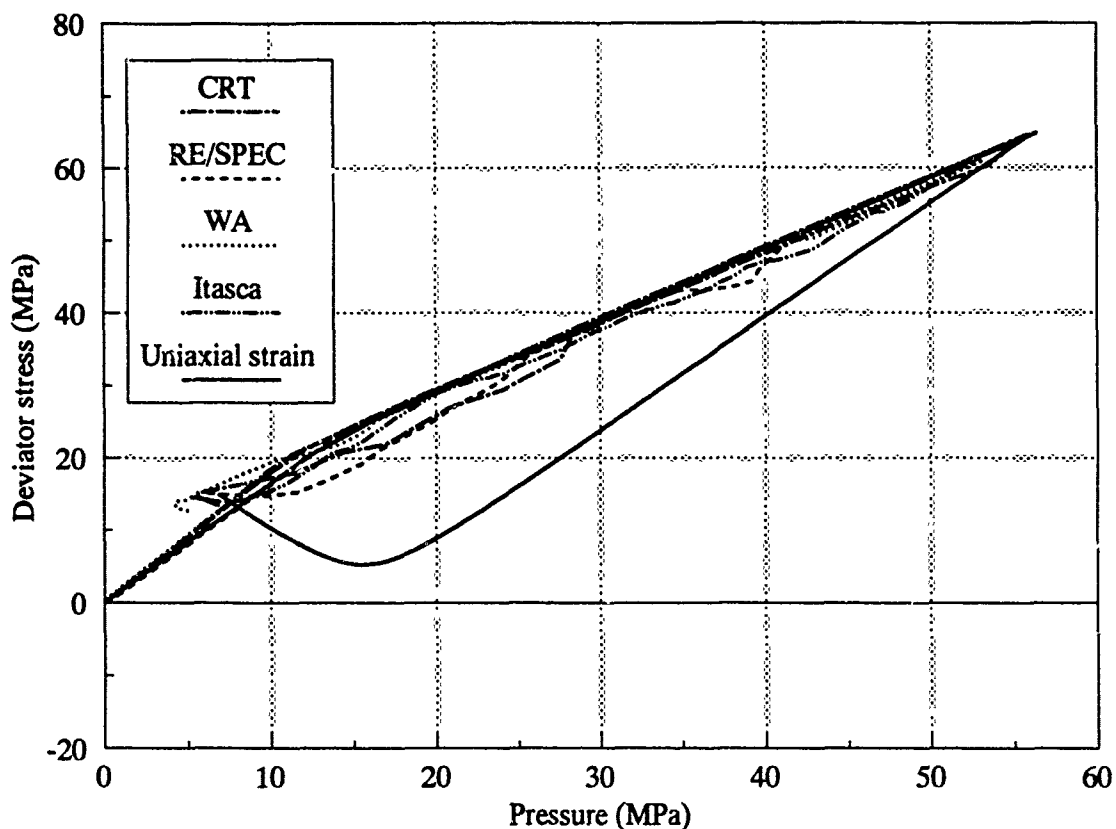


Figure 4-6. Stress path at 487-m range on axis in implicitly jointed rock in problem 3.

With all this plasticity, why then isn't there more attenuation due to dissipation? The main reason is dilatancy, which tends to offset the deviatoric dissipative losses with volumetric expansion against a positive pressure. This is illustrated in Figure 4-7, which gives the pressure-volume paths computed in adjoining zones in the implicitly and explicitly jointed rock. Dilatancy causes a larger final volume than initial, corresponding to *negative* volumetric dissipation (the area between the loading and unloading curves). Net volumetric work is being done *by* the material. The difference between the two sets of curves in Figure 4-7 is that the one in the explicitly jointed region represents local volumetric strain in the intact rock only, while the other

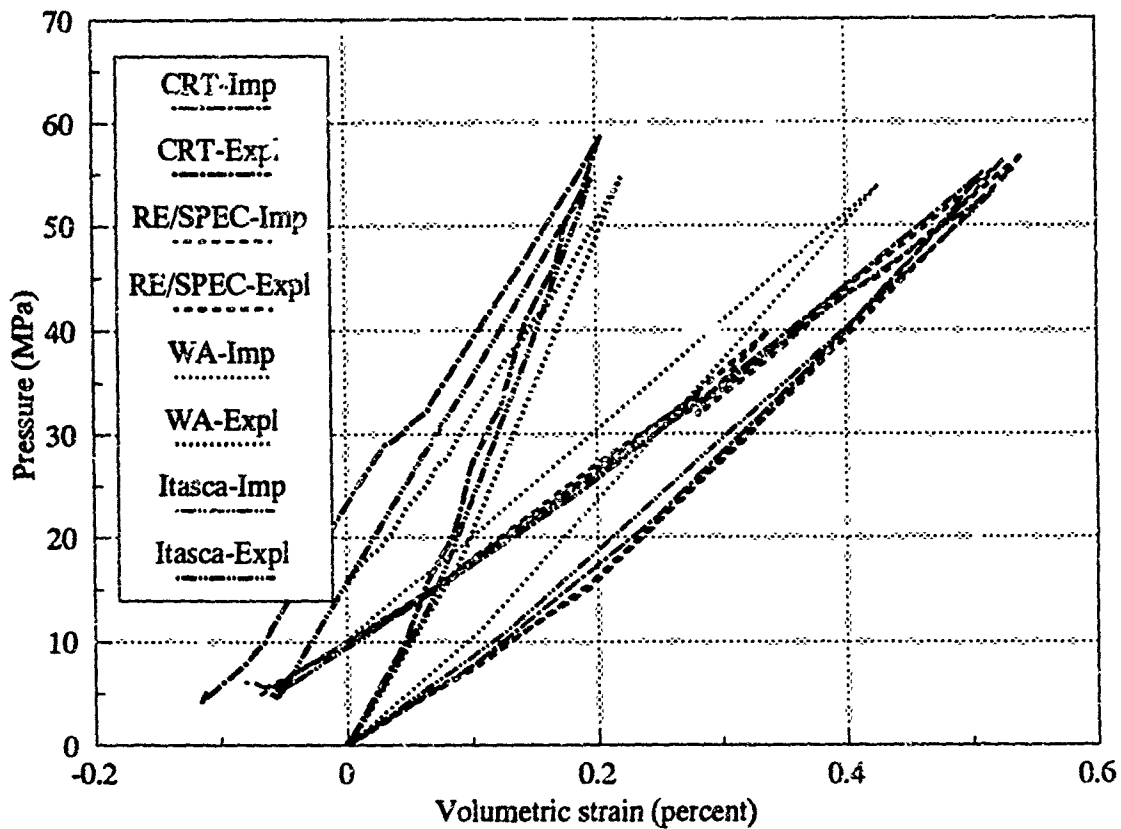


Figure 4-7. Compressibility at 487-m range on axis in problem 3.

set shows overall volumetric strain including the portion due to the joints. (There is only one value of pressure; it is the same in intact rock as in implicitly jointed rock.) The volumetric strain due to the joints is entirely elastic, positive, and recoverable (compressive), while the intact material contributes a positive elastic portion and—after the onset of plasticity at about 15 MPa pressure—a negative (expansive) plastic dilatant portion. Under the constraint conditions here, at low pressure the elastic volumetric strain in intact rock is about one third of the total elastic strain. This fraction increases as the joints stiffen with pressure (in the limit of very large pressure the joints would become rigid and *all* the elastic strain would be in the intact rock). The dilatancy accumulates continuously during both the post-yield portion of the loading phase and the plastic portions of the unloading. Referring to Figure 4-7, during loading the dilatant volume strain is the horizontal distance between the actual curve and the extrapolation of the initial (elastic) part to higher pressures. During unloading, the additional dilatant volume strain is the horizontal distance between the unloading and loading curves. At the same pressure, these horizontal distances should be the same in the implicit curve as the intact one, since there is no plasticity in the joints. Consequently, the areas representing work done by the material will be the same regardless of which type of pressure-volume curve is used.

4.2.3 Numerical Issues.

This problem was specified to have a nonreflecting boundary at the lower edge of the grid. It is well known that no all-purpose absorbing boundary is possible. However, in this problem practically all of the motion is normal to the boundary and the material is almost elastic, so in principle it is possible to meet the specified condition very accurately. One obvious way to evaluate the absorbing boundaries is to examine stress pulses at various locations for reflected signals. Figure 4-8 shows radial stress pulses at three ranges for each calculator who submitted the data. The data from RE/SPEC show clear evidence of a fairly strong reflection, and a little analysis of the timings shows that it has to come from the bottom edge of the grid. The explanation is that the PRONTO formulation requires compressional and shear wave speeds, and computes them without accounting for the anisotropy introduced into the implicitly modelled surroundings by RE/SPEC's "compliant joint" model. Thus with incorrect wave speeds a spurious reflection is generated. RE/SPEC did not directly remedy this error during the course of this study, although this problem was rerun with an extended grid such that no bottom boundary reflection reached the region of interest during the time of interest.

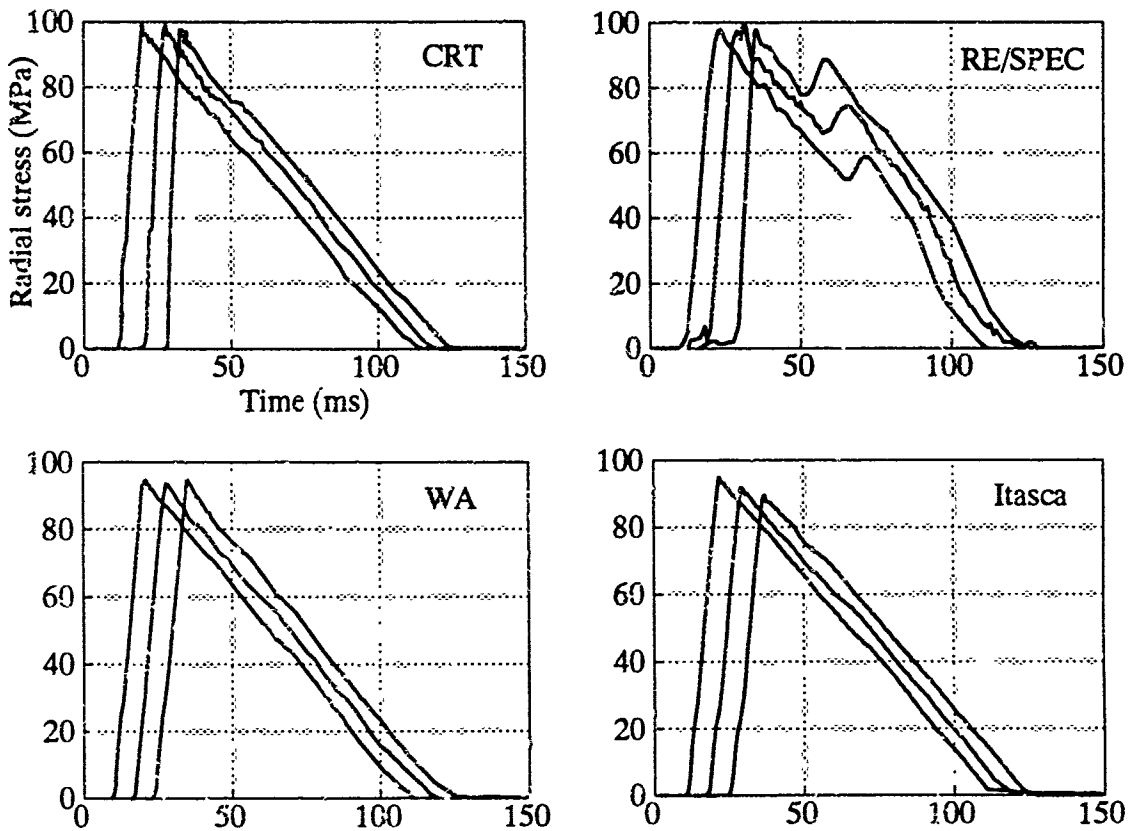


Figure 4-8. Radial stress pulse shapes at 480, 500, and 520-m ranges in problem 3.

A related issue concerns the continuity between the implicitly and explicitly modelled regions. In principle the boundaries should be invisible to waves which are long compared to joint spacing. In this problem the rise time is 10 ms and the loading wave speed is about 2.5 m/ms, so the stress rise—the shortest feature of the wave—is spread out over about 25 m. Since the joints are only 1 m apart one would not expect to see much effect of the implicit/explicit boundary. In Figure 4-8 there is no obvious sign of reflections from these boundaries. Another diagnostic of possible material discontinuity is the difference in computed horizontal stress pulses on either side of the boundary; they should be equal. These traces at the downstream, on-axis discontinuity are shown in Figure 4-9. None of the calculations gives a perfect match, but CRT and RE/SPEC are quite close, while WA and Itasca differ by 20 percent or more over most of the pulse. The discrepancy may be related to the fact that both WA's and Itasca's implicit models are *isotropic* (Appendices D and E), while as noted above the overall behavior of the jointed rock mass is *orthotropic*. Note, however, that by adjusting Poisson's ratio even an isotropic material could be made to give nearly the correct coupling between horizontal and vertical stresses and strains, and therefore to provide the same horizontal stresses in the implicitly and explicitly jointed regions when the wave traverses that boundary. Apparently WA and Itasca used some other criterion for selecting the material properties in the implicitly jointed region. The orthotropic elastic idealization is discussed further in Section 4.3.3.

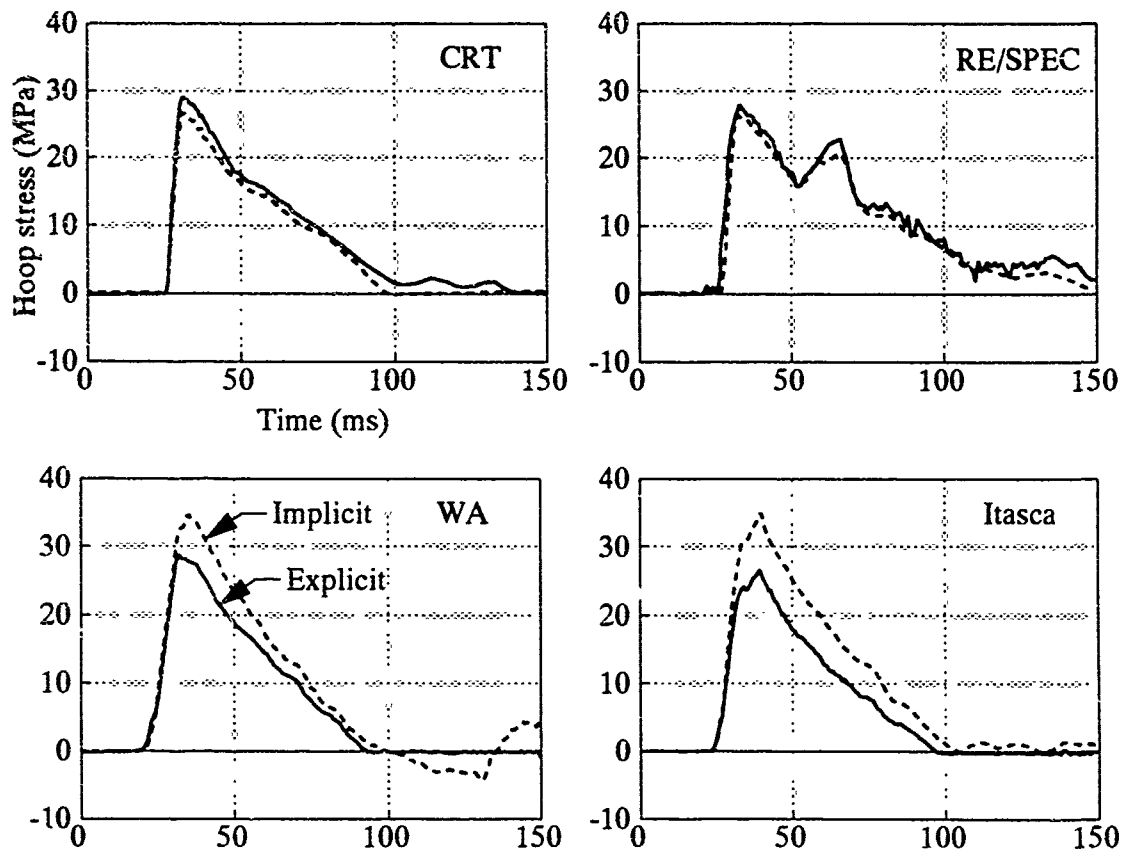


Figure 4-9. Hoop stress at 512-m range on axis, implicit and explicit region, problem 3.

4.3 PROBLEM 4: LINED TUNNEL IN A JOINTED ROCK ISLAND SUBJECTED TO DIVERGENT WAVE PROPAGATION

4.3.1 Statement of the Problem.

The geometry and loading in this problem are shown in Figure 4-10. They are precisely the same as problem 3, but now there is a lined tunnel in the center of the rock island. The properties of the liner have been listed in Tables 2-1 and 2-2. Calculators were asked to provide many diagnostics of tunnel and surrounding medium response, some of which will be discussed here.

The LLNL methodology has no intrinsic mechanism for representing Poisson effects, i.e., horizontal stresses caused by vertical strains. Therefore, in some cases, two different solutions are presented, one with no horizontal stress, and a second with an externally imposed, constant, horizontal stress of 33 MPa. Unless otherwise noted, the LLNL results are for the nonvanishing horizontal stress.

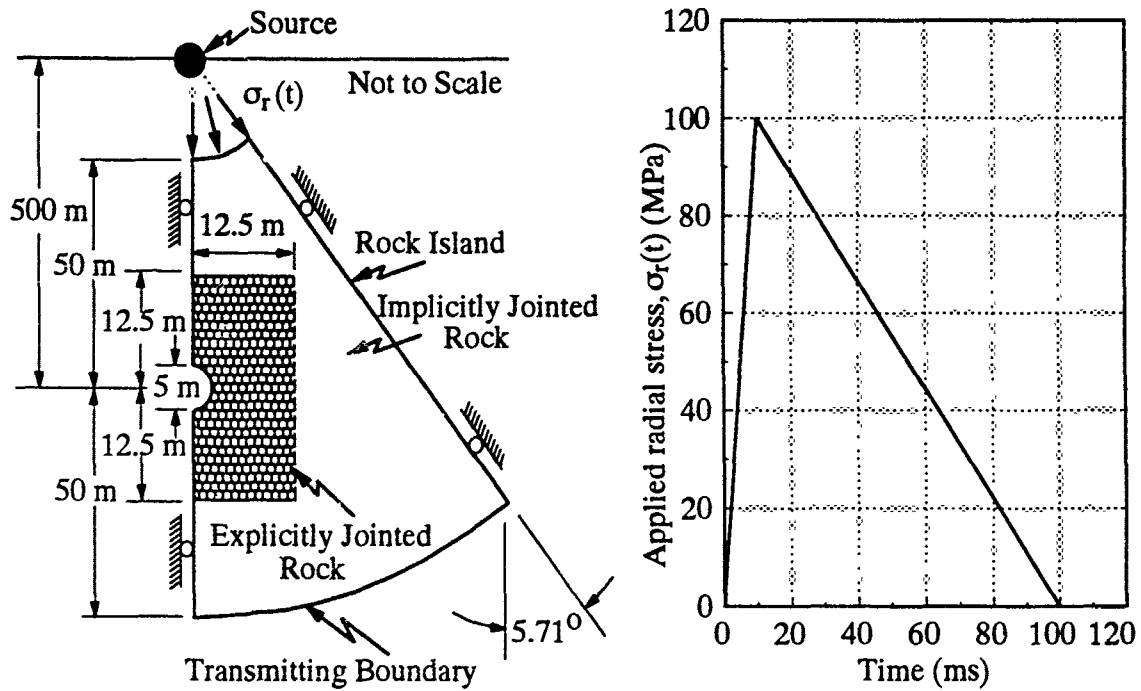


Figure 4-10. Geometry and loading in problem 4.

4.3.2 Physical Effects Observed in the Numerical Solutions.

To begin this discussion, some general observations will be made. The incident pulse was analyzed in problem 3 and is shown in Figures 4-2, 4-3, and 4-8. It propagates at about 2.5 m/ms with little change in shape. Thus the leading edge of the pulse arrives at the tunnel location about 20 ms after application to the rock island boundary, and the peak, about 10 ms later.

It has been noted both in experiments and calculations that tunnel deformations are generally more severe under divergent wave loading than uniaxial loading to the same peak stress. Conventional wisdom holds that in divergent flow the post-peak radially outward motions cause rapid circumferential unloading, "loss of confinement," and consequent reduced strength around the tunnel, compared with unidirectional flow. We have already seen in problem 3 that the macroscopic free field strain path in this geometry does include post peak hoop expansion (Figures 4-4, 4-5), and that the stress path remains either on the failure surface on unloading or much closer to it than in uniaxial strain (Figure 4-6). However, according to Figures 4-11 and 4-12, which show histories of calculated crown/invert and springline closures, all participants

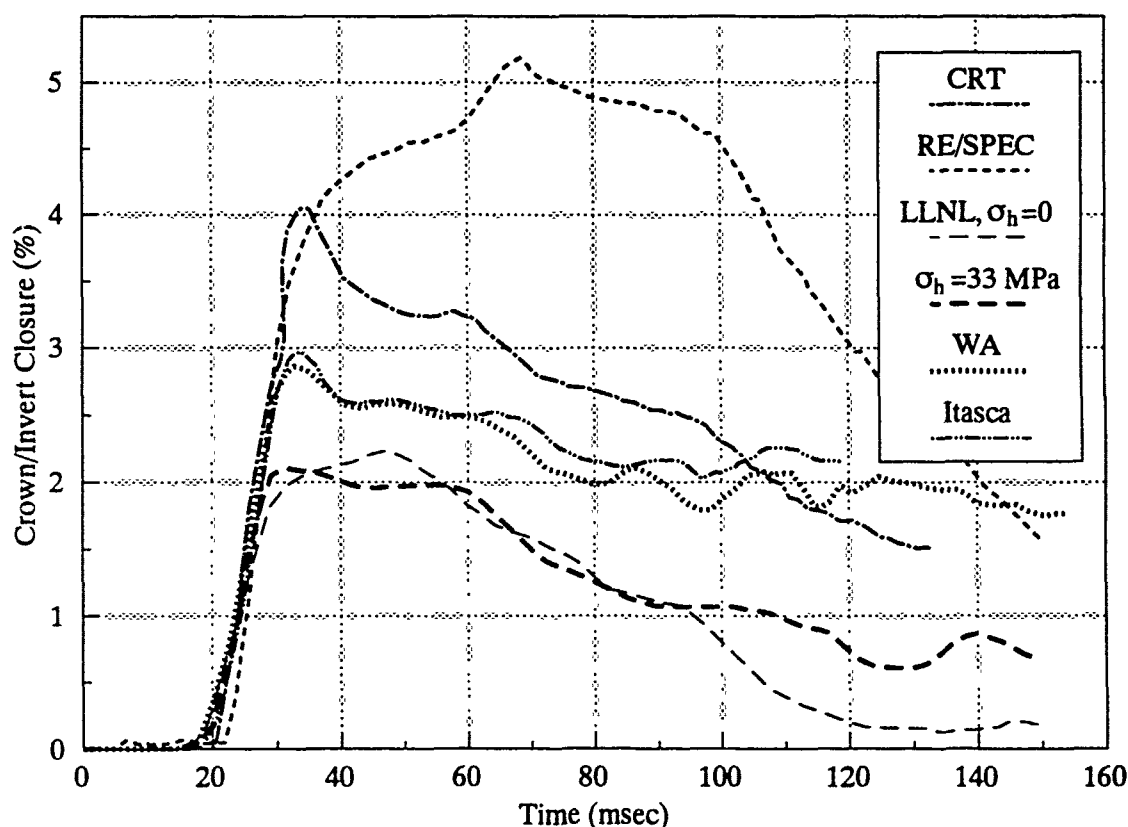


Figure 4-11. Crown-invert closure in problem 4.

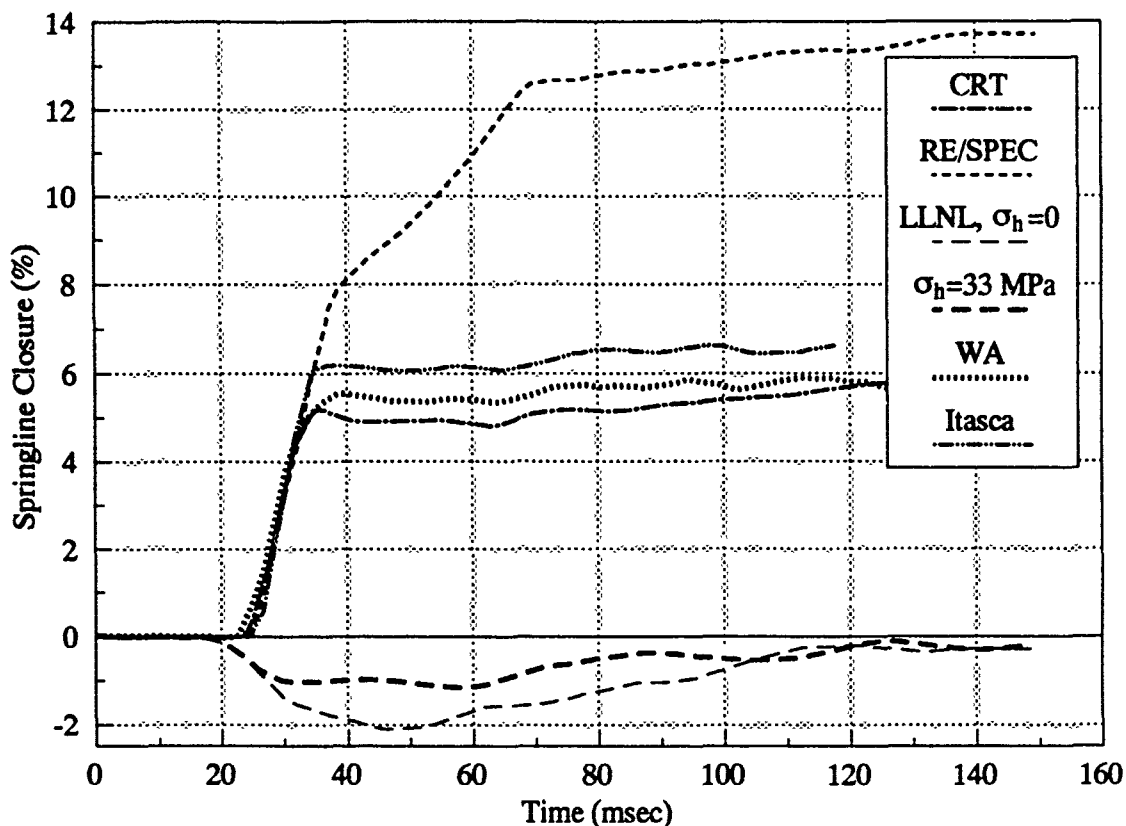


Figure 4-12. Springline closure in problem 4.

except RE/SPEC predict that before 35 ms have elapsed, the tunnel deformation has essentially reached its transient maximum. At this time, only about 20 percent of the ultimate outward displacement and hoop strain has accumulated, and the free field stress at the tunnel range has only dropped by about 5 percent from its peak. Moreover, results from problem 3 indicate that after the peak, the stress point is often slightly below the failure surface (Figure 4-6), not precisely on it as the "loss-of-confinement" scenario would seem to imply. Thus, while some aspects of the calculated results appear to conform with conventional wisdom, other details suggest that the situation is more complex.

One crucial feature which bears on the relationship between the free field and the tunnel deformation is the stress and strain concentration caused by the presence of the tunnel itself. For example, if the surroundings were infinite, isotropic, and elastic and the free field stress state static and unidirectional, then it is well known that the tangential stress at the springline of a circular tunnel is three times the free field stress. While plasticity and joint failure place limits on the achievable stress concentration in this problem, it is clear that the free field stress state need not be precisely on the failure surface in order for the material near the tunnel to be in a plastic state.

Figures 4-13 to 4-16 contain a more detailed picture of the predicted stresses around the tunnel. They show the radial and tangential (with respect to the tunnel) stress distributions near the tunnel at two different times, free field peak stress arrival (about 30 ms) and end of positive phase (about 120 ms). Four of the calculators (CRT, RE/SPEC, and Itasca) provided results in this form. The curves labelled "elastic" in the first two figures will be discussed later.

First consider the radial stresses (with respect to tunnel centerline) at peak stress arrival (Figure 4-13). According to the results of problem 3 the free field vertical stress at the tunnel range is about 100 MPa and the horizontal stress about 30 MPa. At this time the free field stresses will decrease with either increasing or decreasing range from the source point, by about 40 or 5 percent respectively over the 12.5 m (2.5 diameters) plotted. While the calculated radial stresses 12.5 m above the tunnel do exceed those an equal distance below (as expected), neither level is as high as the corresponding free field value. This indicates that the relief provided by the tunnel wall has an effect at least this far out in the vertical direction. Along a horizontal radial, however, the calculated radial stresses approach the free field horizontal stress of 30 MPa much more quickly.

Note in Figure 4-13 that radial stresses along all radials approach about 8 MPa at the tunnel wall. This is the pressure exerted by the yielding perfectly plastic liner in the "breathing" mode.

Figure 4-14 clearly shows the concentration of tangential stress along the horizontal radial. Peak reported values range between 120 and 160 MPa, compared to the free field stress in the same direction of about 100 MPa. However, these peaks are not as high as an isotropic elastic analysis would predict. The reason, as noted above, is that the plasticity limits the level of achievable stress concentration, particularly in the presence of the relief afforded by the tunnel wall.

The "sawtooth" variation of horizontal stress along the vertical radials in Figure 4-14 is due to target point locations alternating between intact rock and joints. There is no requirement that horizontal stresses in horizontal joints be continuous with those in adjoining intact rock. It is comforting to note that most calculations approximately agree on the shapes and magnitudes of these curves.

Thus many features of the stress states at 30 ms can easily be explained based on intuitive, static analysis, and more will be explained later based on an orthotropic elastic analysis. In contrast, the picture at the end of the positive phase (Figures 4-15 and 4-16) is not nearly as clear. The only stresses present are either dynamic or residual, and the levels are much lower on the average. One reason for RE/SPEC's larger values compared with the others is that they plotted results at the end of their free-field positive *velocity* phase, which came earlier than the others (see Figure 4-3), while the free-field stress was still moderately compressive (see Figure 4-2).

Figures 4-17 and 4-18 show the slip along the first four horizontal joints above the tunnel centerline at two times, peak free-field stress arrival and end of positive phase. (All calculators

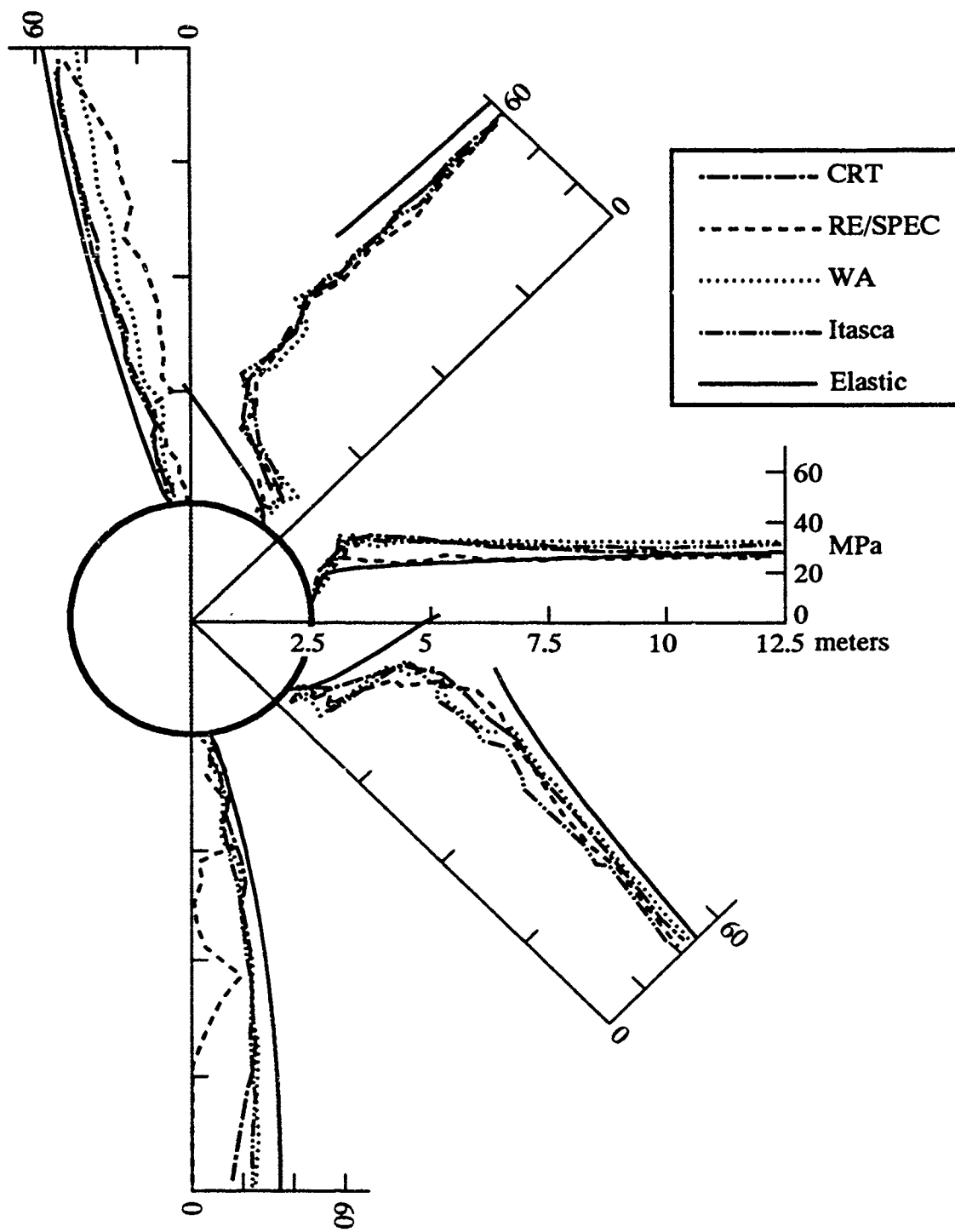


Figure 4-13. Radial stress field near the tunnel at peak free field stress arrival time (about 30 ms).

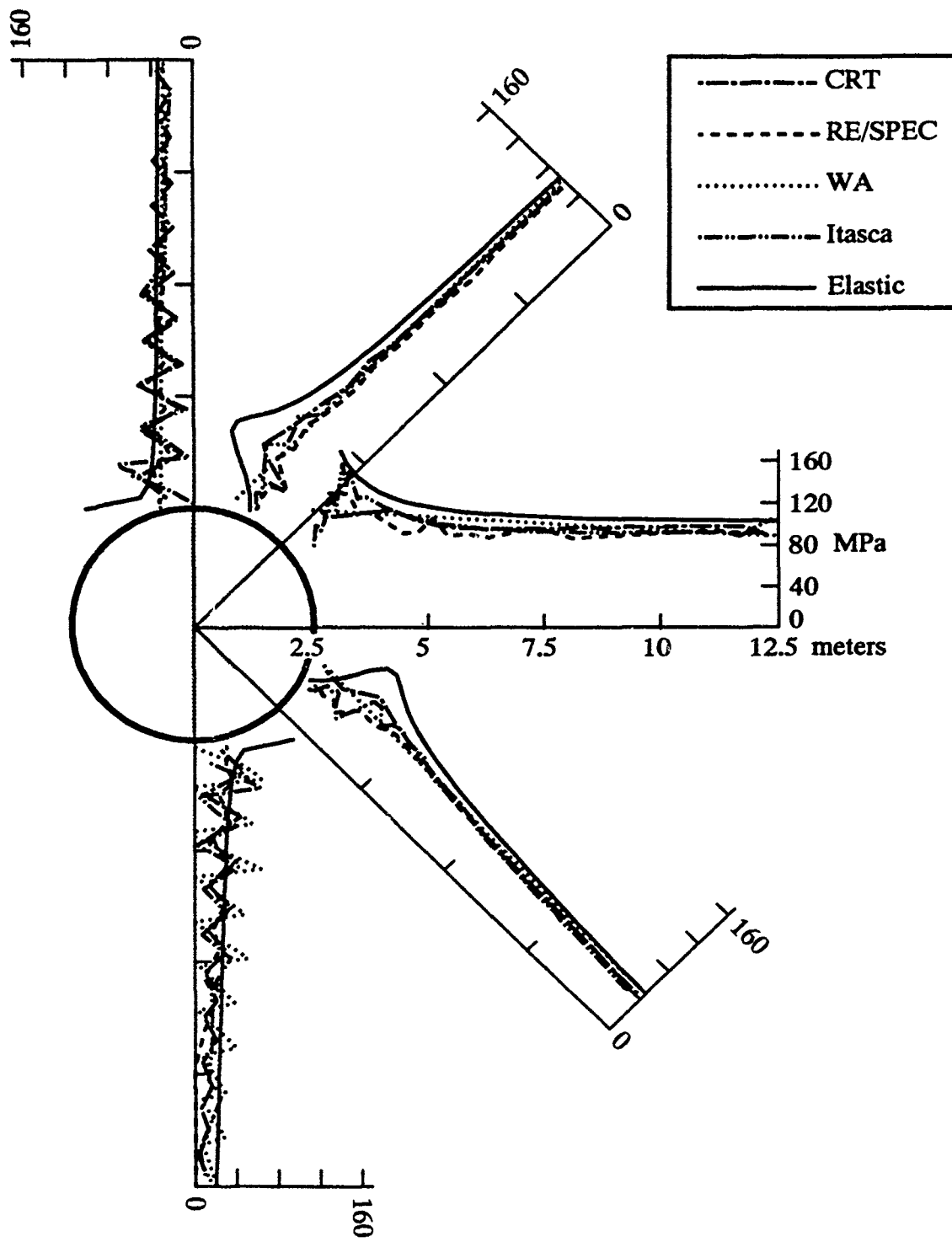


Figure 4-14. Tangential stress field near the tunnel at peak free field stress arrival time (about 30 ms).

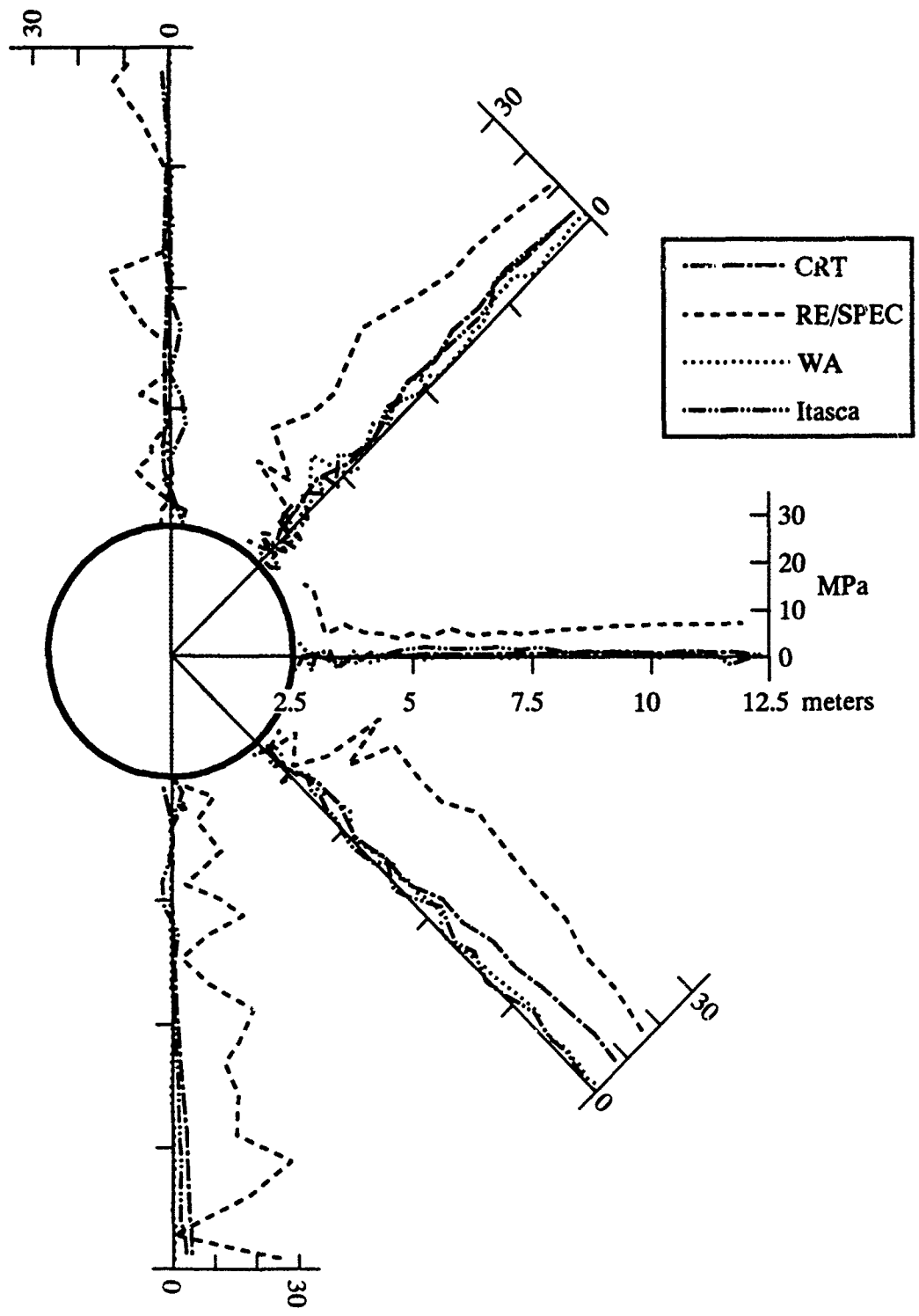


Figure 4-15. Radial stress field near the tunnel at the end of the free-field positive phase (about 120 ms).

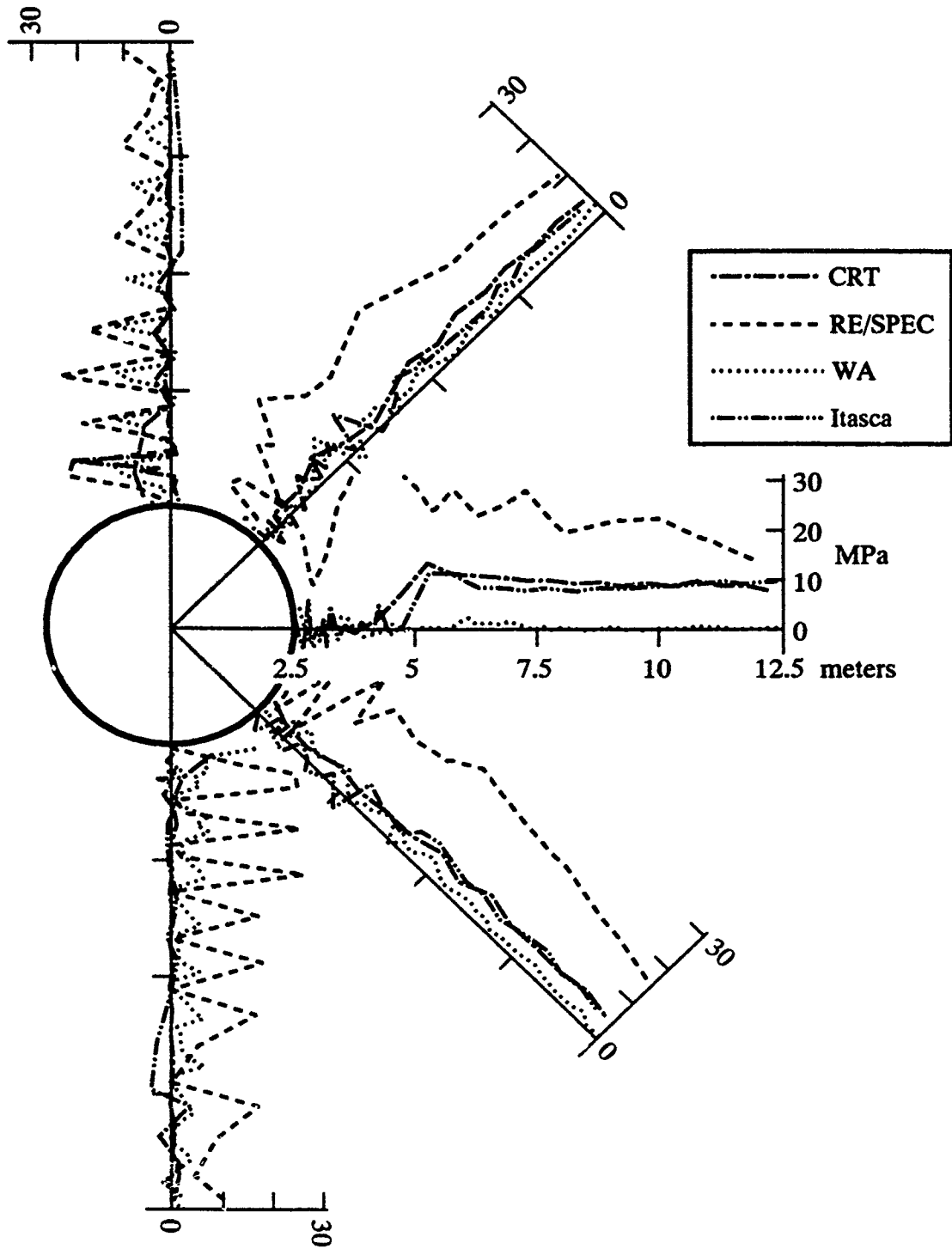


Figure 4-16. Tangential stress field near the tunnel at the end of the free-field positive phase (about 120 ms).

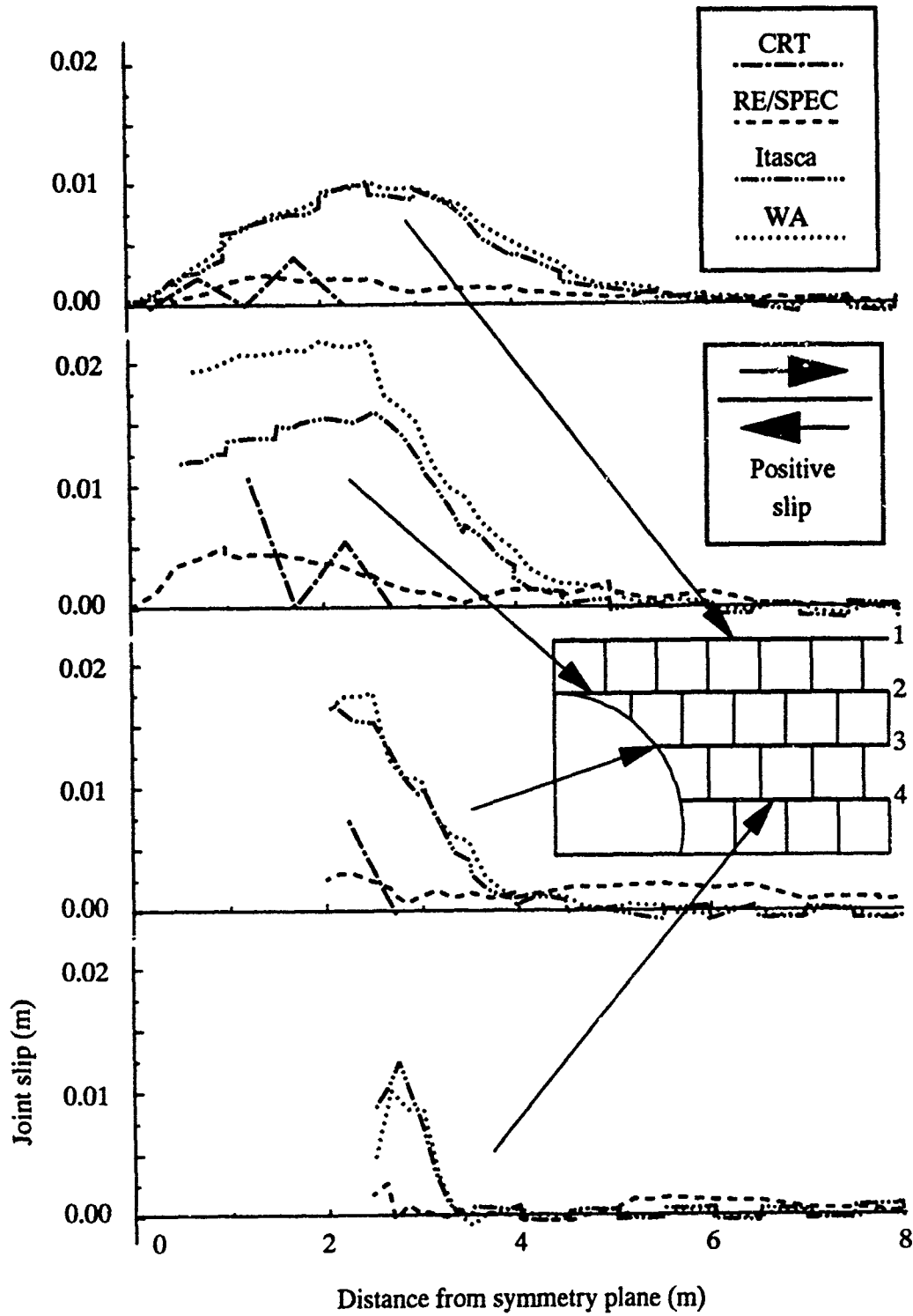


Figure 4-17. Slip along horizontal joints at peak free-field stress arrival.

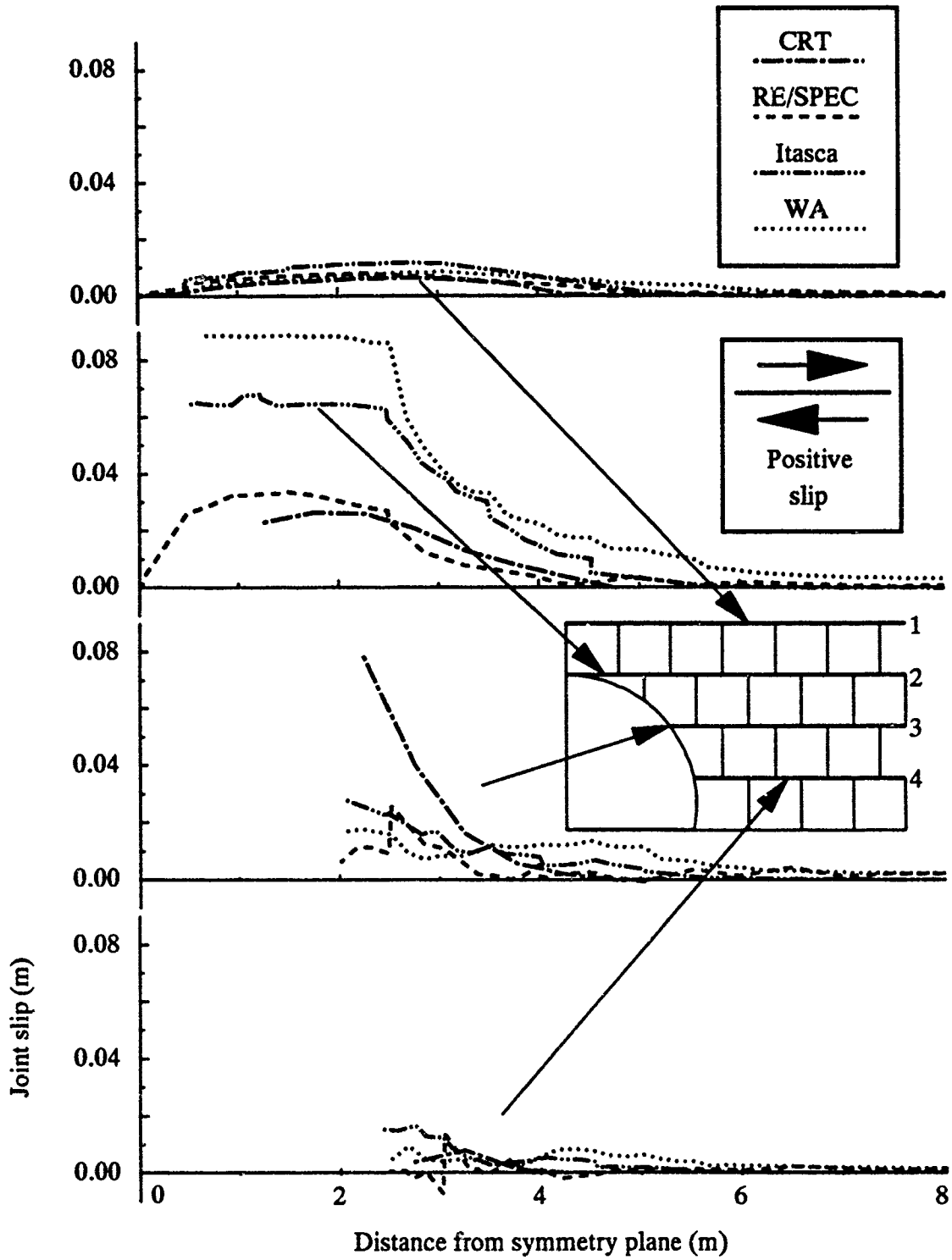


Figure 4-18. Slip along horizontal joints at the end of the free-field positive phase.

predicted nearly equal and opposite slip on the corresponding joint *below* the centerline at the same time.) Virtually all the slips are in the sense that would shorten the springline. The greatest amount of slip occurs along the joint tangent to the top of the tunnel (joint 2) and the one below that (joint 3). The slip at the later time exceeds that at the earlier one by an average factor of about four. At the earlier time, CRT appears to have some non-slipping nodes surrounded by slipping ones, which runs contrary to intuition. Itasca and WA predict slips that average 2 to 3 times the others, but CRT predicts a large slip on joint 3 at the end of the positive phase at the tunnel wall. Overall there is very little consistency in these results among the calculators, making them very difficult to interpret.

One question that could be asked is "How much springline closure can be traced directly to joint slip?" Table 4-1 addresses this question. The table simply sums the slips estimated at the tunnel wall at the end of the positive phase for the two joints nearest the centerline (joints 3 and 4). These two joints could be said to contribute directly to springline closure since they are the ones that intersect the upper half of the tunnel boundary. Again there is little consistency. CRT and Itasca's joints contribute to order unity, while RE/SPEC's barely contribute at all. However, this ranking is not representative of the average slips, where CRT and RE/SPEC are about equal, but—contrary to intuition—RE/SPEC's predictions appear to go to zero at the tunnel wall.

Table 4-1. Joint slip contribution to springline closure.

	CRT	RE/SPEC	Itasca	WA
Joint 3 slip at tunnel edge (m)	0.0904	0.0060	0.0278	0.0169
Joint 4 slip at tunnel edge (m)	0.0023	0.0004	0.0152	0.0047
Sum of joint 3 and 4 slips (m)	0.0927	0.0064	0.0430	0.0216
Half of springline closure (m)	0.138	0.325	0.165	0.145
Fraction of closure due to slip	0.67	0.02	0.26	0.15

Numerically predicted final deformed tunnel shapes are shown in Figure 4-19 (Displacements have been exaggerated by a factor of 10). According to this figure and Figures 4-11 and 12, all calculations except LLNL's show *reverse owalling*, i.e., the springline closure is positive. Most calculations predict severe, localized deformation of the block of rock bordering the springline. This appears to be due to a combination of three factors: (1) Highly concentrated vertical stresses at the springline combine with (2) low lateral confinement due to the presence of the tunnel wall (and not necessarily to wavefront divergence) to create a failed, vertically compressed stress state. (3) Dilatancy then inhibits net compaction, exaggerating the amount of "extrusion" of intact rock into the tunnel. Note that since the LLNL model did not represent the rock as a deformable continuum, it could not have accurately represented the effect of dilatancy, nor could it have correctly predicted the stress concentration near the tunnel wall.

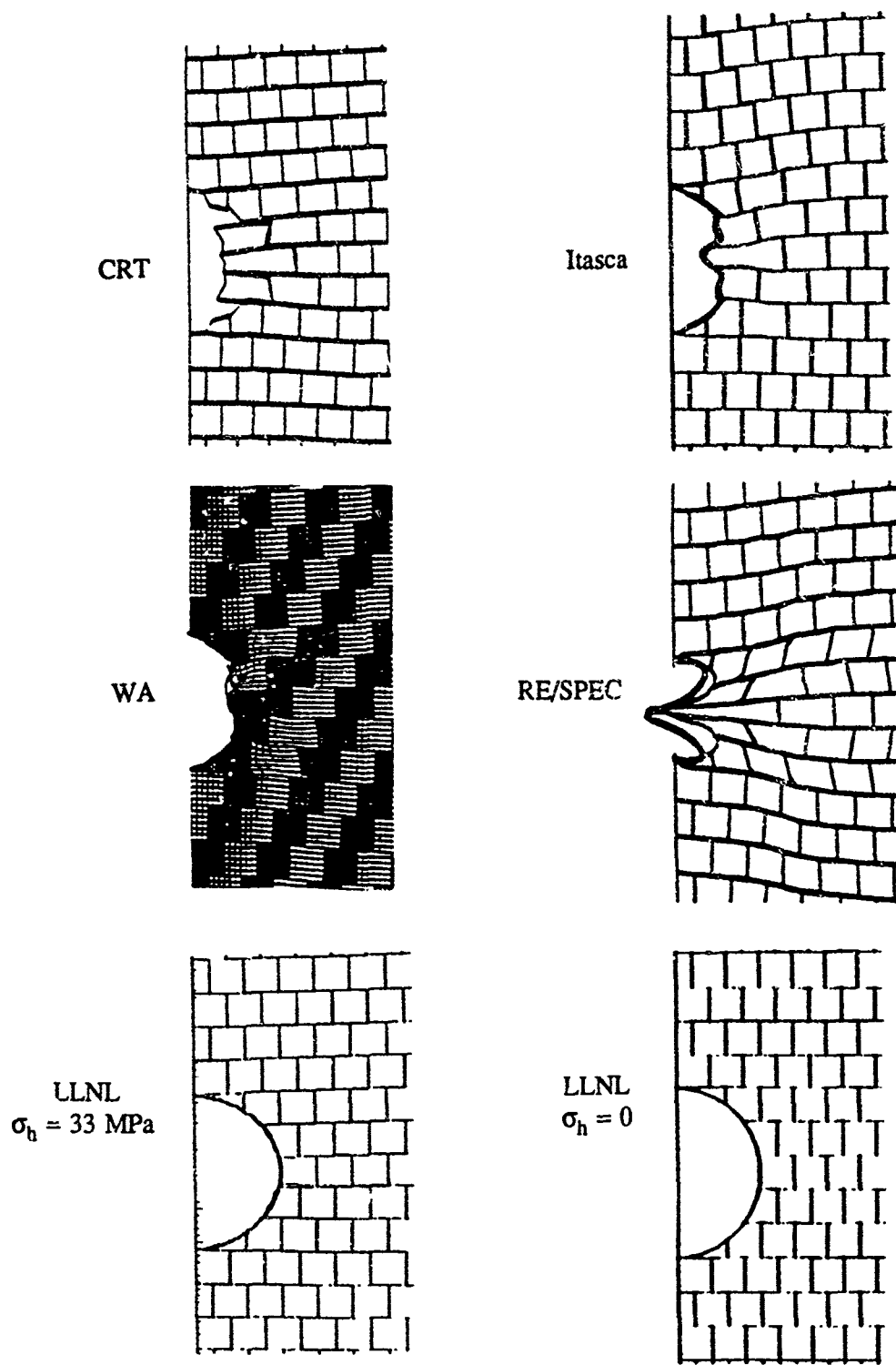


Figure 4-19. Deformed tunnel shapes at end of positive phase (about 120 ms). Displacements are magnified by 10.

4.3.3 Orthotropic Elastic Predictions of Stresses.

At a propagation speed of about 2.5 m/ms, the rising portion of the incident pulse extends over about 25 m and the decaying portion over more than 200 m. Both of these distances are fairly large compared with the tunnel diameter of 5 m, so there is a possibility that some aspects of the response will be quasi-static. Moreover, as noted before, the dilatancy causes the plastic response to be "less plastic," and in particular there is less softening on initial loading above the yield point than there would otherwise be. So we might expect that during initial loading, a two-dimensional, static, orthotropic, elastic solution could shed some light on the stress distributions around the tunnel. To this end, in this section we will construct such a solution under the loading conditions in force when the peak incident stress just reaches the tunnel center.

The derivation of the orthotropic elastic solution follows Lekhnitski (1966). He explains the general approach to two-dimensional problems using complex potentials, and provides some examples for infinite regions with holes, but does not specifically work out the full stress fields for the fundamental problem of interest here, viz., an infinite region with a hole and with uniaxial stress at infinity. So we will fill in the details needed to derive the fundamental solution, and show how this solution can be rotated and superposed to build up one containing the effects of vertical and horizontal free-field stress and internal pressure to represent the effect of the liner.

This first matter to be addressed is the choice of orthotropic elastic constants. In this section only, let x , y , and z represent the horizontal, vertical, and out-of-plane directions respectively. The elastic relation among macroscopic normal stresses and strains in implicitly jointed material is similar to (3-18):

$$\begin{aligned} E\varepsilon_x &= \left(1 + \frac{E}{wk_N}\right)\sigma_x - \nu\sigma_y - \nu\sigma_z, \\ E\varepsilon_y &= -\nu\sigma_x + \left(1 + \frac{E}{wk_N}\right)\sigma_y - \nu\sigma_z, \\ E\varepsilon_z &= -\nu\sigma_x - \nu\sigma_y + \sigma_z. \end{aligned}$$

We are interested in plane strain in the z -direction, so we set $\varepsilon_z = 0$. The resulting expressions for normal strains, when compared with the standard forms

$$\varepsilon_x = \frac{1}{E_1}\sigma_x - \frac{\nu_{21}}{E_2}\sigma_y, \quad \varepsilon_y = -\frac{\nu_{12}}{E_1}\sigma_x + \frac{1}{E_2}\sigma_y,$$

yield

$$\frac{1}{E_1} = \frac{1}{E_2} = \frac{1-\nu^2}{E} + \frac{1}{wk_N}, \quad \nu_{12} = \nu_{21} = \frac{\nu(1+\nu)}{1-\nu^2 + E/wk_N}.$$

For shear components, we write the engineering shear strain γ_{xy} as a sum of two parts, the first τ_{xy}/G due to intact rock shearing, and the second due to joint elastic shear. For the latter, note that a square block of intact rock of any size w , bounded by joints, will suffer relative tangential displacements τ_{xy}/k_S across each pair of parallel sides, so the corresponding shear strain averaged over the block is $2\tau_{xy}/wk_S$. The net shear compliance is thus

$$\frac{1}{G_{12}} = \frac{1}{G} + \frac{2}{wk_S}.$$

The joint normal stiffness is the only original elastic constant that varies with stress. For this analysis we will hold it constant at its value when joint closure is half of joint thickness.

Next, we must solve the characteristic equation

$$\frac{1}{E_1} \lambda^4 + \left(\frac{2\nu_{12}}{E_1} + \frac{1}{G_{12}} \right) \lambda^2 + \frac{1}{E_1} = 0,$$

which is a necessary condition for the general functional form of the complex potentials assumed by Lekhnitski to satisfy the equation of strain compatibility expressed in terms of stresses. The two positive roots can be written

$$\lambda_{1,2} = \left[\frac{1 \mp (1-4\varepsilon^4)^{1/2}}{2\varepsilon^2} \right]^{1/2},$$

where, after using the above relations among elastic constants,

$$\varepsilon^2 = \frac{1}{2} \frac{1-\nu + 2G/wk_N}{1-\nu + 2G/wk_S}.$$

The essence of Lekhnitski's procedure is that if $\Phi_1'(z)$, $\Phi_2'(z)$ are practically any complex valued potential functions of a complex variable z , then the stress fields

$$\begin{aligned}\sigma_x &= -2\text{Re}[\lambda_1^2 \Phi_1'(z_1) + \lambda_2^2 \Phi_2'(z_2)] \\ \sigma_y &= 2\text{Re}[\Phi_1'(z_1) + \Phi_2'(z_2)] \\ \tau_{xy} &= 2\text{Im}[\lambda_1 \Phi_1'(z_1) + \lambda_2 \Phi_2'(z_2)]\end{aligned}$$

will satisfy all the equations of two-dimensional static orthotropic elasticity provided

$$z_k = x + i\lambda_k y, \quad k = 1, 2; \quad i = (-1)^{1/2}.$$

The task now is to find potential functions for which the stresses satisfy the appropriate boundary conditions. For remote uniaxial stress σ_h in the horizontal (x) direction the appropriate functions are

$$\Phi_k'(z_k) = \frac{a\sigma_h}{2[z_k^2 + a^2(\lambda_k^2 - 1)]^{1/2}(\lambda_{3-k} - \lambda_k)\zeta_k}, \quad \zeta_k = \frac{z_k + [z_k^2 + a^2(\lambda_k^2 - 1)]^{1/2}}{a(1 + \lambda_k)}, \quad k = 1, 2$$

where a is the radius of the opening. This completes the derivation of the fundamental solution.

The problem of interest is that of a tunnel loaded by vertical and horizontal free-field stresses as well as internal loads due to the liner. We will approximate the latter by a uniform internal pressure p_l . The full solution for any stress component σ_i can be built up by superposition as follows. Let $\hat{\sigma}_i(r, \omega)$ be the stress component at radius r from the center of the tunnel and angle ω from the horizontal, corresponding to a *unit* remote load in the horizontal direction. Then by linearity, the solution for horizontal free field stress σ_h will be $\sigma_h \hat{\sigma}_i(r, \omega)$. This corresponds exactly to the fundamental solution derived above. For the problem of interest there are two other sources of loading, vertical free field stress σ_v and internal pressure p_l . Because the implicitly jointed medium is symmetric about 45° lines, the solution for the former is $\sigma_v \hat{\sigma}_i(r, \pi/2 - \omega)$. For the internal pressure we superpose three more fields: a uniform pressure p_l everywhere, and the fields $-p_l \hat{\sigma}_i(r, \omega)$, $-p_l \hat{\sigma}_i(r, \pi/2 - \omega)$ due to horizontal and vertical free field *tensions* to cancel out the uniform pressure there. This completes the solution for the stresses around a statically, biaxially loaded, internally pressurized opening in an infinite orthotropic elastic medium.

To apply this analysis to the situation at peak stress arrival time, we set $\sigma_v = 100$ MPa, $\sigma_h = 33$ MPa, and $p_l = 8$ MPa. One final adjustment is needed: because as already noted the free field stress varies in the vertical direction, after evaluating the stresses by superposition as described above, the result is then scaled down by an amount representing the locally lower free field stress level. The results are plotted in Figures 4-13 and 4-14 as the curves labelled "elastic". The agreement with numerically derived results is striking. Disagreements arise where expected, i.e., when stresses are high and plasticity comes strongly into play (radial stresses at $\pm 45^\circ$ at intermediate radii, tangential at 0° and $\pm 90^\circ$ at the tunnel wall). But the intermediate maxima in tangential stress along the $\pm 45^\circ$ radials are mimicked, and

decay rates beyond the maxima in all cases are well approximated. The radial stresses above and below the tunnel (Figure 4-13) closely agree with the numerical solutions. This confirms the earlier statements concerning the extent of the relief provided by the tunnel wall.

In Figure 4-14 the vertical scale for tangential stress was cut off at 160 MPa for clarity, owing to the very large stress concentrations in the elastic solution. In particular, the tangential stress at the tunnel wall along the horizontal radial comes out at 673 MPa. This compares with a value of 259 MPa from an isotropic elastic analysis under the same loading conditions. In the orthotropic elastic solution the high stress concentration is very localized near the tunnel wall. In the first meter, the tangential stress drops to 144 MPa, i.e., by a factor of 4.7. As such, the orthotropic elastic solution would not be expected to accurately represent the stresses near the tunnel in an explicitly jointed medium, even if the blocks and joints remained elastic. However, the more severe concentration under homogeneous orthotropic conditions (compared with isotropic) suggests that the global orthotropy of the jointed medium may be leading to more severe tunnel deformations than would arise in an isotropic medium with the same vertical and horizontal properties.

4.3.4 Remarks on the Numerical Solutions to Problem 4.

Three of the five participants (CRT, WA, Itasca) obtained numerical solutions which—where comparisons were possible—agree with each other in most practical respects. All of these solutions appear credible, based on the significant body of evidence available, i.e.,

- Use of rational continuum models to represent the rock,
- Use of physically based models for the joints,
- Compatibility of results with basic understanding of wave propagation processes,
- Absence of obvious numerical artifacts such as spurious reflections,
- Comparison of stresses and strains with complete and partial analytic solutions in all the benchmark problems.

RE/SPEC's numerical solution to problem 4 differs significantly from the first three, for example in springline closure (Figure 4-12), radial stresses above and below the tunnel at peak stress arrival (Figure 4-13), and radial and tangential stresses along the other radials at the end of the positive phase (Figures 4-15 and 4-16). In the case of the stresses at the peak stress arrival time, RE/SPEC's solution also differs from the orthotropic elastic solution, while the latter agrees well with CRT and Itasca's numerical results and does so for reasons that we believe we understand. The large springline closure could be related to a spurious, compressive reflection from the lower boundary of the computational grid. There is no obvious explanation for the significant residual stresses around the tunnel at the end of the positive phase (Figures 4-15 and 4-16). There do appear to be explanations for most of the other identified shortcomings and breakdowns in RE/SPEC's numerical solutions to the earlier problems, and with further effort the

results could probably be corrected. However, the totality of evidence developed during this study suggests that this solution to problem 4 is not as accurate as the aforementioned three.

LLNL's approach omits a great deal of pertinent physics, most glaringly the behavior of the rock as a deformable continuum. A glance at Figure 4-19 shows convincingly that when the blocks as specified in problem 4 are permitted to deform, they will do so, and their deformations will contribute substantially to the conventional indices of tunnel distress, viz., tunnel closure. Moreover, particularly with respect to springline closure, the coupling between vertical and horizontal stresses and deformations plays a crucial role. There is no mechanism in the LLNL model for directly representing this coupling. LLNL attempted to approximate the effect by imposing a constant 33 MPa horizontal stress. The result is seen in Figure 4-12: even with the imposed horizontal stress, the springline closure is still negative (i.e., the springline elongates), in contrast with the expected result in the face of dilatant rock response. More generally, the pattern of deformations depends crucially on the distribution of stresses near the tunnel, and the LLNL approach cannot accurately estimate these stresses. It is for these reasons that the approach seems ill-suited for the problems at hand. This is not to say that there aren't certain problems for which it may be applicable. But to be useful it would have to be accompanied by guidelines for its applicability.

SECTION 5

CONCLUSIONS

The primary objective of the benchmark calculation study was to understand the effect of computational approach on predictions of tunnel deformations. We can only claim success in meeting that objective by adopting a rather broad view of what comprises a computational approach. That is, we must include more than purely numerical issues. In most cases where we have identified problems or differences and where there is an apparent cause, that cause lies in the way the medium was idealized. For example,

- (1) The LLNL approach oversimplified the continuum physics of the rock by lumping it in the joints, and this probably led to their substantially different results from all the others.
- (2) In some early solutions by WA the normal stiffness of the joints was based on the properties of the intact rock and therefore unrepresentative of the specified joint stiffness. The code was modified so that a constant stiffness approximating the actual normal joint stiffness could be specified. The joints still did not have the specified nonlinear behavior, but they did have a constant stiffness much closer to the average over the expected range of joint closures. With this modification, the reason for the stiffness deviation was understood, and was due to a conscious choice in an area that could now be regarded as material idealization.
- (3) Itasca and WA both chose to use an isotropic model for the implicitly jointed region. A possible result of this is the discrepancy in horizontal stresses across the implicit/explicit boundary noted in Figure 4-9.

There are also a few examples of issues more clearly and classically numerical in nature:

- (4) The WA sliding interface model was causing a great deal of numerical chatter in problem 2, the first one in this study where it was used. After changing certain features of the model other than the stiffness (see Section E4), the problem was resolved.
- (5) RE/SPEC had a problem with the nonreflecting boundary in problem 3, and recognized that it was caused by the wave speeds used in the boundary condition. They did not elect to remedy the problem during the course of this study. The spurious bottom reflection probably caused higher stresses at the end of the free field positive phase (compared with other participants), and this in turn may have led to significantly larger springline closures.

It is important to recognize that there is no definitive proof of the cause-and-effect relationships suggested above. They rely more on physical reasoning and induction than

deduction. In fact, as indicated for example in the discussion on divergent flow, glib physical arguments may either fail or reveal themselves as oversimplifications when placed under closer scrutiny.

In particular, statement (3) above, while apparently logical, could be questioned. As suggested in Section 4.2.3, by judicious choice of material parameters, an isotropic elastic model could be made to give the same coupling between vertical and horizontal stresses and strains as an orthotropic one. The material parameters quoted in Appendix E for WA's implicit model correspond to a smaller Poisson's ratio than for intact rock, as do the anisotropic elastic relationships of Section 4.3.3, when used with the *unstrained* stiffness of the joints. But as the joints compress and stiffen, Poisson's ratio increases. The situation is obviously more complex than first meets the eye.

As to the overall success of the calculations themselves, the remarks in Section 4.3.4 summarize the author's evaluation. But even the organizations which appeared to successfully negotiate problem 4 did not do so without breakdowns and detours along the way. If the tunnel deformation calculations had not been preceded by a sequence of progressively more challenging problems, the results would have been much more scattered. Often a calculator is faced with a *more* complex problem than any of those treated here, and *fewer* resources to devote to it. Some of the lessons are obvious: the calculator should take care to include all the correct physics he can, while the customer should support as much preliminary work as possible, and barring that, maintain a healthy sense of skepticism about the outcome of any isolated, complex, numerical simulation.

SECTION 6

REFERENCES

Allen, M.P., and Tildesley, D.J., *Computer Simulations of Liquids*, Clarendon Press, Oxford, 1987. (UNCLASSIFIED)

Bandis, S.C., Lumsden, A.C., and Barton, N.R., "Fundamentals of Rock Joint Deformation," *Intern. J. Rock Mech. Mining Sci. & Geomech. Abstr.*, Vol. 20, No. 6, pp. 249-268, 1983. (UNCLASSIFIED)

Bathe, K.J. and Wilson, E.L., Iding, R.H., *NONSAP: Structural Analysis Program for Static and Dynamic Response of Nonlinear Systems*, Report No. UC SESM 74-3, February 1974. (UNCLASSIFIED)

Bathe, K.J., and Wilson, E.L., *Numerical Methods in Finite Element Analysis*, Prentice-Hall, Englewood Cliffs, NJ, 1976. (UNCLASSIFIED)

Belytschko, T., "An Overview of Semidiscretization and Time Integration Procedures," *Computational Methods for Transient Analysis*, Chapter 1, pp. 1-65, Elsevier Science Publishers, B.V., New York, 1983. (UNCLASSIFIED)

Callahan, G.D., and Fossum, A.F., *Quality Assurance Study of the Special Purpose Finite Element Program SPECTROM: II. Plasticity Problems*, ONWI-141, prepared by RE/SPEC Inc., Rapid City, SD, for the Office of Nuclear Waste Isolation, Battelle Memorial Institute, Columbus, OH, 1982. (UNCLASSIFIED)

Callahan, G.D., Fossum, A.F., and Svalstad, D.K., *Documentaton of SPECTROM-32: A Finite Element Thermomechanical Stress Analysis Program*, DOE/CH/10378-2, prepared by RE/SPEC Inc., Rapid City, SD for the U.S. Department of Energy, Chicago Operations Office, 1989. (UNCLASSIFIED)

Chen, W.F. and Han, D.J., *Plasticity for Structural Engineers*, Springer-Verlag, New York, 1988. (UNCLASSIFIED)

Cundall, P.A., *Rational Design of Tunnel Supports: A Computer Model for Rock Mass Behavior Using Interactive Graphics for the Input and Output of Geometric Data*, US Army Corps of Engineers, Technical Report MRD-2-74, Vicksburg, MS, 1974. (UNCLASSIFIED)

Cundall, P.A., "Adaptive Density-Scaling for Time-Explicit Calculations," in *Proceedings of the 4th International Conference on Numerical Methods in Geomechanics*, pp. 23-26, 1982. (UNCLASSIFIED)

Cundall, P.A., and Hart, R.D., *Analysis of Block Test No. 1 Inelastic Rock Mass Behavior: Phase 2 - A Characterization of Joint Behavior (Final Report)*, Itasca Consulting Group, Rockwell Hanford Operations, Subcontract SA-957, March 1984. (UNCLASSIFIED)

Cundall, P.A., and Lemos, J.V., "Numerical Simulation of Fault Instabilities with the Continuously-Yielding Joint Model," *Rockbursts and Seismicity in Mines*, A. A. Balkema, Rotterdam, pp. 147-152, 1990. (UNCLASSIFIED)

Dimagio, F.L. and Sandler, I.S., "Material Model for Granular Materials," *J. of Eng. Mech. Div.*, ASCE, Vol. 97, 1971. (UNCLASSIFIED)

Flanagan, D.P. and Belystchko, T., "A Uniform Strain Hexahedron and Quadrilateral with Orthogonal Hourglass Control," *Intern. J. Numer. Methods in Eng.*, Vol. 17, pp. 679-706, 1981. (UNCLASSIFIED)

Flanagan, D.P. and Belystchko, T., "Eigenvalues and Stable Time Steps for the Uniform Strain Hexahedron and Quadrilateral," *J. Appl. Mech.*, 84-APM-5. Transactions of the ASME, 1984. (UNCLASSIFIED)

Goodman, R.E., *Methods of Geological Engineering in Discontinuous Rocks*, West Publishing Company, New York, 1976. (UNCLASSIFIED)

Halquist, J.O., Goudreau, G.L., Benson, D.J., "Sliding Interfaces with Contact-impact In Large-Scale Lagrangian Computations," *Computer Methods in Appl. Mech. and Eng.*, Vol. 51, 1985. (UNCLASSIFIED)

Heuze, F.E., Walton, O.R., Maddix, D.M., Shaffer, R.J. and Butkovich, T.R., "Analysis of Explosions in Hard Rocks: The Power of Discrete Element Modeling," *Proceedings Intern Con. Mech. Jointed and Faulted Rocks*, Vienna, Austria, (A.A. Balkema, Brookfield, VT) pp. 21-28, April 18-20, 1990. Also, Lawrence Livermore National Laboratory, UCRL-JC-103498. (UNCLASSIFIED)

Ito, Y.M., England, R.H. and Nelson, R.B., "Computational Method for Soil Structure Interaction Problems," *Computers and Structures*, Vol. 13, No. 1-3, pp. 157-162, 1981. (UNCLASSIFIED)

Key, S.W., Beisinger, Z.E., and Krieg, R.D., *HONDO II: A Finite Element Computer Program for the Large Deformation Dynamic Response of Axisymmetric Solids*, SAND78-0422, Sandia National Laboratories, Albuquerque, NM, 1978. (UNCLASSIFIED)

Labreche, D.A., and Petney, S.V., *The SPECTROM-31 Compliant Joint Model: A Preliminary Description and Feasibility Study*, SAND85-7100, prepared by RE/SPEC Inc., Albuquerque, NM, for Sandia National Laboratories, Albuquerque, NM, 1987. (UNCLASSIFIED)

Lekhnitski, S.G., *Anisotropic Plates*, University Microfilms, Ann Arbor, MI, 1966. (UNCLASSIFIED)

Lemos, J.V., *A Distinct Element Model for Dynamic Analysis of Jointed Rock with Application to Dam Foundations and Fault Motion*, Ph.D. Thesis, University of Minnesota, 1987. (UNCLASSIFIED)

Levine, H.S., "A Two Surface Plastic and Microcracking Model for Plain Concrete," *Nonlinear Numerical Analysis of Reinforced Concrete*, Winter Annual Meeting, ASME, Phoenix, AZ, November 1982. (UNCLASSIFIED)

Levine H.S., Ludwig C.J., Vaughan, D.K., Isenberg, J., "Comparison of Two Different Interface Approaches for Modeling in Large Scale Interaction Problems", *J. Appl. Mech.*, ASME, Vol. 94, 1989. (UNCLASSIFIED)

Lysmer, J. and Kuhlemeyer, R.L., "Finite Dynamic Model for Infinite Media", *J. Eng. Mech. Div.*, ASCE, Vol. 95, pp. 859-877, August 1969. (UNCLASSIFIED)

Muki, Y. Nelson, R.B. and Ito, Y.M., *Numerical Modeling of Jointed Limestone*, DNA Final Report Contract DNA001-89-C-2105, 1992 (To be published). (UNCLASSIFIED)

Senseny, P.E., *UTP Benchmark Definition*, 29 March, 1991. (UNCLASSIFIED)

Simons, D.A., *UTP Benchmark Problem 2-S Definition*, 6 May, 1991. (UNCLASSIFIED)

Singh, B., "Continuum Characterization of Jointed Rock Mass," *Int. J. Rock Mech. Mining Sci. & Geomech. Abstr.*, Vol. 10, 1973. (UNCLASSIFIED)

Taylor, L.M., and Flanagan, D.P., *PRONTO 2D: A Two-Dimensional Transient Solid Dynamics Program*, SAND86-0594, Sandia National Laboratories, Albuquerque, NM., 1987. (UNCLASSIFIED)

Vaughan, D.K. and Richardson, E., "FLEX Users Manual", Weidlinger Associates Report, Version 1-H.2, June 1991. (UNCLASSIFIED)

Walton, O.R., *Particle Dynamics Modeling of Geological Materials*, Lawrence Livermore National Laboratory Report, UCRL-52925, 1980. (UNCLASSIFIED)

Walton, O.R., "Explicit Particle Dynamics Model for Granular Materials," *Numerical Methods in Geomech.*, pp. 1261-1268, A.A. Balkema, Brookfield, VT, 1982. (UNCLASSIFIED)

Walton, O.R., Maddix, D.M., Butkovich, T.R., and Heuze, F.E., "Redirection of Dynamic Compressive Waves in Materials With Nearly Orthogonal and Random Joint Sets," *Am. Soc. Mech. Eng. AMD*, v.117, pp. 65-72, ASME, New York, NY, 1991. (UNCLASSIFIED)

APPENDIX A

DESCRIPTION OF THE PRONTO2D COMPUTER CODE USED IN THE UNDERGROUND TECHNOLOGY PROGRAM BENCHMARK ACTIVITY

John Osnes (RE/SPEC), Ben H. Thacker (SwRI),
and David S. Riha (SwRI)

A1. INTRODUCTION.

PRONTO2D is a two-dimensional transient solid dynamics code for analyzing large deformations of highly nonlinear materials subjected to extremely high strain rates (Taylor, L. M. and Flanagan, D. P., 1987). It is the latest in a series of transient dynamics finite element codes that has been developed at Sandia National Laboratories, beginning with HONDO (Key, S. W., et al., 1978). As such, PRONTO2D contains a number of state-of-the-art numerical algorithms, including an adaptive timestep control algorithm, a robust hourglass control algorithm, a very accurate incremental rotation algorithm, and a robust surface contact algorithm. Four-noded, uniform-strain, quadrilateral elements with single-point integration are used in the finite element formulation. Beyond its general capabilities, PRONTO2D was chosen for the benchmark calculations because new constitutive models are readily added and because a three-dimensional derivative of the program is available (PRONTO3D) if needed by the UTP in the future.

The two features that make the UTP benchmark calculations relatively unique among large-deformation solid dynamics problems are:

- (1) A jointed rock mass subject to loading conditions that could result in large relative motions (sliding) between adjacent rock blocks, and
- (2) Loading conditions that could result in substantial tensile failure, plastic deformation, and dilation within the rock blocks.

The joints also affect the elastic behavior of the rock mass by reducing its elastic moduli from the intact rock values. Further, the elastic moduli of jointed rock generally are nonlinear functions of the joint apertures.

The surface contact algorithm in PRONTO2D is directly applicable to modeling the slip between adjacent rock blocks. It is designed to simulate smooth, cohesionless surfaces with shear strengths defined in terms of static and dynamic coefficients of friction. In the benchmark problems, the static coefficient of friction is the tangent of the joint friction angle. The friction coefficient does not decay during sliding, so the dynamic coefficient of friction is equal to the static coefficient.

The surface contact algorithm does *not* provide a means to model the elastic behavior of the joints. Consequently, the approach used in the benchmark problems is to superpose the nonlinear stress-displacement response of the joints and the linear stress-strain response of the intact rock. The result is a composite material whose elastic behavior is equivalent to a jointed rock mass. This approach has been developed and used successfully by other modelers

(Labreche, D. A. and Petney, S. V., 1987), and it is referred to as the Complaint Joint Model (CJM). Note that the elastic behavior of jointed rock masses as simulated by the CJM is inherently anisotropic because the stress-strain response normal to a joint set is substantially different from the response tangential to the joint set.

Nine constitutive models are available in PRONTO2D. They include an elastic-plastic model with a Mises yield criterion that is directly applicable to modeling the tunnel liner. The models also include an elastic-plastic model with a two-invariant yield surface. However, the flow rule in that model is nonassociative and cannot be reduced to an associative form. Consequently, to perform the benchmark calculations, a new constitutive model (Drucker-Prager) was implemented in PRONTO2D for modeling the plastic deformation within the rock blocks. The new model also simulates the limited tensile strength of the intact rock. The CJM is incorporated within the model to simulate the elastic response of the intact rock, including joint sets.

In summary, the approach to modeling the jointed rock mass uses:

- (1) The surface contact algorithm in PRONTO2D to explicitly model slip between rock blocks along joints.
- (2) A new constitutive model that:
 - (a) Models the elastic behavior of the rock and joint sets as an equivalent composite material using the Compliant Joint Model to calculate the nonlinear, anisotropic stress-strain response of the rock mass.
 - (b) Simulates yield of the intact rock using an incremental plasticity method with a Drucker-Prager yield function and the associated plastic potential function.
 - (c) Simulates tensile failure using a limited-tension algorithm to reduce principal stress components that exceed the tensile strength to the tensile strength while maintaining the original principal stress directions.

A2. NUMERICAL FORMULATION.

A2.1 Explicit Time Integration.

The equations of motion are integrated using a modified central difference scheme in PRONTO2D. The velocities are integrated with a forward difference and the displacements are integrated with a backward difference. This scheme is expressed as

$$\ddot{u}_t = \frac{f_t^{EXT} - f_t^{INT}}{m}$$

$$\dot{u}_{t+\Delta t} = \dot{u}_t + \Delta t \ddot{u}_t$$

$$u_{t+\Delta t} = u_t + \Delta t \dot{u}_{t+\Delta t}$$

where f_t^{EXT} is the external nodal force, f_t^{INT} is the internal nodal force, m is the nodal point lumped mass, and Δt is the time increment. This central difference operator is conditionally stable and the Courant stability limit is given by the highest eigenvalue ω_{max} of the system (Bathe, K. J. and Wilson, E. L., 1976).

$$\Delta t \leq \frac{2}{\omega_{max}}$$

Flanagan and Belytschko (1984) provided eigenvalue estimates for the uniform strain quadrilateral used in PRONTO2D.

Numerical damping is introduced in the solution by adding artificial viscosity. This prevents high velocity gradients from collapsing an element before it has a chance to respond and to quiet truncation frequency ringing. The technique used in PRONTO2D is to add viscosity to the "bulk" response. This generates a viscous pressure in terms of the volume strain rate.

A2.2 Four Node Uniform Strain Element.

PRONTO2D uses a four-noded two-dimensional uniform strain element in the finite element formulation. A one point integration of the element under-integrates the element but provides a large computational advantage over a two-by-two integration rule. However, this results in a rank deficiency for the element that may cause spurious zero energy (hourglass) modes.

The mean stress-strain formulation for the uniform strain element considers only a fully linear field. Any remaining nodal velocity field is the hourglass field. Possibly severe unrestricted mesh distortion can occur if these modes are excited. The method used in PRONTO2D isolates the hourglass modes so they may be treated independently of the rigid body and uniform strain modes (Flanagan, D. P. and Belytschko, T., 1981).

A2.3 Material Behavior.

Several classical yield surfaces that are defined in terms of the first stress invariant and the second deviatoric stress invariant have been used to model plasticity in rock. They include the linear Mohr-Coulomb and the Drucker-Prager yield criteria. These criteria have been reviewed by Callahan and Fossum (1982). The Drucker-Prager yield function was used for modeling the plasticity in the benchmark problems. This yield function is defined as

$$f(\sigma_{ij}) = \sqrt{J_2} - \alpha I_1 - k$$

where σ_{ij} are the components of the stress tensor, α and k are material constants, I_1 is the first invariant of the stress tensor, and J_2 is the second invariant of the *deviatoric* stress tensor. The yield surface is the locus of stress states at which the value of the yield function is zero ($f = 0$). Consequently, the Drucker-Prager yield surface is a cone in principal stress space with the axis of the cone along the hydrostat. The specification of perfect plasticity in the benchmark problems means that the Drucker-Prager yield surface does not change as a result of plastic deformation (i.e., the values of α and k do not change).

The Drucker-Prager and the Mohr-Coulomb yield criteria are equivalent only at certain stress states, depending on how the Drucker-Prager material constants are evaluated. To match the Mohr-Coulomb criterion in triaxial compression, the material constants must be evaluated as follows:

$$\alpha = \frac{2 \sin \phi}{\sqrt{3} (3 - \sin \phi)}$$

$$k = \left(\frac{2\sqrt{3} \cos \phi}{3 - \sin \phi} \right) c_0$$

where ϕ and c_0 are the Mohr-Coulomb friction angle and cohesion, respectively. The resultant Drucker-Prager yield surface circumscribes the Mohr-Coulomb yield surface.

The stress state is elastic when the yield function is negative ($f < 0$). When the stress state is on the yield surface ($f = 0$) and the loading condition is such that it would result in $f \geq 0$, the resulting deformation is plastic. The components of the resultant plastic strain tensor are defined in terms of the flow rule, which is classically stated as proportional to the gradient of a plastic potential function $g(\sigma_{ij})$. The proportionality constant is determined by the consistency condition which requires that the stress state remain on the yield surface during plastic deformation. When the plastic potential function and the yield function coincide for all stress states ($g = f$), the flow rule is said to be associated with the yield function, as required in the benchmark problems.

An incremental method using tangent stiffness (Chen, W. F. and Han, D. J., 1988) is used to implement Drucker-Prager plasticity in the constitutive model that was added to PRONTO2D for the benchmark problems. The incremental stress-strain relationship can be expressed in the following general form:

$$d\sigma_{ij} = \left[C_{ijkl} - \frac{C_{ijmn} \frac{\partial g}{\partial \sigma_{mn}} \frac{\partial f}{\partial \sigma_{pq}} C_{pqkl}}{\frac{\partial f}{\partial \sigma_{rs}} C_{rstu} \frac{\partial g}{\partial \sigma_{tu}}} \right] d\epsilon_{kl}$$

where $d\sigma_{ij}$ and $d\epsilon_{kl}$ are the components of the incremental stress and strain tensors, respectively, C_{ijkl} are the components of the elastic coefficient tensor, and repeated subscripts indicate summation. The coefficient tensor in the brackets represents the elastic-plastic tensor of tangent moduli for an elastic-perfectly plastic material. The quantities in the brackets, including C_{ijkl} for a nonlinear elastic material such as in the CEM, are evaluated at the current stress state.

For the Drucker-Prager yield surface, the partial derivatives of the yield function with respect to the stress components are

$$\frac{\partial f}{\partial \sigma_{ij}} = \frac{s_{ij}}{2\sqrt{J_2}} - \alpha \delta_{ij}$$

where s_{ij} are the components of the deviatoric stress tensor ($s_{ij} = \sigma_{ij} - \delta_{ij}I_1/3$) and δ_{ij} is the Kronecker delta function. In the constitutive model added to PRONTO2D the following extended form of the plastic potential function associated with the Drucker-Prager yield function is used:

$$g(\sigma_{ij}) = \sqrt{J_2} - \beta I_1 - k$$

where

$$\beta = \frac{2 \sin \psi}{\sqrt{3} (3 - \sin \psi)}$$

and ψ is the dilation angle. The plastic potential function results in an associated flow rule when the dilation angle equals the friction angle (so that $\beta = \alpha$ and $g = f$). The components of the flow rule (the partial derivatives of g with respect to σ_{ij}) are

$$\frac{\partial g}{\partial \sigma_{ij}} = \frac{s_{ij}}{2\sqrt{J_2}} - \beta \delta_{ij}$$

A2.4 Limited-tension Algorithm.

A limited-tension algorithm developed by Callahan (Callahan, G. D. and Fossum, A. F., 1982) and implemented in SPECTROM-32 (Callahan, G. D., et al., 1989) is used in the constitutive model to simulate tensile failure. In this algorithm the tensile strength at each integration point T_x is set initially to the intact tensile strength T_0 . At each integration point at each time step, the principal stresses ($\sigma_I \geq \sigma_{II} \geq \sigma_{III}$) and their unit direction vectors ($\hat{n}_I, \hat{n}_{II}, \hat{n}_{III}$) are calculated based on the trial stress state σ_{ij}^1 at that location and time. Each principal stress component that exceeds the tensile strength at the integration point T_x is set to the residual tensile strength T_r . In addition, the tensile strength at the integration point is set to T_r if T_x is exceeded. (Recall that tension is negative according to the sign convention, so exceeding T_x implies that the stress is less than $-T_x$ and the stress is set to $-T_r$.) The resultant stress state is calculated by transforming the principal stress components back to the global coordinate system while maintaining the original principal stress directions. This transformation is accomplished according to the following equation:

$$\sigma_{ij} = n_{1i} n_{1j} \sigma_I + n_{2i} n_{2j} \sigma_{II} + n_{3i} n_{3j} \sigma_{III}$$

where n_{ji} is the i^{th} component of unit direction vector \hat{n}_j .

In the limited-tension algorithm, the stress state is modified in a very direct way when the tensile strength is exceeded. The deformation field also is affected because modifying the stress state produces an imbalance between the external forces and the internal forces (the integral of the stress divergence). In turn, this imbalance results in accelerations and ultimately deformation in response to the tensile failure. Changing the tensile strength to a residual value after tensile failure allows the formation of tension cracks to be simulated by a reduction in strength. However, this approach to simulation of tensile cracking is very crude because it does not account for crack orientation and the resultant anisotropy in the tensile strength. It is justifiable when the principal stress directions are fairly constant throughout a simulation, so that the tensile direction and the resultant orientation of tension cracks are fairly constant. In general, this condition could not be ensured in the benchmark calculations. Consequently, the tensile strength is maintained at the intact value even after tensile failure (i.e., $T_r = T_o$).

A2.5 Implicit Rock Joint Modeling.

The compliant joint model (CJM) is a three-dimensional elastic model used to represent the mechanical response of a rock matrix with joints (Labreche, D. A. and Petney, S. V., 1987). The model implemented in PRONTO2D is a two-dimensional version of the CJM. The CJM assumes that the deformation of a jointed rock mass is caused by the combination of the elastic response of the rock matrix and the elastic response of the joints. The unfractured rock matrix is modeled as an isotropic linear elastic solid and the joints as a nonlinear elastic layer. The model consists of up to four joint sets with various spacing and orientation. The response of the CJM is effectively anisotropic due to the presence of the joint sets.

The displacement behavior normal to the joint plane varies nonlinearly with stress and the response is governed by the physical characteristics such as joint aperture, roughness and contact between joint surfaces, strength of the wall rock, and presence or absence of filling. The response is also governed by the recent movement history of the rock joint. The aperture change of a well-mated joint without filling can be represented by a hyperbolic relationship between the stress normal to joint plane and the joint closure (Bandis, S. C., et al., 1983 and Goodman, R. E., 1976). The form used in the CJM is given by the equation

$$\sigma_n = a \left(\frac{v_n}{\delta - v_n} \right)^m$$

where,

- σ_n - normal stress acting on the joint (compression positive)
- a - half-closure stress (stress to reduce the aperture to $\delta/2$)
- v_n - joint normal displacement (closure positive, zero when $\sigma_n = 0$)
- δ - maximum joint closure
- m - exponent

The stiffness normal to the joint, k_n , is defined by

$$k_n = \frac{\partial \sigma_n}{\partial v_n} = am \frac{\delta v_n^{m-1}}{(\delta - v_n)^{m+1}}$$

which is the slope of the nonlinear joint closure. For the Benchmark problems, $a = 125$ MPa and $m = 1$. This hyperbolic function is used in the numerical formulation for the normal stress-displacement response when the normal stress is compressive. A constant value of 10^{-4} times the dilatational modulus, $\lambda + 2\mu$, of the matrix is used for joint normal stiffness when the normal stress is tensile. This stiffness defines a linear, normal stress-normal displacement relationship for the joint in tensor. This small but nonzero stiffness avoids numerical singularities in the computations. The transmission of small tensile stresses by elements having moduli four orders of magnitude lower than the matrix are accepted as insignificant relative to typical compressive stresses.

The compressive normal stress-displacement relation is nonlinear and elastic. Thus, there is no path dependence and all joint closure is fully recoverable in this model.

The shear response of joints generally consists of a nearly linear rise to peak shear strength, followed by softening behavior with continuing shear. However, it is acknowledged that joint size dependence may alter this. The peak shear strength response of joints is supported by studies such as Goodman (1976) and Bandis (Bandis, S. C., et al., 1983). The shear stress of joints is known to be inelastic when the stress state approaches the peak shear strength. The CJM only models the elastic joint shear response. The shear stiffness, which is independent of the normal stiffness across the joint, relates the shear displacement to shear stress.

$$\tau = k_s v_t$$

where,

τ - shear strength

k_s - joint shear stiffness

v_t - joint displacement tangent to plane of joint

The shear stiffness is defined by

$$k_s = \frac{\partial \tau}{\partial v_t}$$

The CJM introduces anisotropy by reducing the composite modulus of the modeled rock mass in the direction normal to the joint in an otherwise linear elastic material. Computation of effective moduli is used to implement the softening effects of the joints. Stress equilibrium is the underlying assumption in the combined response of the rock matrix and the joint sets. The normal stress across the joint is equal to the stress in the rock matrix normal to the joint plane. The shear stress on the joint is equal to the shear stress in the rock matrix parallel to the joint plane.

Correspondingly, the strains in the rock matrix are combined with the strains in the joints additively. That is, the effective compliance for the rock mass is the sum of the compliances of the unfractured rock and the joint sets. The effective Young's modulus, \hat{E} , normal to a joint and the effective shear modulus, \hat{G} , parallel to a joint, are

$$\frac{1}{\hat{E}} = \frac{1}{E} + \frac{1}{k_n s}$$

$$\frac{1}{\hat{G}} = \frac{1}{G} + \frac{1}{k_s s}$$

where E and G are the elastic moduli of the rock matrix, k_n and k_s are the normal and shear stiffness of the joint set, and s is the spacing of the joints in the joint set.

The description of the compliant joint model is for an elastic material that models the elastic response of a jointed rock mass. However, the implementation of the limited tensile algorithm and Drucker-Prager plasticity allows a more realistic representation of the rock matrix.

A2.6 Explicit Rock Joint Modeling.

PRONTO2D treats contact as a kinematic constraint. That is, the algorithm modifies the accelerations of the nodes along the contact region such that the kinematic constraints are satisfied. The algorithm uses a partitioned approach to enforce compliance between two contact surfaces by allowing each surface to act as a master surface for a fraction of each time step and a slave for the remainder.

There are four steps involved in the contact algorithm. First, the contact surface geometry is recalculated at each time step and the predicted configuration is computed by integrating the motion without regard to the kinematic constraints required by the contact surfaces. The following quantities are calculated for each node:

$$\begin{aligned}\hat{a} &= f/m \\ \hat{v} &= v + \Delta t \hat{a} \\ \hat{x} &= x + \Delta t \hat{v}\end{aligned}$$

where f is the residual force vector (sum of external forces minus the sum of internal forces), m is the nodal mass, v , is the current velocity, and Δt is the time increment. The predicted kinematic quantities are denoted by the hat.

The second step is surface tracking, or the process of matching nodes along one surface with the mating surface. The algorithm used is to locate the spatially nearest master node to the possible point of contact. This procedure can be the most time consuming portion of the analysis for this type of problem. To streamline the tracking algorithm, the nearest master node to a given slave node at one time step is assumed to be in the vicinity of the nearest master node at the next time step. Therefore, at each time step, the nearest master node is the starting point for the search along the surface.

The next step is to determine contact or penetration. The slave node is oriented with respect to the master segments connected to the tracked master node. The depth and position coordinates are calculated for both master segments connected to the nearest master node. From these quantities, if the depth is positive, the slave node is penetrating the segment and if the position is positive then the slave node is along the segment. When the master surface forms an outside corner, there may be penetration of both segments. In this case, the algorithm determines with which master segment the slave surface is more strongly in contact. One limitation of the algorithm is that it can not detect a contact surface contacting itself.

The final step in the contact algorithm is to calculate the penetration forces imposed on the master surface by the slave surface to restore kinematic compliance. These forces are calculated as a fraction of the forces that would be imposed by the slave nodes if the master surface was rigid. This fraction is based on the fraction of each time step for which the surfaces act as master and slave. The roles are reversed for the remaining fraction of the time step. The accelerations are calculated to predict the response of the master surface to these penetration forces such that the response of each contacting slave node is constrained by its master nodes. The principle of virtual work is employed to define the accelerations of the master nodes in response to the penetration forces. When friction is present, the relative tangential motion of the contacting slave nodes is resisted. The magnitude of the tangential force exerted on the master surface on a slave node cannot exceed the friction force. Thus friction adds a tangential acceleration to the nodes in contact

A2.7 Transmitting Boundary Conditions.

A transmitting boundary is used to simulate a semi-infinite domain outside the boundary, where the wave speeds of the material on both sides of the boundary are the same. The region exterior to the boundary is replaced with an energy-absorbing boundary condition that behaves as if the energy is transmitted across the boundary. Thus, no energy is reflected back into the interior region.

The nonreflecting boundary is implemented in PRONTO2D according to a technique proposed by Lysmer (Lysmer, J. and Kuhlemeyer, R. L., 1969). The basic idea is to apply tractions at the boundary that will exactly cancel the stresses that would be reflected from a free surface. Hence, the numerical technique involves calculating and applying the following tractions to the surface of the nonreflecting boundary

$$\begin{aligned}\sigma_n &= -\rho V_p \dot{u}_n \\ \tau_s &= -\rho V_s \dot{u}_t\end{aligned}$$

where σ_n and τ_s are the normal and shear tractions; ρ , V_p , and V_s are the current density, compressional wave speed, and shear wave speed of the material along the boundary; and \dot{u}_n and \dot{u}_t are the normal and tangential components of the current velocity at the boundary. At each time step, PRONTO2D updates the tractions at the boundary using the current density and effective dilatational and shear moduli in each element along the boundary.

In calculating the current wave speeds, PRONTO2D assumes that the wave speeds are isotropic and independent of the orientation of the boundary. Obviously, the joint sets in a rock

mass yield an anisotropic medium in which the wave speeds depend on the incident direction. However, the anisotropy inherent in the CJM is not accounted for in the wave speed calculation in PRONTO2D. Consequently, the wave speeds used to calculate the tractions along the nonreflecting boundary are somewhat in error, the magnitude of which depends on the orientation of the boundary with respect to the principal directions of the anisotropy. This error results in a partial reflection of the incident stress.

APPENDIX B

THEORETICAL ASPECTS OF THE LLNL DIBS DISCRETE ELEMENT CODE USED IN THE DNA/UTP BENCHMARK EXERCISE

Francois Heuze

B1. INTRODUCTION.

Calculations for this study were performed with the LLNL Discrete Interacting Block System (DIBS) numerical model (Walton, O. R., 1982 and Walton, O. R., 1980) using a new "rounded corner" version of that model. DIBS was started from the algorithms of earlier "distinct-element" models (Cundall, P. A., 1974), and evolved at LLNL. It calculates the motion of each discrete polygonal block as it responds to contact forces, boundary and applied loads, and gravity. Arbitrary (convex) polygonal shapes are allowed for each particle or block. Several simplifying assumptions make the calculations tractable. All deformations take place at the contacts, which include the compliance of the rock blocks as well as that of the rock joints; meanwhile the blocks are kept rigid during the calculations. Note that all rock joints in DIBS are explicit; there is no implicit jointing. All starting contacts between polygons are assumed to be corner-on-side (i.e., temporary, sliding joint-elements or contacts are set-up at polygonal vertices, as needed). Small but finite "overlaps" occur as normal forces are developed. Similarly a finite, partially recoverable shear-strain develops in the contact before frictional sliding is initiated. In the rounded-corner version of the model, corner-corner contacts are also allowed, and they serve to allow a smooth transition in the direction of the contact normal, as a contact moves from one side onto the next.

DIBS has been applied to several analyses of the effects of nuclear and chemical explosions in jointed rocks (Heuze, F. E., et al., 1990).

B2. CONTACTS.

Information on contact detection and on corner-side contacts is available in (Walton, O. R., et al., 1991). The rounded-corner contact capability was developed for this study.

The rounded-corner version builds on the DIBS construct. From a user's point of view the model functions almost the same as the sharp-corner version. Internally, however, there are some significant differences. Input geometric data for each block contain the coordinates of an "outer" polygon with sharp corners; this is just the polygon the original DIBS model would use. When the problem is initialized (i.e., as geometric data are stored) a circle of fixed radius, r_c , is placed inside each vertex, tangent to the two adjacent sides. A new "inner" polygon is constructed connecting the centers of each of the corner circles. The side lengths of the inner polygon are exactly the same as the lengths of the line segments between tangent points on the outer polygon (Fig. B-1). The coordinates of the vertices of the inner polygon replace the original outer polygon coordinates in the computer storage arrays, and this inner polygon is used on all contact searching algorithms. Such a construct facilitates the use of most of the same searching algorithms for contact detection as were used in the original sharp-corner version of

the model. One major modification is that "overlap" is considered to occur when the two inner polygons are a distance apart equal to the sum of their respective corner radii. When a corner is contacting a side, the transformed local coordinates, x_t and y_t , are still determined by (Fig. B-2):

$$x_t = (x_c - x_a) \cos \phi + (y_c - y_a) \sin \phi$$

$$y_t = (y_c - y_a) \cos \phi - (x_c - x_a) \sin \phi$$

The overlap, α , is now defined to be

$$\alpha = r_i + r_j - y_t$$

where r_i and r_j are the radii of the corners for blocks I and J, respectively (Fig. B-2). This, in effect, moves the real surface (for determination of contact forces) a distance r_c outside the stored inner polygon. The other major difference for the rounded-corner model occurs when a contacting corner goes beyond either end of the "side" of the inner polygon, (i.e., $x_t < 0$, or $x_t > |AB|$). When this occurs, the contact is redefined to be a corner-corner contact.

The existing contact forces, including the currently partially recoverable tangential shear strain, are unaffected by the transition from one contact type to another. Only the indices in the linked list of contact, indicating which corner and/or side of which blocks comprise the contact, are affected. This contact information is in a separate, dynamic, linked list for each block. Each block's list contains the indices of the sides and/or corners of blocks contacted by that block.

B3. CONTACT FORCES.

The tangential friction force model also was described by Walton et al (1991). Because of the unique character of the nonlinear normal contact model, it is explained in more detail here.

The combined effects of an initially soft, inelastic joint and the approximate deformation of a stiff elastic block are modeled in DIBS with a loading curve that has a monotonically increasing slope. The stiffness asymptotically approaches a value equivalent to the elastic response of intact rock at high loads. The total deformation of both the block and the joint is assigned to the interface alone, in the model. Thus, the apparent overlap between two blocks in the model includes the displacement associated with the actual deformation of the block. If d is the distance between the centroids of two contacting blocks, and E_r is the modulus of the blocks, an equivalent spring stiffness, K_r , can be defined between the centroids, $K_r = E_r h t / d$, where h is the block height and t is the joint thickness (see Fig. B-3a). The model combines this "rock stiffness" with a contact relation for joints that has a vertical asymptote at a maximum joint closure, α_c . A commonly used form for such joint behavior (Goodman, R. E., 1976 and Bandis, S. C., et al., 1983) requires just two input parameters: the maximum joint closure, α_c and the normal joint stiffness, K_j . The force displacement assumed for the joint is $F = (K_j \alpha_c \alpha_j) / (\alpha_c - \alpha_j)$, where α_j is the displacement (i.e., closure) of the joint. The rock is assumed to be linear-elastic with a force displacement relation $F = K_r \alpha_r$, where α_r is the displacement associated with the rock deformation. Rearranging these expressions we obtain,

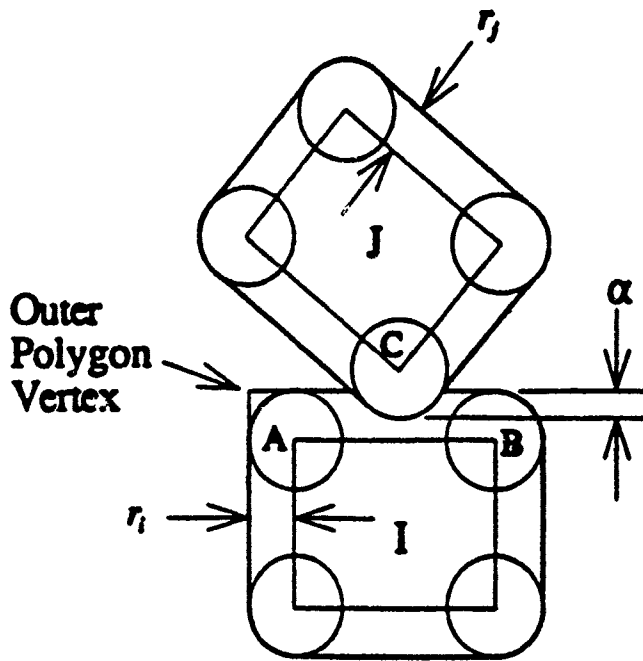


Figure B-1. Rounded-Corner Polygons.

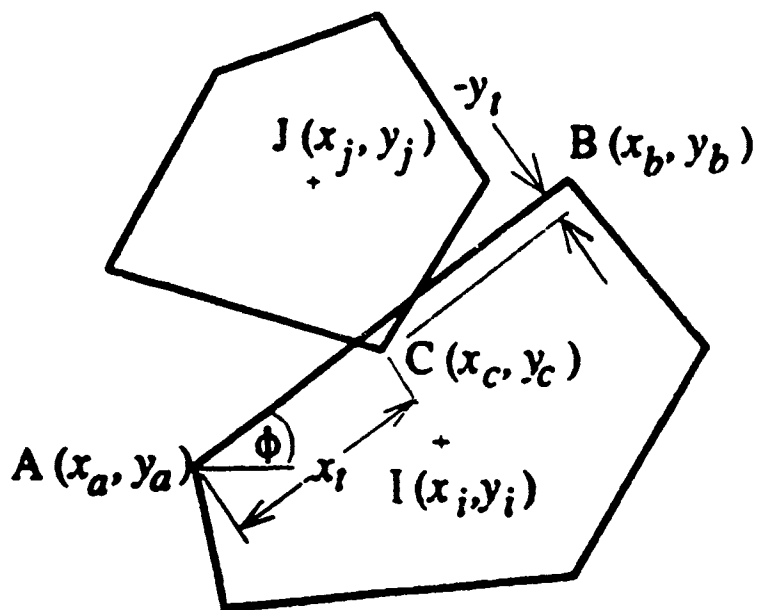


Figure B-2. Schematic of Corner-on-Side Contact in DIBS.

$$\alpha_j = \frac{F\alpha_c}{F + K_1\alpha_c} \quad \text{and} \quad \alpha_r = \frac{F}{K_r}$$

for the displacements of the joint and rock, respectively. The total displacement, α , is simply the sum of these two terms,

$$\alpha = \alpha_j + \alpha_r = \frac{F\alpha_c}{F + K_1\alpha_c} + \frac{F}{K_r} \quad (\text{B-1})$$

Equation (B-1) may be solved for F in terms of α ,

$$F = \frac{1}{2}[\alpha K_r - \alpha_c(K_1 + K_r)] + \frac{1}{2}\{[(K_1 + K_r)\alpha_c - \alpha K_r]^2 + 4K_1K_r\alpha_c\alpha\}$$

The slope of this force displacement curve, $dF/d\alpha$, approaches K_r as α approaches infinity,

$$\frac{dF}{d\alpha} = \frac{K_r}{2} + \frac{\alpha K_r^2 - \alpha_c K_r (K_r - K_1)}{2[\alpha^2 K_r^2 - 2\alpha \alpha_c K_r (K_r - K_1) + (K_r + K_1)^2 \alpha_c^2]}$$

Figure B-3a is a schematic representation of the rock-joint model and Fig. B-3b shows the qualitative behavior of the component and combined force-displacement curves. Various assumptions are possible for unloading and reloading with this nonlinear rock-joint model: (a) the unload and reload slopes are equal to K_r , (b) the unload and reload slopes are equal to the tangent of the loading curve at the point of initial unloading, and (c) unload and reload slopes are set to a fixed (input) multiplier of the tangent slope at initial unloading. The selection of the unloading model determines the degree of energy loss during collisions.

B4. OTHER THEORETICAL ASPECTS.

B4.1 Viscous Damping Algorithm.

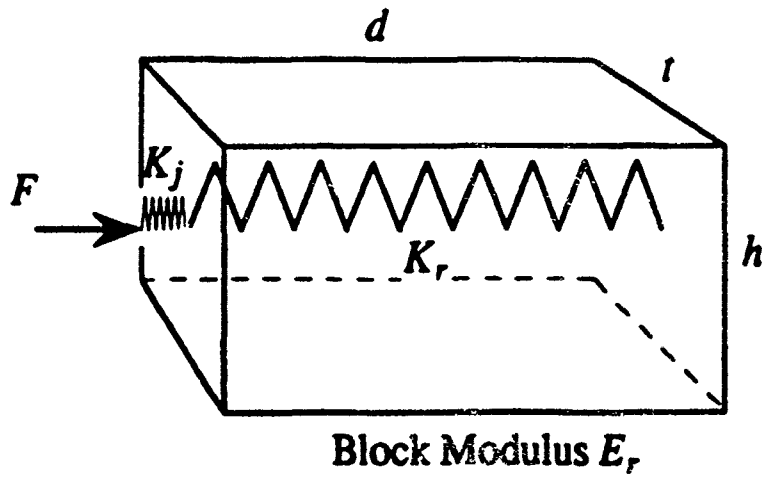
Without any viscous damping, the hysteretic contact model produced some numerical noise in wave propagation calculations. After tests of various damping options, we adopted linear, velocity-proportional damping, the effect of which was shown to be amplitude independent.

$$F = K\alpha - DV$$

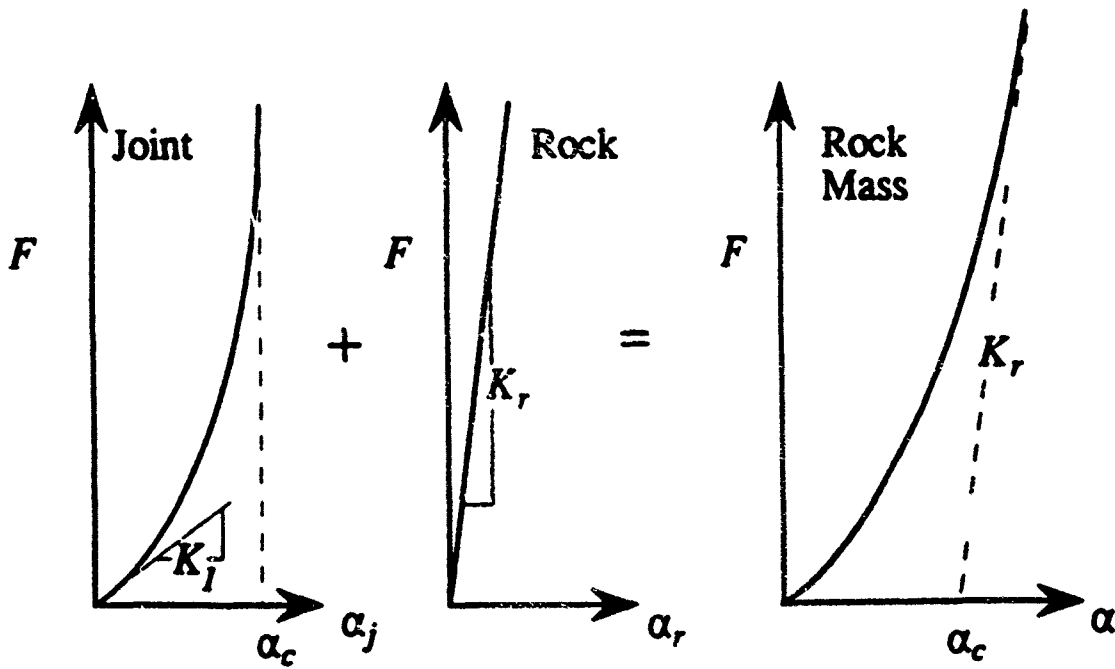
The damping coefficient D is a user input, and it is suggested to be approximately two to five percent of critical damping

$$D = .04(KM) \quad (\text{B-2})$$

where K is the spring stiffness between blocks and M , the average block mass. Figure B-4a is a plot of position versus velocity showing the numerical noise the code was generating when a square pulse was applied to the end of a one-dimensional chain of blocks, without any damping.

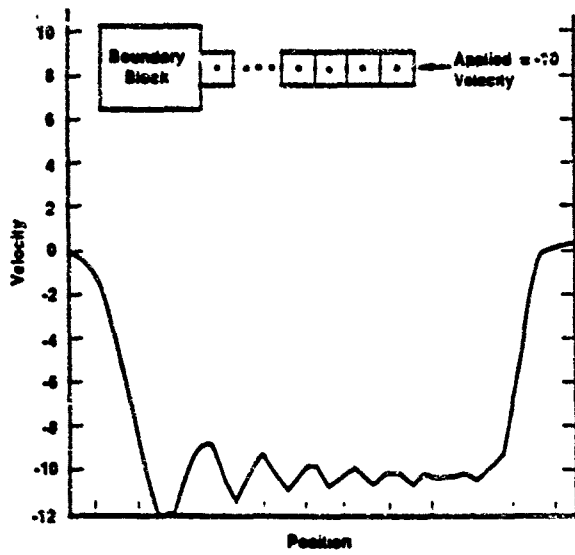


a) Schematic of Rock and Joint Model

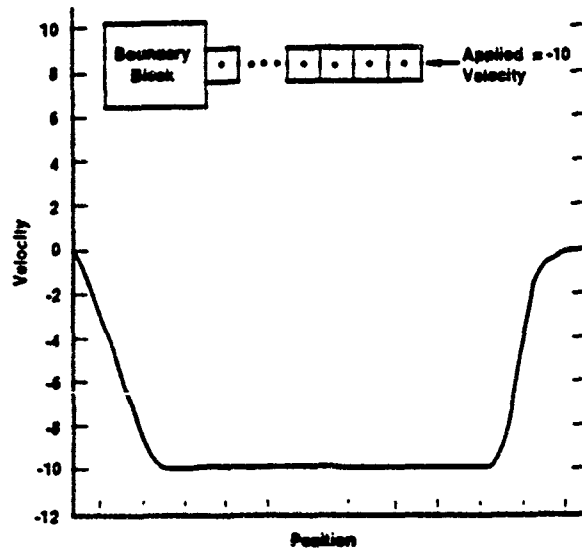


b) Force-Displacement Model for Normal Contact

Figure B-3.

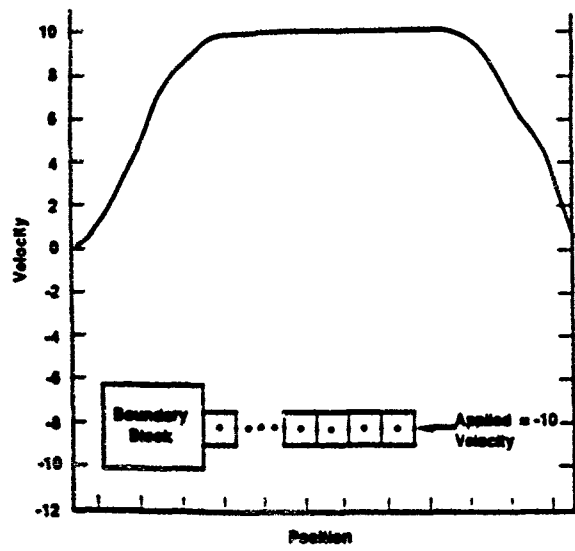


a) No viscosity; numerical noise

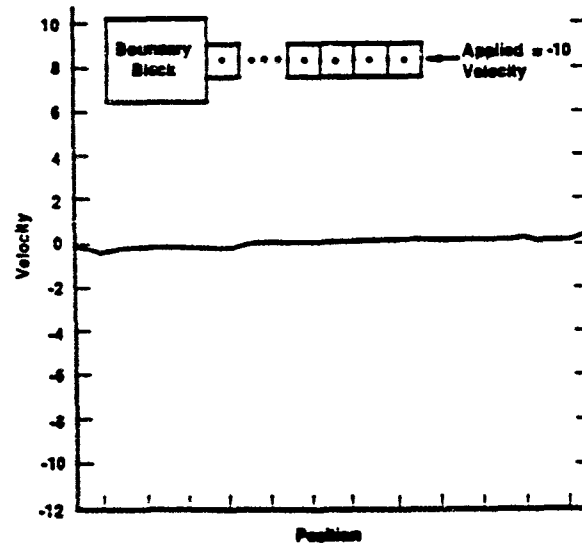


b) Viscosity; no numerical noise

Figure B-4.



a) No infinite boundary;
wave reflection



b) Infinite boundary;
no wave reflection

Figure B-5.

In contrast, Figure B-4b is an illustration of the same plot as in Figure B-4a, but with the addition of the small amount of viscous damping indicated in Equation (B-2).

B4.2 Infinite/non-reflecting Boundaries.

To absorb the wave with no reflected pulse, we added linear damping on the boundary; the dashpot coefficient used was one quarter of critical damping, as determined empirically

$$F = .5(KM) V \quad (B-3)$$

where K is the spring stiffness and M is the block mass for blocks next to the boundary. Note that the functional form of Equation (B-3) is equivalent to the ρC damping used traditionally in infinite boundaries for finite element grids (Lysmer, J. and Kuhlemeyer, R. L., 1969). Figure B-5a is a plot of the wave reflected from the rigid left boundary of a one-dimensional chain of blocks, when the calculation of Figure B-4b is continued without the silent boundary capability. In contrast, Figure B-5b is the same plot but with the addition of the silent boundary capability, and it shows essentially no wave reflection. The wave absorption has proven to be very efficient in two dimensions, as well.

B4.3 Other Features.

Numerous other features were put in DIBS in the past years. They are fully explained elsewhere (Heuze, F. E., et al., 1990), and are summarized as:

- A new method for speeding up gravity settling. A factor of 8 in speed was obtained by using a kinetic energy zeroing algorithm.
- A boundary transformation algorithm to go from the gravity settling mode to the infinite boundary mode.
- A new contact search algorithm which eliminates spurious high forces where new contacts are discovered.
- A time-history capability and restart capability.
- A variety of mesh generating algorithms, including a Voronoi polygon generator.

B5. TIME INTEGRATION.

At each explicit time step of the calculation, a loop through all contacts is performed once, accumulating the total force and moment on each particle for that configuration. Then, the equations-of-motion are integrated one time step and the time advanced. Each coordinate of each particle's position (i.e., x , y , and θ) is integrated in time using a second order accurate scheme valid with non-uniform time steps. For example, the x -coordinate of the centroid of a particle at time step $n+1$ is determined explicitly from the positions at steps n and $n-1$ and the x -direction force at the n th time step, F_x^n , by the expression

$$x^{n+1} = \left(1 + \frac{\Delta t'}{\Delta t}\right)x^n - \left(\frac{\Delta t'}{\Delta t}\right)x^{n-1} + \frac{1}{2}(\Delta t' \Delta t + \Delta t'^2)\ddot{x}^n \dots + O(\Delta t^3)$$

where $\Delta t'$ is the time interval from n to $n+1$, Δt is the time interval from $n-1$ to n , and $\ddot{x} = F_x^n/m$ where m is the mass of the block. If the time step is uniform (i.e., $\Delta t' = \Delta t$), and there are no velocity dependent forces, this expression reduces to the familiar, time centered, third order accurate Verlet scheme commonly used in molecular dynamics calculations (Allen, M. P. and Tildesley, D. J., 1987). Similar expressions are used for the y - and θ -coordinate integrations, based on the total y -direction force and the total moment acting on each block.

Because this is an explicit integration scheme, the time step must be kept below a stability limit determined by the stiffest spring and/or the smallest mass in the system. For accuracy, the time step must usually be kept significantly smaller than the stability limit. Empirical tests of accuracy have determined that on the order of 50 or 100 time steps per physical oscillation cycle are needed for the numerically integrated results to compare favorably with analytic solutions for simple multi-block systems (i.e., $\pm 1\%$).

APPENDIX C

DESCRIPTION OF FINITE ELEMENT METHOD USED IN UTP BENCHMARK ACTIVITY BY CALIFORNIA RESEARCH AND TECHNOLOGY

Yoshio Muki, Y. Marvin Ito

C1. INTRODUCTION.

Finite element methods which incorporate an interface logic are capable of simulating the behavior of jointed rock masses subjected to quasi-static or dynamic loading environments. At California Research and Technology Division (CRT) of The Titan Corporation, analyses of jointed rock mass problems for the UTP Benchmark Activity were performed using EXCALIBUR. Originally developed from NONSAP (Bathe, K. J., et al., 1974), a Lagrangian finite element program for the solution of static and dynamic structural and continuum problems with both geometric and material nonlinearity capabilities, EXCALIBUR has undergone extensive development and validation over the course of many DNA sponsored programs.

The EXCALIBUR code uses an explicit (central-difference) time integration scheme which allows efficient solution of ground shock problems where there are large response gradients in both time and space. An advantage of the explicit algorithm is the ability to incorporate complex constitutive models which represent detailed inelastic behavior of geologic materials. The code also has a variety of special features to enhance numerical solution efficiency, including element underintegration, and controls on the levels of physical models carried by various parts of the finite element grid.

C2. REPRESENTATION OF JOINTED ROCK MASS.

For analyzing tunnel response in jointed rock masses, EXCALIBUR treats large-scale material discontinuities with gap formation and frictional contact using an interface element. A recent enhancement incorporates substructuring at the element level allowing the code to capture micromechanical effects including anisotropy in the far-field jointed system without increasing the global system of equations. These methods of modeling jointed rock masses are used in the UTP benchmark calculations. The first approach, termed discrete joint modeling, will be described next, followed by a description of the second approach termed composite jointed rock modeling.

C2.1 Discrete Joint Modeling.

In the discrete joint modeling approach, both the rock mass and the rock joint are represented by ordinary finite elements, typically four-node quadrilaterals. The mechanical behavior of the rock joints is modeled using a modified version of the CRT Interface Element (Ito, Y. M., et al., 1981). The interface element was developed to treat the mechanical interactions of dissimilar or disconnected bodies. The element typically carries a high aspect ratio with a prescribed stiffness in the direction normal to the joint face.

As specified for the Benchmark Activity, the normal stiffness of the rock joint is prescribed to increase with closure. The element has a constant elastic shear stiffness, with shear bearing capacity along the joint face following a non-dilatant Coulomb-type friction rule (dependent on the normal stress). The element can be prescribed to have no stiffness in tension. This combination of features allows the element to model interface stick, slip and separation.

The constitutive relation governing the interface element is a 2-by-2 matrix, i.e.,

$$\begin{Bmatrix} \Delta\tau \\ \Delta\sigma_n \end{Bmatrix} = \begin{bmatrix} C_{11} & C_{12} \\ C_{21} & C_{22} \end{bmatrix} \begin{Bmatrix} \Delta\gamma \\ \Delta\epsilon_n \end{Bmatrix}$$

where τ and γ are shear stress and strain and σ_n and ϵ_n are normal stress and strain. Under conditions where the interface is closed and no slip is occurring, the incremental constitutive relation is

$$\begin{Bmatrix} \Delta\tau \\ \Delta\sigma_n \end{Bmatrix} = \begin{bmatrix} G' & 0 \\ 0 & E' \end{bmatrix} \begin{Bmatrix} \Delta\gamma \\ \Delta\epsilon_n \end{Bmatrix}$$

where G' and E' are the tangent stiffnesses. While under conditions where slip is occurring, the relation is

$$\begin{Bmatrix} \Delta\tau \\ \Delta\sigma_n \end{Bmatrix} = \begin{bmatrix} 0 & -\frac{\sqrt{\tau^2}}{\tau} \mu E' \\ 0 & E' \end{bmatrix} \begin{Bmatrix} \Delta\gamma \\ \Delta\epsilon_n \end{Bmatrix} ; |\tau| = \tau_c + \mu \tau_n$$

where τ_c is the cohesion and μ is the coefficient of friction. And of course, during separation ($\epsilon_n < 0$), the stiffness is the zero.

In this method, the thickness, location (hence spacing), and orientation of the rock joint are discretely represented in the numerical model. This is an important feature of modeling jointed rock fields near buried structures where the nominal structural dimensions are of the same order as the nominal joint spacing. Thus, a small time step is usually required, not only to retain numerical stability, but to accurately track the nonlinear behavior of the joint system near the tunnel.

C2.2 Composite Jointed Rock Element.

In order to effectively analyze jointed rock mass in the far-field, a composite joint/rock mass element has been developed (Muki, Y., et al., 1992). The composite jointed rock element is a mathematical representation of the mechanical behavior of a rock mass with a regular distribution of joints. The element is intended to capture the mechanical behavior of a characteristic sample of insitu material comprising a rock mass interspersed with joint zones. Each component within the composite joint element is treated as a substructure with a full and

separate constitutive relationship. The interaction of the joint zones and rock mass is based on stress equilibrium and strain compatibility within the element.

The composite jointed rock element assumes a geometric orientation and distribution between intact rock and joint materials, with the intact material taking up most of the region occupied by the element. For the sake of this discussion, the orientation of the distribution of joints is taken to be horizontal and vertical, although this restriction can easily be changed to account for more arbitrary jointed rock mass configurations. The joint zone represents the effects of all joints with similar orientation in the sample. The key parameter is the relative thickness of (distributed) joint material as compared to intact rock. Since there are two types of joints, horizontal and vertical, two characteristic ratios of intact rock thickness to joint material thickness must be defined: the ratio of the width W of the intact material to the width w of the vertical joint material is $\alpha = W/w \gg 1$, and the ratio of the height H of the intact material to the height h of the horizontal joint is defined as $\beta = H/h \gg 1$.

The superscripts used in the development are as follows:

[]ⁱ refers to intact rock material quantities,

[]^v refers to vertical joint material quantities,

[]^h refers to horizontal joint material quantities.

Also, the symbols $\Delta\epsilon^c$ refer to correction strain and $\Delta\sigma^e$ refer to out-of-balance stress. Unscripted quantities refer to overall element (external) quantities which define the composite representation of the response of the various components of the jointed rock mass. These composite values are used during the time integration. Finally, with the exception of out-of-balance stress terms, which are carried forward from the previous time step, all quantities are quoted at the current time step.

The following mathematical development assumes plane strain behavior, with x denoting the horizontal direction and y the vertical direction. Overall composite strain increments are represented by $\Delta\epsilon$, $\{\Delta\epsilon\} = \{\Delta\epsilon_x \Delta\epsilon_y \Delta\gamma_{xy}\}$ and are uniform over the entire element. Correction strain increments are represented by $\Delta\epsilon^c$, $\{\Delta\epsilon^c\} = \{\Delta\epsilon_x^c \Delta\epsilon_y^c \Delta\gamma^c\}$. The correction strains represent perturbations about the overall composite strains and affect each component differently. These correction strain increments are used to adjust the increments in the strains of both the intact rock and the vertical and horizontal joints to attain internal stress equilibrium. Note that the internal strain correction increments do not affect the motions at the four corner nodes. Together, seven strain increment modes (four internal and three external) along with the two material distribution parameters, α and β , fully describe the incremental strain state of each of the components.

The governing equations for compatibility of strain increments are

$$\begin{aligned}\Delta \epsilon_x^I &= \Delta \epsilon_x - \frac{1}{\alpha} \Delta \epsilon_x^c \\ \Delta \epsilon_y^I &= \Delta \epsilon_y - \frac{1}{\beta} \Delta \epsilon_y^c \\ \Delta \gamma^I &= \Delta \gamma - \frac{1}{\alpha} \Delta \gamma^{cv} - \frac{1}{\beta} \Delta \gamma^{ch}\end{aligned}\tag{C-1}$$

for intact rock,

$$\begin{aligned}\Delta \epsilon_x^v &= \Delta \epsilon_x + \Delta \epsilon_x^c \\ \Delta \epsilon_y^v &= \Delta \epsilon_y - \frac{1}{\beta} \Delta \epsilon_y^c \\ \Delta \gamma^v &= \Delta \gamma + \Delta \gamma^{cv} - \frac{1}{\beta} \Delta \gamma^{ch}\end{aligned}\tag{C-2}$$

for vertical joint material, and

$$\begin{aligned}\Delta \epsilon_x^h &= \Delta \epsilon_x - \frac{1}{\alpha} \Delta \epsilon_x^c \\ \Delta \epsilon_y^h &= \Delta \epsilon_y + \Delta \epsilon_y^c \\ \Delta \gamma^h &= \Delta \gamma - \frac{1}{\alpha} \Delta \gamma^{cv} + \Delta \gamma^{ch}\end{aligned}\tag{C-3}$$

for horizontal joint material.

Assuming that changes in stresses produced from the strain changes in the previous time step are not in equilibrium, an inherited out-of-balance in stress increments $\Delta \sigma^e$ must be carried forward and included in the calculation for stress equilibrium at time t . [For example, $\Delta \sigma_x^e = (\Delta \sigma_x^I - \Delta \sigma_x^v) |_{t-\Delta t}$.]

Then, for stress equilibrium, the following equations must hold

$$\begin{aligned}\Delta \sigma_x^e + \Delta \sigma_x^v + \Delta \sigma_x^I &= 0 \\ \Delta \sigma_y^e + \Delta \sigma_y^h &= \Delta \sigma_y^I \\ \Delta \tau^{cv} + \Delta \tau^v &= \Delta \tau^I \\ \Delta \tau^{eh} + \Delta \tau^h &= \Delta \tau^I\end{aligned}\tag{C-4}$$

From the constitutive relationship for intact rock we have

$$\begin{aligned}\Delta \sigma_x^I &= C_{11}^I \Delta \epsilon_x^I + C_{12}^I \Delta \epsilon_y^I \\ \Delta \sigma_y^I &= C_{11}^I \Delta \epsilon_y^I + C_{12}^I \Delta \epsilon_x^I \\ \Delta \tau^I &= C_{33}^I \Delta \gamma^I\end{aligned}\tag{C-5}$$

where the stiffness coefficients C^I are assumed-isotropic and related to bulk modulus K^I and shear modulus G^I by the usual relations

$$C_{11}^I = K^I + \frac{4}{3} G^I$$

$$C_{12}^I = K^I + \frac{2}{3} G^I$$

$$C_{33}^I = G^I$$

Similar relations hold for the vertical joint material (superscript v) and for the horizontal joint material (superscript h).

Combining Equations (C-1) through (C-5) gives a set of equations relating intact rock, vertical joint and horizontal joint strain increments to nominal external and internal strain increments, and corrections in the stress increments of the form:

$$[C] \{\Delta \varepsilon^e\} = [D] \{\Delta \varepsilon\} - \{\Delta \sigma^e\} \quad (C-6)$$

where

$$[C] = \begin{bmatrix} C_{11}^v + \frac{1}{\alpha} C_{11}^I & \frac{1}{\beta} (C_{12}^I - C_{12}^v) & 0 & 0 \\ \frac{1}{\alpha} (C_{12}^I - C_{12}^h) & C_{11}^h + \frac{1}{\beta} C_{11}^I & 0 & 0 \\ 0 & 0 & C_{33}^v + \frac{1}{\alpha} C_{33}^I & \frac{1}{\beta} (C_{33}^I - C_{33}^v) \\ 0 & 0 & \frac{1}{\alpha} (C_{33}^I - C_{33}^h) & C_{33}^h + \frac{1}{\beta} C_{33}^I \end{bmatrix}$$

$$[D] = \begin{bmatrix} C_{11}^I - C_{11}^v & C_{12}^I - C_{12}^v & 0 \\ C_{12}^I - C_{12}^h & C_{11}^I - C_{11}^h & 0 \\ 0 & 0 & C_{33}^I - C_{33}^v \\ 0 & 0 & C_{33}^I - C_{33}^h \end{bmatrix}$$

$$\{\Delta\epsilon^c\} = \begin{Bmatrix} \Delta\epsilon_x^c \\ \Delta\epsilon_y^c \\ \Delta\gamma^{cv} \\ \Delta\gamma^{ch} \end{Bmatrix}; \quad \{\Delta\epsilon\} = \begin{Bmatrix} \Delta\epsilon_x \\ \Delta\epsilon_y \\ \Delta\gamma_{xy} \end{Bmatrix}; \quad \{\Delta\sigma^e\} = \begin{Bmatrix} \Delta\sigma_x^e \\ \Delta\sigma_y^c \\ \Delta\tau^{cv} \\ \Delta\tau^{ch} \end{Bmatrix}$$

When the composite element is used in conjunction with nonlinear materials, a predictor/corrector method (Ito, Y. M., et al., 1981) is used to maintain solution accuracy and efficiency. Briefly, the incremental stiffness relationship in Equation (C-6) is based on secant moduli which are calculated at the end of each time step for use in the equilibrium equation in the following time step. If the type of loading changes (e.g., plastic loading/unloading joint separation closure), a set of revised secant moduli can be calculated for each of the components undergoing the nominal external strain increment. Note that the secant moduli are for an assumed strain increment and may not be the same as for the strain increments obtained after solving Equation (C-6). This difference will lead to out-of-balance stress $\{\Delta\sigma^e\}$ which is added in the following time step.

Given the material moduli, overall strain increments and out-of-balance, Equation (C-6) can be solved for the internal strain increments. For elastic conditions, Equation (C-6) is decoupled into two 2-by-2 systems of equations which are easily solved for $\{\Delta\epsilon^c\}$. Insertion of $\{\Delta\epsilon^c\}$ into the strain compatibility relationships (Equation 2 C-3, C-2, C-3) yields the predicted equilibrium strains for each component of the element. Stresses and other state variables are then updated by exercising the appropriate material model for each of the components in the new strain state. By using the predictor/corrector method, the number of calls to the material model subroutines can be minimized.

Finally, it is also possible and often desirable to use the initial elastic moduli for each of the materials in the internal equilibrium equations *for all time*, even though larger approximations in out-of-balance stresses occur, in order to reduce the numerical cost of the solution. In this case, the out-of-balance stress is used to carry all nonlinear effects into the next time step in the integration.

C3. BENCHMARK CALCULATIONS.

C3.1 Static Calculations (Benchmark Problems 1, 2 and 2-S).

Both discrete and composite joint modeling methods were used to analyze three quasi-static Benchmark cases. As will be shown, except for some numerical cell ringing, excellent agreement was found in all cases between the discrete and composite joint model calculations. In all the quasi-static calculations, no damping was used in the equations of motion.

In Case 1 (Senseny, P. E., 1991), a simplified spherically divergent strain path is used to drive both an intact rock sample and a jointed rock sample. For the jointed rock sample, both discrete and composite joint methods were employed to obtain results for comparison. In Case 2 (Senseny, P. E., 1991), a staggered jointed rock array undergoing uniaxial strain loading is

analyzed. (In this case, the possibility of hourglass distortion in a multi-cell grid was eliminated by using full 2-by-2 integration for the discrete joint calculation. In all other cases, one point integration was used.) In the composite joint calculations, material ratios (α and β) of 200:1 were used.

Case 2-S (Simons, D. E., 1991) was designed to exercise the jointed rock mass models under combined shear and compressive loading. In the discrete model analysis, the rock material was represented using two constant strain triangles and the joint separating the two was modeled using a four node quadrilateral. Although the original problem description contained rollers on the left and lower boundaries, in the present analysis the boundary conditions were driven from all sides to minimize nonsymmetric effects in the solution of the equations of motion. Of the twelve independent displacement degrees of freedom present in the system, eight were controlled by the specified displacement boundary condition, the remaining four were determined by equations of motion.

Case 2-S was repeated using the composite joint model with very similar results. The composite joint analysis uses only one element with eight displacement degrees of freedom. The two internal correction strains are equivalent to the four degrees of freedom solved by the equations of motion in the discrete joint analysis. These two strain terms are solved using the governing equilibrium equations and have vastly different dynamic characteristics than the four degrees of freedom solved by the central difference method used in the discrete joint calculation. The out-of-balance stresses only appear in a portion of the solution after a transition (change of modulus, elastic/plastic loading) and converge rapidly in typical solutions. The composite joint solution under conditions where there are no transitions will give equilibrium exactly. Due to the absence of numerical ringing, the composite joint model yielded very clean results with adequate time resolution, and reliably determined plasticity and joint slip in the solution.

C3.2 Dynamic Calculations (Cases 3 and 4).

Cases 3 and 4 are the field calculations (Senseny, P. E., 1991). In each case both discrete and composite joint models were used to construct a solution. In the near field the joints were modeled discretely as specified and in the far field the composite joint element was used. All elements were evaluated using 2-by-2 integration. To control the numerical ringing during unload, a time dependent stiffness proportional damping was used. From time $t = 0$ to 25 milliseconds, no damping was used. After 25 milliseconds (nominally the TOA of the peak at the tunnel range, damping was increased linearly in time to reach 10% of critical damping at 30 milliseconds. The damping coefficient was held at 10% critical for the remainder of the solution. No lithostatic stresses were assumed to exist in these analyses.

The model of the steel tunnel liner in Case 4 employed a higher-order elasto-plastic element which simulates the response in both thrust and moment. The element is an assemblage of a membrane component to match axial stiffness and a shear/bending component to match moment of inertia. A layer of interface elements with the same normal stiffness behavior used to model the joints but without shear capacity was placed between the tunnel liner and the surrounding rock mass. This allows the structure to freely slide along or separate from the surrounding jointed rock mass during deformation.

APPENDIX D

DESCRIPTION OF THE DISTINCT ELEMENT METHOD USED IN THE UNDERGROUND TECHNOLOGY PROGRAM (UTP) BENCHMARK ACTIVITY

Loren Lorig

D1. INTRODUCTION.

The distinct element method is a recognized discontinuum modeling approach for simulating the behavior of jointed media subjected to quasi-static or dynamic conditions. The method has three distinguishing features which makes it well suited for discontinuum modeling:

- (1) The medium is simulated as an assemblage of blocks which interact through corner and edge contacts.
- (2) Discontinuities are regarded as boundary interactions between these blocks; discontinuity behavior is prescribed for these interactions.
- (3) The method utilizes an explicit timestepping (dynamic) algorithm which allows large displacements and rotations and general non-linear constitutive behavior for both the matrix and discontinuities.

Since the time the method was proposed, several forms of distinct element codes have been developed to cover a range of rock mass strengths and confining pressures which are encountered in situ.

UDEC (Universal Distinct Element Code) is the original mainframe computer code developed for geomechanical analysis in which the performance of rock mass may be dominated by discontinuities (joints, faults, bedding planes). UDEC was originally developed by Dr. Peter Cundall through contracts with the U.S. Army Waterways Experiment Station. Since 1983, Itasca Consulting Group, Inc. have completed a number of modifications to the code which greatly expand its range of applicability.

UDEC is sold by Itasca Consulting Group, Inc. as a source code or as an executable code for use on personal computers and some workstations. Over 150 copies of the code have been sold world wide. The most recent version, Version 1.7, was used as the basis for the benchmark activity. The code was modified to include the intact rock constitutive relation (i.e., Drucker-Prager model) specified for the benchmark problem. With the inclusion of this constitutive model, a new version number was assigned, Version 1.8.

D.2 THE DISTINCT ELEMENT METHOD.

D2.1 Numerical Formulation.

In the distinct element method, a rock mass is represented as an assemblage of discrete blocks. Joints are viewed as interfaces between distinct bodies. The contact forces and

displacements at the interfaces of a stressed assembly of blocks are found through a series of calculations which trace the movements of blocks. Movements result from the propagation through the block system of a disturbance applied at the boundary. This is a dynamic process in which the speed of propagation is a function of the physical properties of the discrete system.

The dynamic behavior is described numerically by using a timestepping algorithm in which the size of the timestep is selected such that velocities and accelerations can be assumed constant within the timestep. The distinct element method is based on the concept that the timestep is sufficiently small that during a single step disturbances cannot propagate from one discrete element in the model further than its immediate neighbors. This solution scheme is identical to that used by the explicit finite difference method for continuum numerical analysis. The timestep restriction applies to both contacts and blocks. For deformable blocks (blocks which are internally discretized into finite difference elements), the zone size is used to define the timestep limitation, and the stiffness of the system includes contributions from both the intact rock modulus and the stiffness at the contacts.

The calculations performed in the distinct element method alternate between application of a force-displacement law at the contacts and Newton's second law of motion at the blocks. The force-displacement law is used to find contact forces from displacements. Newton's second law gives the motion of the blocks resulting from the forces acting on it. If the blocks are deformable, motion is calculated at the gridpoints of the triangular finite-strain elements within the blocks. Then, the application of the block material constitutive relations gives new stresses within the elements.

This numerical formulation satisfies momentum and energy conservation laws by satisfying Newton's laws of motion exactly. Although some error may be introduced in the computer programs by the numerical integration process, this error may be made arbitrarily small by the use of suitable timesteps and high precision coordinates.

D2.2 Rock Joint Representation.

A rock joint is represented numerically as a contact surface (composed of individual point contacts) formed between two block edges. In general, for each pair of blocks that touch (or is separated by a small enough gap), data elements are created to represent point contacts. In UDEC, adjacent blocks can touch along a common edge segment or at discrete points where a corner meets an edge or another corner. For deformable blocks, point contacts are created at all gridpoints located on the block edge. Thus, the number of contact points can be increased as a function of the internal zoning of the adjacent blocks.

A specific problem with contact schemes is the unrealistic response that can result when block interaction occurs close to or at opposing block corners. Numerically, blocks may become locked or hung-up. This is a result of the modelling assumption that block corners are sharp or have infinite strength. In reality, crushing of the corners would occur as a result of a stress concentration. Explicit modeling of this effect is impractical. However, a realistic representation can be achieved by rounding the corners so that blocks can smoothly slide past one another when two opposing corners interact. Corner rounding is used in UDEC by specifying a circular arc for each block corner. The arc is defined by the distance from the true apex to the point of

tangency with the adjoining edges. By specifying this distance rather than a constant radius, the truncation of sharp corners is not severe.

In UDEC, the point of contact between a corner and an edge is located at the intersection between the edge and the normal taken from the center of the radius of the circular arc at the corner to the edge. If two corners are in contact, the point of contact is the intersection between the line joining the two opposing centers of radii and the circular arcs. The directions of normal and shear force acting at a contact are defined with respect to the direction of the contact normal. Contacts along the edge of a deformable block are represented by corners with very large rounding lengths.

Corner rounding only applies to the contact mechanics calculation in UDEC. All other calculations and properties such as block and zone mass are based on the entire block. Corner rounding can introduce inaccuracy in the solution if the rounding is too large. If the rounding length is kept to approximately one percent (1%) of the representative block edge length in the model, good accuracy is achieved.

Contact point information in UDEC is updated automatically as block motion occurs. The algorithms to perform this updating must be computationally efficient, particularly for dynamic analysis, in which large displacements may require deleting and adding hundreds of contacts during the dynamic simulation. UDEC takes advantage of a network of "domains" created by the two-dimensional block assembly. Domains are the regions of space between blocks which are defined by the contact points. During one timestep, new contacts can be formed only between corners and edges within the same domain, so local updates can be executed efficiently whenever some prescribed measure of motion is reached within the domain. The main disadvantage of this scheme is that it cannot be used for very loose systems because the domain structure becomes ill-defined.

D2.3 Rock Joint Behavior.

Numerically, a joint is a special contact type which is classified as an edge-to-edge contact in 2D. In UDEC, a joint is recognized when a domain is defined by two point contacts. The joint is assumed to extend between the two contacts and be divided in half with each half-length supporting its own contact stress. Incremental normal and shear displacements are calculated for each point contact and associated length.

UDEC has two joint behavior relations to describe the mechanical response at the interface. The basic joint model (Coulomb slip model) captures several of the features which are representative of the physical response of joints. In the normal direction, the stress-displacement relation is assumed to be linear and governed by the stiffness k_n such that

$$\sigma_n = k_n u_n$$

where σ_n is the effective normal stress, and u_n is the normal displacement.

There is also a limiting tensile strength, T , for the joint. If the tensile strength is exceeded (i.e., if $\sigma_n < -T$), then $\sigma_n = 0$. Similarly, in shear the response is controlled by a constant shear

stiffness, k_s . The shear stress, τ_s , is limited by a combination of cohesive (C) and frictional (ϕ) strength. This, if

$$|\tau_s| \leq C + \sigma_n \tan \phi = \tau_{\max} \quad (D-1)$$

then

$$\tau_s = k_s u_s^e \quad (D-2)$$

or else, if

$$|\tau_s| \geq \tau_{\max} \quad (D-3)$$

then

$$\tau_s = \text{sign}(u_s) \tau_{\max} \quad (D-4)$$

where u_s^e is the elastic component of the shear displacement, and u_s is the total shear displacement.

For the benchmark activity, a more comprehensive joint model, called the continuously-yielding joint model (Cundall, P. A. and Lemos, J. V., 1990) was used. The continuously-yielding joint model, proposed by Cundall and Hart (1984) and revised by Lemos (1987), is intended to simulate the intrinsic mechanism of progressive damage of the joint under shear. This approach produces consistent responses in the varied conditions encountered in numerical modeling. The model also provides continuous hysteretic damping for dynamic simulations.

The response to normal loading is expressed incrementally as

$$\Delta \sigma_n = k_n \Delta u_n$$

where k_n is the normal stiffness, given by $k_n = \alpha_n \sigma_n^{e_n}$, a simple relation representing the observed increase of stiffness with normal stress, where α_n and e_n are model parameters. The user may specify maximum and minimum normal stiffnesses and, in general, zero tensile strength is assumed.

One feature of the continuously-yielding model is the ability to simulate the intrinsic mechanisms of progressive damage of the joint under shear. Since this feature was not required for the benchmark activity, the shear stress-displacement relation previously described (Equations D-1 through D-4) was used.

D2.4 Block Deformability.

In UDEC, each block is automatically discretized into triangular constant-strain elements. These elements may follow an arbitrary, nonlinear constitutive law (e.g., Mohr-Coulomb failure criterion with non-associated flow rule). Other nonlinear plasticity models recently added to UDEC include a ubiquitous joint model and strain-softening models for both shear and volumetric (collapse) yield. As mentioned in the introduction, the Drucker-Prager model was

added specifically for use in the benchmark activity. The complexity of deformation of the blocks depends on the number of elements into which the blocks are divided. For the benchmark activity, either 4 or 16 triangular zones were used for each square block.

D2.5 Numerical Damping.

If natural energy dissipation such as inter-block sliding or internal block failure accompanies the discontinuum analysis, unwanted vibrations due to initial or transient force imbalance will be absorbed. However, if the analysis is predominantly elastic, some artificial damping will be necessary. Damping is used in UDEC to solve both static and dynamic problems. Static problems generally require more damping than dynamic ones. Two types of damping, mass-proportional and stiffness-proportional, are available in UDEC. Mass-proportional damping (or viscous damping) applies to centroids of rigid blocks or gridpoints of deformable blocks a force which is proportional to the (mass) velocity but in the opposite direction. Stiffness-proportional damping applies to contacts or stresses in zones as a force which is proportional to the incremental force or stress and in the same sense. Either form of damping may be used separately or in combination. The use of both forms of damping in combination is termed Rayleigh damping (Bathe, K. J. and Wilson, E. L., 1976).

Qualitatively, the mass-proportional part tends to act on lower frequency modes which usually are associated with the movement in unison of several blocks or gridpoints ("sloshing"), while the stiffness-proportional component damps higher frequency inter-block vibrations ("rattling").

The mass damping force terms $\{d\}$, for translational degrees of freedom in the momentum equation take the form

$$\{d\} = -\alpha [M] \{\dot{u}\}$$

where $[M]$ is the mass matrix, $\{\dot{u}\}$ is the velocity vector, and α is the mass-proportional damping constant.

Vibrational energy generated at contacts between blocks or within deformable zones is damped by applying stiffness-proportional damping at the contact or zone. The damping force is

$$\{s\} = \beta [K] \{\dot{u}\}$$

where $[K]$ is the stiffness matrix, and β is the stiffness-proportional damping constant. The stiffness damping force is omitted if sliding occurs at the contact or if failure occurs within the zone because frictional dissipation provides natural damping.

For a multiple degree-of-freedom system, choice of the damping constants, α and β , cannot be made with certainty. However, the critical damping ratio, γ , at any natural (angular)

frequency of the system, ω , can be found (Bathe, K. J. and Wilson, E. L., 1976) to be

$$\gamma = \frac{1}{2} \left[\frac{\alpha}{\omega} + \beta \omega \right] \quad (D-5)$$

The level of damping is seen to be frequency-dependent. The values of α and β must be chosen to provide a suitable fraction of critical damping.

Equation (D-5) reaches a minimum at

$$\gamma_{\min} = \sqrt{\alpha\beta}, \quad \omega_{\min} = \sqrt{\frac{\alpha}{\beta}}$$

The fundamental frequency is then defined as

$$f_{\min} = \frac{\omega_{\min}}{2\pi}$$

where units are cycles/second. The values of γ_{\min} and f_{\min} are required input for damping in UDEC. For static analysis, the values have often been determined either by using a simplified analog of the model (for example, the vibration of an equivalent elastic half space) or by monitoring a short undamped run so that dominant modes for damping can be identified. An alternative approach used in UDEC is to employ an "adaptive" damping scheme which adjusts the mass damping constant, α , automatically to the changing conditions of the problem during solution (Cundall, P. A., 1982). The adaptive damping algorithm monitors the rate of energy change in the model during solution. The value of α is adjusted as a function of the rate of energy dissipation and the rate of change of kinetic energy in the model. The algorithm is similar to a servo-mechanism in which an output system control parameter is continuously adjusted based on the measured system response.

For dynamic analysis, the damping should attempt to reproduce the frequency-dependent damping of natural materials at the correct levels. For geologic materials, this is generally 2% to 5% of the critical damping. The dominant frequencies are a combination of the input wave frequencies and the natural modes of the system. For the benchmark activity, no numerical damping was used except to arrive at the prescribed static in-situ conditions prior to application of the dynamic load.

D2.6 Solution Stability.

As mentioned previously, the solution scheme used for the distinct element method is only conditionally stable. The limiting timestep is determined which satisfies both the stability criterion for calculation of internal block deformation as well as that for the inter-block relative displacement. The approximate timestep required for the stability of block deformation computations is

$$\Delta t_{\gamma} = 2 \min \left[\frac{m_i}{k_i} \right]^{1/2}$$

where m_i is the mass associated with block node i , and k_i is the measure of stiffness of the elements surrounding the node. The ratio of mass to stiffness is analogous to the highest eigenfrequency, ω_{\max} , of a linear elastic system.

The stiffness term k_i must account for both the stiffness of the intact rock and that of the discontinuities. It is calculated as the sum of the two components:

$$k_i = \sum k_{zi} + k_{ji}$$

The first term on the right-hand side represents the sum of the contributions of the stiffness of all elements connected to node i , which are estimated as

$$k_{zi} = \frac{8}{3} \left[K + \frac{4}{3} G \right] \frac{b_{\max}^2}{h_{\min}}$$

where K and G are the bulk and shear elastic moduli of the block material, respectively, b_{\max} is the largest zone edge, and h_{\min} is the minimum height of the triangular element. The joint stiffness term k_{ji} exists only for nodes located on the block boundary, and is taken as the product of the normal or shear joint stiffness (whichever is larger) and the sum of the lengths of the two block edge segments adjacent to node i .

For calculations of inter-block relative displacement, the limiting timestep is calculated, by analogy to a simple degree-of-freedom system, as

$$\Delta t_b = (frac) 2 \left[\frac{M_{\min}}{K_{\max}} \right]^{1/2}$$

where M_{\min} is the mass of the smallest block in the system, and K_{\max} is the maximum contact stiffness. The factor *frac* is a user-supplied value which accounts for the fact that a single block is in contact with several blocks. A typical value for *frac* is 0.1.

The controlling timestep for a distinct element analysis is

$$\Delta t = \min(\Delta t_n, \Delta t_b)$$

When stiffness-proportional damping is used, this timestep restriction may not guarantee stability. Belytschko (1983) shows that the timestep in this case should be adjusted as follows:

$$\Delta t = \frac{2}{\omega_{\max}} \left[\sqrt{1 + \gamma^2} - \gamma \right]$$

where ω_{\max} is the highest eigenfrequency of the system, and γ is the fraction of damping at this frequency. This is accounted for in the UDEC analysis by a user-supplied factor based on the selected damping conditions.

APPENDIX E

THE APPLICATION OF THE FLEX PROGRAM TO UTP BENCHMARK PROBLEMS

Felix Wong, David Vaughan

E1. INTRODUCTION.

Weidlinger Associates analyzed the series of UTP Benchmark Problems using the FLEX finite element program (Vaughan, D. K. and Richardson, E., 1991). The FLEX code was developed by Weidlinger Associates to solve a wide range of structural response, structure-media interaction and continuum wave propagation problems.

Several of the smaller benchmark problems were solved running FLEX on an IBM RS/6000 workstation. The larger models were analyzed on a supercomputer at Los Alamos National Laboratory.

E2. OVERVIEW OF THE FLEX CODE.

FLEX is a finite element code designed for 2-D and 3-D dynamic analysis using an explicit time integration approach. Both geometric and material nonlinearity may be included in an analysis. Static problems may also be solved using a dynamic relaxation approach.

E2.1 Time Integration Approach.

The equilibrium equations of motion for a finite element grid can be expressed as:

$$[M] \ddot{u} + [C] \dot{u} + [K] u = Q \quad (E-1)$$

where u is the displacement vector for all nodes of the grid (the single and double dots indicate single and double time derivatives, respectively). $[M]$, $[C]$ and $[K]$ are the mass, damping and stiffness matrices and Q is a vector of applied nodal forces. FLEX solves Equation (E-1) using the second order, central difference approach to explicitly integrate the equations of motion forward in time. A diagonal lumped mass matrix is used and a diagonalized stiffness and/or mass proportional damping matrix is also assumed. This approach avoids the necessity of assembling and manipulating large global stiffness, mass and damping matrices and provides a computationally efficient approach to the solution of large, nonlinear wave propagation problems.

The adopted approach is numerically stable for time steps which are no greater than the Courant stability limit. This criteria can be thought of as the time required for a wave to propagate across the minimum dimension of an element within the model. Since a model may contain locally small or stiff elements which tend to reduce the allowable time step for an element, an approach, termed subcycling, is used to allow different time steps in different regions of the model. This approach minimizes the time step penalty associated with locally small or stiff elements.

E2.2 Element Library.

FLEX may be used to solve both 2-D and 3-D models. For 2-D plain strain or axisymmetric models, the available element types are: 4 node quadrilateral continuum elements, 2 node layered shell (Mindlin plate) and 2 node spring and dashpot continuum elements. For 3-D models, the available element types are: 8 node hexahedron continuum elements, 4 node layered shell and 2 node spring and dashpot elements.

All elements assume linear shape functions and utilize single point quadrature integration for all integrals over the volume of an element. Since this approach under integrates the internal strain energy of an element, there are deformational modes, termed hourglass modes, of an element which are unresisted. The adopted formulation for the continuum elements (Flanagan, D. P. and Belytschko, T., 1981) includes orthogonal hourglass control to suppress these hourglass modes.

E2.3 Constitutive Models.

A number of constitutive models are available within FLEX to allow the simulation of a material's nonlinear constitutive behavior in a high stress environment. These models, developed by Weidlinger Associates, include the cap family of models for soil and rock (Dimaggio, F. L. and Sandler, I. S., 1971) and equivalent models for concrete (Levine, H. S., 1982). These constitutive models use an incremental plasticity formulation with a fixed failure surface and moveable cap. An associated flow rule is assumed. This approach provides guarantees of uniqueness, continuity and stability for material behavior when subjected to multi-dimensional strain paths. Both rate dependent and rate independent models are available. Also, two- and three-invariant plasticity surfaces are available.

E2.4 Geometric Nonlinearity.

Both small rotation/small strain and large rotation/moderate strain options are available within the program. The large rotation/moderate strain option uses an updated Lagrangian approach to account for the geometric nonlinear behavior of the model.

E2.5 Joint Modeling.

FLEX provides two methods (Levine, H. S., et al., 1989) for modeling joints. These are the continuum interface element approach and the slide line approach.

The interface element approach uses 'thin' continuum elements to represent a joint between two blocks of material in an analysis. The interface elements are not the actual thickness of the joint since this would result in severe time step penalties and aspect ratio problems. Instead, an interface element simulates a region of continuum material with a joint embedded within it. These elements have special joint constitutive relations in addition to the standard constitutive properties of the continuum material on either side of the joint. Simulation of slip and separation/recontact can be achieved using this approach. The normal and shear stresses of interface elements are modified based upon whether contact or separation is detected and by limiting the shear stresses tangential to the boundary using a Mohr-Coulomb failure

surface that is fit to joint data. Because the nodal connectivity of interface elements do not change during an analysis, this approach is inherently restricted to problems in which the amount of sliding along an interface is much less than one element dimension.

The slide line approach used in FLEX is a penalty function approach (Halquist, J. O., et al., 1985). This approach allows the user to define multiple domains within the computational model which interact with each other through the forces produced by contact (penalty) springs. Penalty springs form between two domains whenever the nodes of one domain penetrate the exterior boundary of another domain. This approach can be used for problems which include significant sliding along a joint since it accounts for an adaptive connectivity which changes as nodes slide beyond the current contact element on the boundary of a domain.

The main features of the slide line contact computation are as follows: At each time step, after the geometry of the slide line boundary nodes have been updated from the last time step:

- (1) The closest element on the adjacent domain is determined for each slide line node.
- (2) For slide line nodes which are in contact with the adjacent domain: the normal penetration, ϵ , into the adjacent domain and the increment of sliding, δ , along the adjacent domain's perimeter during the present time step is computed.
- (3) The normal contact force, F , due to a nodes penetration of an adjacent domain at time n is computed as

$$F^n = k\epsilon^n A$$

where k represents the normal stiffness of the joint and A is the tributary contact area associated with the node. Currently, k is considered to be a constant but this could be modified so that $k = f(\epsilon)$.

- (4) Equal and opposite reaction forces are distributed to the nodes which define the penetrated element of the adjacent domain. Once this process is complete for all nodes on both sides of the slide line, the total normal interaction force, I , at a node is known. I includes F for the node and any reaction forces due to nodal penetration from the adjacent domain.
- (5) The normal contact stress, σ , for each node at time n is defined as:

$$\sigma^n = \frac{I^n}{A}$$

- (6) The joint shear stress, τ , at time n is evaluated incrementally as:

$$\tau^n = \tau^{n-1} + g\delta$$

where g is the shear stiffness of the joint, assumed to be a constant. τ must also satisfy the Coulomb friction limit defined as:

$$|\tau^n| \leq C + \sigma^n \tan\Phi$$

where C is the initial cohesion and f is the shear friction angle for the joint.

- (7) Nodal forces due to τ are computed for each node and equal and opposite reaction forces are distributed to the nodes of the adjacent contact surface.
- (8) Slide line processing is complete for this time step.

Although the amount of joint slip anticipated to occur for the benchmark problems was not great, the slide line approach was chosen to be used in the UTP Benchmark series since it was anticipated that future problems of interest to DNA may include large amounts of joint slip which would be outside the range of applicability of interface element modeling. Consequently, the benchmark problems were seen as an opportunity to gain practical experience modeling joints using slide lines.

E2.6 Artificial Viscosity.

FLEX allows the use of either linear or quadratic artificial viscosity for shock related wave propagation. These viscosities allow the smoothing out of shocks which form in an analysis due to the hardening behavior of certain types of materials such as many clays. These controls provide a way to control spurious numerical oscillations within the model which occur due to the fundamental frequency limitation of computational models. As is typical for most codes, the viscosity is applied to the volumetric strain rate and is used for compressive strain rates only.

E2.7 Boundary Conditions.

A number of boundary condition options are available within the program including prescribed pressure, prescribed velocity and absorbing boundary conditions. The absorbing boundary condition uses a standard normally incident plane wave assumption (Lysmer, J. and Kuhlemeyer, R. L., 1969). The methodology is derived from one dimensional wave propagation impulse-momentum balance relations. The applicable relationship for the normal velocity at an absorbing boundary is:

$$V_n = \frac{\sigma}{\rho c_p} \quad (\text{E-2})$$

where V_n is the normal velocity, σ is the normal stress, ρ is the mass density of the material and c_p is the dilatational wave speed of the material. The equivalent relationship for the tangential motion at the boundary is:

$$V_t = \frac{\tau}{\rho c_s} \quad (\text{E-3})$$

where V_t is the tangential velocity, τ is the tangential shear stress, and c_s is the shear wave speed of the material.

E3. APPLICATION OF FLEX TO BENCHMARK PROBLEMS.

This section describes specific modeling issues and approaches which were used for the series of benchmark problems. As mentioned previously, the slide line approach was used to explicitly model joint behavior in all the benchmark analyses. No stiffness or mass proportional damping was used. Standard values of artificial viscosity were used. All analysis were performed using 2-D plane strain or axisymmetric models.

The first three benchmark problems are all composed of only a few blocks with explicitly defined joints separating them. The last two benchmarks involved simulations which included regions of the model with explicitly modeled blocks and joints and other regions with implicitly jointed material.

Modeling problem 2 produced excessive numerical chatter in the joints. Improvements in understanding the interaction of discrete blocks using slide line joint models allowed for improved modeling of the final two benchmark problems resulting in negligible numerical noise and chatter due to joint contact.

E3.1 Constitutive Model.

The requested Drucker Prager constitutive model to be used for the benchmark problems was represented within the program by fitting the failure surface of the standard two invariant cap model to the Drucker Prager failure surface. The cap portion of the model was deactivated for all calculations. The standard associated flow rule was utilized.

E3.2 Explicitly Jointed Regions.

In regions of the model where blocks and their surrounding joints were explicitly modeled, all blocks were modeled as fully deformable solids with an 8 x 8 arrangement of 4 node quadrilateral continuum elements. Slide lines were placed on all sides of each block to simulate the joint behavior. The normal stiffness, k , and shearing stiffness, g , of the joint were assumed constant. Although the slide line penalty springs could have been altered to model the specified nonlinear stiffness of the joints, the linear approximation was considered adequate and facilitated matching the overall stiffness of the implicit and explicitly jointed regions throughout the range of applied pressure loading.

E3.3 Implicitly Jointed Regions.

The implicitly jointed material accounts for the presence of joints within a continuum region of the model by altering the constitutive parameters of the native continuum material.

This approach (Singh, B., 1973) alters the elastic stiffness properties of the continuum so that they represent the composite behavior of multiple layers of intact material separated by joints with independent stiffness characteristics. The modified continuum properties are assumed to remain isotropic, i.e. the continuum region is assumed uniformly jointed in all directions. The elastic bulk and shear modulus of the intact continuum material was $K = 20$ GPa and $G = 12$ GPa. For implicitly jointed material, the reduced elastic properties were $K' = 9.5$ GPa and $G' = 8.36$ GPa. The equivalence of the implicit and explicitly jointed material was demonstrated by performing 1-D rock column simulations for both representations and comparing time histories of stress and velocities at equivalent spatial locations.

E3.4 Static Overburden Solution.

A static solution of the model subjected to gravitational loading was performed to provide the insitu stress state as initial conditions for the dynamic response analysis of Benchmark Problems 3 and 4. The geometrical spreading included within the dynamic model was a complication in performing a proper static analysis. This difficulty was avoided by wrapping additional layers of elements around the dynamic model in order to produce a static model with a globally oriented, rectangular outer perimeter. This model, subjected to gravitational load, was then solved using dynamic relaxation. The dynamic analysis used the stress distribution from the static analysis as appropriate initial conditions.

The dynamic response of the two benchmark problems with and without insitu initial conditions was investigated. It was found that the insitu stress state was not very important for this group of problems due to the relatively low stress levels compared to the dynamic loading applied.

E3.5 Boundary Conditions.

Standard boundary conditions (prescribed pressure time histories, symmetry planes, etc.) were used for all benchmark problems. One item of note is the proper use of the absorbing boundary at the bottom of the model for benchmark problems 4 and 5. The default dilatational wavespeed used for the absorbing conditions (Equations E-2 and E-3) are the elastic wave speeds of the material. Since the loading wave speed of the continuum material for the applied loading is significantly slower than the elastic wave speed, the bottom boundaries tended to reflect more of the applied pressure wave than was desirable. Consequently, a proper loading wave speed was determined for the material to more appropriately match the impedance characteristics of the absorber to that of the discretized domain. Standard program options allow the user to override the default elastic wavespeeds for absorbing boundary conditions when the need arises.

E4. LESSONS LEARNED UNDER UTP BENCHMARK SERIES FOR MODELING JOINTED BLOCK BEHAVIOR.¹

The UTP series of benchmark problems provided a useful set of simulation problems and a useful environment for evaluating and enhancing joint modeling simulation capabilities. The benchmark series consisted of a group of problems ranging from small, single element problems to large jointed block assemblages. The solutions for the simpler problems could be evaluated analytically to validate the numerical solutions. The more complex problems could be checked for rational consistency and compared with other independent numerical solutions.

While progressing through the series of benchmark problems, WA gained some useful insight into the application of its simulation software to jointed rock problems. This write up briefly describes the primary lessons learned during the benchmark study phase.

E4.1 Representation of Joint Stiffness.

The penalty function slide line approach used in FLEX uses a default penalty spring stiffness related to the geometric size of the elements adjacent to the slide line and their elastic stiffness properties. This provides an internally computed spring stiffness which minimizes the amount of slide line penetration which may occur but still provides a reasonable, stable time step for the calculation. Initial benchmark calculations using default penalty spring values showed them to be unacceptable when trying to simulate the macro effective stiffness of a jointed block region when the prescribed joint stiffness differs significantly from the default value.

The code input was generalized to allow a user prescribed linear penalty spring stiffness, K. This allows a user to match available joint stiffness data. This provides for a much better representation of the stiffness characteristics of the jointed block assemblage.

E4.2 Numerical Chatter at Joints.

Our initial simulation of benchmark problem #2 manifested a significant amount of numerical chatter or vibration. Numerical experiments using damping to control this chatter were unsatisfactory. The problem was closely scrutinized to identify and understand the source of the numerical noise. It was determined that there were two contributing issues:

- (1) Numerical precision
- (2) Treatment of slide line joints at block corners

E4.2.1 Numerical Precision Issues Related to Joint Modeling.

A recently acquired IBM RS/6000 workstation was used to perform the small benchmark problem simulations. The larger benchmark problems were simulated on a CRAY computer at

¹This subsection was provided during the review of the initial draft of the report to clarify certain modifications implemented during the course of the study.

Los Alamos. Benchmark #2 was run on the IBM using a single precision version of the FLEX code.

We determined that for certain classes of problems, using a 32 bit precision algorithm for slide line computations results in a significantly noisier response than if 64 bit arithmetic were used. This results from the fact that the amount of penetration, ϵ , which is computed by the slide line logic is based on the global coordinates of slide line nodes. Small amounts of penetration which would result in the initiation of resisting penalty function forces in a 64 bit computation can result in an evaluation of no penetration using 32 bit logic. Consequently, 64 bit computations tend to have a smoother contact initiation phase and a correspondingly smoother response.

Follow-on computations were performed using 64 bit precision and resulted in reduced noise and improved slide line response.

E4.2.2 Joint Corner Treatment for Blocks.

Another contribution to the numerical chatter observed in Benchmark #2 was related to the treatment of block corners. The jointed rock benchmark problems contain a number of discrete blocks, each with joint planes all around. Each block is composed of a very stiff material, which has the potential to exhibit a fair amount of elastic ringing. The basic penalty function slide line approach defines the penalty spring forces acting on a node based on the amount of the node's penetration into the surface of an adjacent domain or block. When a node slides beyond the extent of an adjacent block's corner, it no longer can penetrate that block and therefore it is no longer in contact with the block. Consequently, any previous penalty spring forces which were applied to the node are removed. This sudden transition from a penetrating node to a non-penetrating node can produce a local ringing of the node. Since the node is in close proximity to the adjacent block's corner, the local ringing of the node can move it back into contact with the block, causing an amplification of the numerical oscillation of the node. The larger the number of block corners within the model, the larger the number of potential sources of numerical noise from this effect.

Upon careful considerations of the fundamental physical phenomenon we are trying to simulate for the jointed block problem, it was observed that the problem with the current corner treatment derived from the assumption that the entire tributary area of the slide line which is lumped at each node effectively "slides off" or "slides on" to an adjacent node instantaneously, i.e. the node contact is binary (off or on) instead of graded as the node's tributary region slides past the corner. This lumped behavior is fine for many types of problems but for the jointed block problems with the level of discretization being used, the assumption of lumped contact resulted in excessive numerical vibration.

In order to correct for this difficulty, the computation of slide line contact near corners of blocks was extended in order to compute the proportion of a node's tributary area which is in contact with the adjacent block. Therefore, as a node slid past the corner of an adjacent block the penalty spring forces began to decrease smoothly in the proper proportion to the remaining amount of contact area instead of instantaneously being reduced to zero. We suspect this approach is analogous to the usage by Itasca of "rounded corners". While our corners are not

technically rounded, the grading of a penalty spring's resistance as nodes slide off of or on to a corner of a block produces a similar effect.

The extensions to the slide line logic were used for the series of larger benchmark problems helping to produce well-behaved joint interaction computations.

DISTRIBUTION LIST

DNA-TR-92-176

DEPARTMENT OF DEFENSE

ADVANCED RESEARCH PROJECT AGENCY
ATTN: DEFENSE SCIENCES OFFICE

ASSISTANT TO THE SECRETARY OF DEFENSE
ATTN: EXECUTIVE ASSISTANT

DEFENSE INTELLIGENCE AGENCY
ATTN: DB-6E2 J DOPERALSKI
ATTN: DIW-4

DEFENSE NUCLEAR AGENCY
ATTN: OPNA
ATTN: SPSD
5 CY ATTN: SPSD P SENSENY
2 CY ATTN: TITL

DEFENSE TECHNICAL INFORMATION CENTER
2 CY ATTN: DTIC/OC

DNA PACOM LIAISON OFFICE
ATTN: DNALO

FIELD COMMAND DEFENSE NUCLEAR AGENCY
ATTN: FCNM
2 CY ATTN: FCTT W SUMMA
ATTN: NMHE

DEPARTMENT OF THE ARMY

U S ARMY CORPS OF ENGINEERS
ATTN: CERD-L

U S ARMY ENGINEER DIST OMAHA
ATTN: MROED-S H GAUBE

U S ARMY ENGR WATERWAYS EXPER STATION
ATTN: C D NORMAN
ATTN: CEWES J K INGRAM
ATTN: CEWES-SD DR J G JACKSON JR
ATTN: CEWES-SE MR L K DAVIS
ATTN: DR D BANKS CEWES-GS
ATTN: G ALBRITTON
ATTN: J BALSARA CEWES-SS-R
ATTN: J WARRINER WESGR-M
ATTN: RESEARCH LIBRARY
ATTN: W MILLER

DEPARTMENT OF THE AIR FORCE

AIR FORCE CTR FOR STUDIES & ANALYSIS
ATTN: AFSAA/SAI

AIR UNIVERSITY LIBRARY
ATTN: AUL-LSE

DEPARTMENT OF ENERGY

LOS ALAMOS NATIONAL LABORATORY
ATTN: REPORT LIBRARY

SANDIA NATIONAL LABORATORIES
ATTN: DIV 9311 L R HILL
ATTN: TECH LIB 3141
ATTN: S ATTAWAY

ATTN: L COSTIN
ATTN: C W SMITH

OTHER GOVERNMENT

CENTRAL INTELLIGENCE AGENCY
ATTN: OSWR/NED

DEPARTMENT OF THE INTERIOR
ATTN: P SANDS

DEPARTMENT OF DEFENSE CONTRACTORS

AEROSPACE CORP
ATTN: LIBRARY ACQUISITION

ANALYTIC SERVICES, INC (ANSER)
ATTN: K BAKER

APPLIED RESEARCH ASSOCIATES, INC
ATTN: C J HIGGINS

APPLIED RESEARCH ASSOCIATES, INC
ATTN: S BLOUIN

APPLIED RESEARCH ASSOCIATES, INC
ATTN: R FRANK

BDM ENGINEERING SERVICES CO
ATTN: D BURGESS

BOEING TECHNICAL & MANAGEMENT SVCS, INC
ATTN: W M LEAVENS
ATTN: A W SPENCER
ATTN: ROSS J WOOD

CALIFORNIA RESEARCH & TECHNOLOGY, INC
ATTN: J THOMSEN
ATTN: K KREYENHAGEN

IIT RESEARCH INSTITUTE
ATTN: DOCUMENTS LIBRARY
ATTN: M JOHNSON

INSTITUTE FOR DEFENSE ANALYSES
ATTN: CLASSIFIED LIBRARY

JAYCOR
ATTN: CYRUS P KNOWLES

KAMAN SCIENCES CORP
ATTN: RICHARD KEEFFE

KAMAN SCIENCES CORP
ATTN: DASAC

KAMAN SCIENCES CORPORATION
ATTN: DASAC

LACHEL AND ASSOCIATES, INC
ATTN: C LINAMEN
ATTN: J BECK

LOGICON R & D ASSOCIATES
1 CY ATTN: D SIMONS
ATTN: LIBRARY

DNA-TR-92-176 (DL CONTINUED)

LOGICON R & D ASSOCIATES
ATTN: J WALTON

LOGICON R & D ASSOCIATES
ATTN: D PIEPENBURG

NTS ENGINEERING
ATTN: R KENNEDY
ATTN: S SHORT

PACIFIC-SIERRA RESEARCH CORP
ATTN: H BRODE

PACIFIC-SIERRA RESEARCH CORP
ATTN: D GORMLEY

RE/SPEC INCORPORATED
ATTN: J OSNES

S-CUBED
ATTN: K D PYATT JR

SCIENCE APPLICATIONS INTL CORP
ATTN: DR M MCKAY
ATTN: H PRATT
ATTN: TECHNICAL REPORT SYSTEM

SCIENCE APPLICATIONS INTL CORP
ATTN: W LAYSON

SOUTHWEST RESEARCH INSTITUTE
ATTN: A FOSSUM
ATTN: B THACKER
ATTN: S HSUING

SRI INTERNATIONAL
ATTN: J GRAN

TITAN CORPORATION
ATTN: LIBRARY
ATTN: S SCHUSTER
ATTN: Y M ITO

TRW SPACE & DEFENSE SECTOR
ATTN: W WAMPLER

UTD, INC
ATTN: E FOSTER

WEIDLINGER ASSOC, INC
ATTN: F WONG
ATTN: H LEVINE

WEIDLINGER ASSOCIATES, INC
ATTN: I SANDLER
ATTN: M BARON

WOODWARD-CKYDE
ATTN: F TSAI